

THE ROLES OF IRON AND CADMIUM IN HUMAN HEALTH

By

YU WANG

LAURA BUSENLEHNER, COMMITTEE CHAIR

JOHN VINCENT

CAROLYN CASSADY

KEVIN SHAUGHNESSY

CAROL DUFFY

A DISSERTATION

Submitted in partial fulfillment of the requirements
for the degree of Doctor of Philosophy
in the Department of Chemistry
in the Graduate School of
The University of Alabama

TUSCALOOSA, ALABAMA

2014

Copyright Yu Wang 2014
ALL RIGHTS RESERVED

ABSTRACT

The trace transition metals in humans are divided into two groups, the essential metals and the non-essential/non-native heavy metals. This dissertation research explores the interactions of two transition metals, iron and cadmium, with protein targets to understand their effects on human health.

Iron is an important essential metal and is a component of two inorganic cofactors, heme and Fe/S clusters. Disruption of heme and Fe/S cluster cofactor assembly causes downstream protein dysfunction, oxidative stress, and cellular damage. Many diseases, such as the neurodegenerative disease Friedreich's ataxia (FRDA), are caused by the inability to synthesize Fe/S clusters. FRDA is the result of decreased expression of the mitochondrial protein frataxin; however, its exact function is unclear. In this dissertation, a *Schizosaccharomyces pombe* fission yeast strain was generated in which the yeast frataxin homologue *fxn1* was overexpressed to determine what the function(s) of frataxin is through the affected pathways. Based on this study, we demonstrated that *S. pombe* Fxn1 overexpression elevated the activities of Fe/S enzymes through the up-regulation of Fe/S cluster synthesis, which led to imbalanced iron metabolism, mitochondrial dysfunction and oxidative stress. This research supports that mitochondrial Fxn1 up-regulates the efficiency of Fe/S cluster assembly and provides insight into the cause of FRDA.

Besides diseases caused by dysregulation of essential metals, there are diseases related to chronic exposure to heavy metals. The heavy metal cadmium is linked to breast cancers, but with unknown mechanisms. One proposed mechanism is that Cd^{2+} activates the estrogen

receptor α (hER α) transcriptional regulator by binding to the protein and mimicking the conformational effects of the hormone estrogen. We utilized hydrogen/deuterium exchange mass spectrometry to analyze the structural changes of the hER α ligand binding domain upon estradiol or Cd²⁺ binding. Estradiol binding leads to conformational changes in the dimer interface, the estradiol binding cavity, and the loop between helix H11 and H12. Cadmium demonstrated similar conformational changes at the dimer interface and helix H12. This is the first direct evidence that hER α LBD undergoes structural changes upon Cd²⁺ binding that are similar to that caused by hormone binding, lending support for this potential mechanism of Cd²⁺-induced carcinogenesis.

LIST OF ABBREVIATIONS AND SYMBOLS

[2Fe–2S] cluster	two iron–two sulfur cluster
[3Fe–4S] cluster	three iron–four sulfur cluster
[4Fe–4S] cluster	four iron–four sulfur cluster
°C	Celsius degree
μg	microgram
μL	microliter
μM	micromolar
μM ⁻¹	inverse micromolar
6His	6 histidine tag
Å	angstrom
A ₂₃₀	absorbance at 230 nm
A ₂₆₀	absorbance at 260 nm
A ₂₈₀	absorbance at 280 nm
ABC transporter	ATP-binding cassette transporter
ABCB7	ABC transporter B family member 7
AF-1	N-terminal transactivation domain
AF-2	C-terminal transactivation domain
Aft1p	iron-regulated transcriptional activator 1

ALAS	5-aminolevulinate synthase
Asp	aspartic acid
Atm1	iron-sulfur clusters transporter
AU	adenine and uracil
BCA assay	bicinchoninic acid assay
BCIP	5-Bromo-4-chloro-3-indolyl phosphate
BPS	bathophenanthrolinedisulfonic acid
BRCA1	breast cancer type 1 susceptibility protein
BSA	bovine serum albumin
cDNA	complementary DNA
CIA	cytosolic iron sulfur protein assembly system
CID	collision induced dissociation
cm ⁻¹	inverse centimeter
DBD	DNA binding domain
D-box	distal box
DCIP	2,6-dichlorophenolindophenol
DFO	desferoxamine
DNA	deoxyribonucleic acid
DTNB	5,5'-dithio-bis(2-nitrobenzoic)
DTPA	diethylene triamine pentaacetic acid
DTT	dithiothreitol
E2	17 β -estradiol
EDTA	ethylenediaminetetraacetic acid

EMM	edinburgh minimal media
ER	estrogen receptor
ERE	estrogen response element
Fe/S cluster	iron sulfur cluster
FeCH	ferrochelatase
Fep1	iron sensing transcription factor 1
Fet4	low affinity iron/zinc transport protein
Fio1	iron transport multicopper oxidase
Fip1	plasma membrane iron permease
FRDA	Friedreich's ataxia
Frp1	ferric reductase
FXN	human frataxin gene
Fxn1	<i>Schizosaccharomyces pombe</i> frataxin homolog
GAA	guanine-adenine-adenine
Gal4	yeast galactose-induced regulator 4
GATA	guanine-adenine-guanine-adenine
GI	gastrointestinal
GLRX5	glutaredoxin-related protein 5
Glu	glutamic acid
Grx5	monothiol glutaredoxin-5
GSH	glutathione
GuHCl	guanidinium chloride
h	hour

HDX-MS	hydrogen/deuterium exchange mass spectrometry
HEPES	4-(2-hydroxyethyl)-1-piperazineethanesulfonic free acid
HER2	human epidermal growth factor receptor 2
hER α	human estrogen receptor alpha
hFxn	human frataxin protein homolog
His	histidine
HPLC	high-performance liquid chromatography
Hsp70	heat shock protein 70 kDa protein
IgG	immunoglobulin G
IPTG	isopropyl- β -D-thiogalactopyranoside
IRP	iron-responsive element-binding protein
ISC	iron sulfur cluster system
IscR	HTH-type transcriptional regulator
ISCU	Iron-sulfur cluster assembly enzyme
Isd11	protein ISD11
Isu1	iron sulfur cluster assembly protein 1
Jac1	J-type co-chaperone JAC1
K _d	dissociation constant
kDa	kilodalton
K _{sp}	solubility equilibrium constant
L	liter
LB	luria bertani
LBD	ligand binding domain

Lys	lysine
M	molar
m_0	natural isotope abundance
M^{-1}	inverse molar
m_{100}	theoretical number of exchangeable amide hydrogens
MALDI	matrix-assisted laser desorption/ionization
MBP	maltose binding protein
min	minute
mL	milliliter
mM	millimolar
mm	millimeter
MPP1	mitochondrial processing peptidase
mRNA	messenger ribonucleic acid
MS	mass spectrometry
MT	metallothionein
m_t	the centroid of the peptides at time t
N	nitrogen
NADH	nicotinamide adenine dinucleotide
$NADP^+$	nicotinamide adenine dinucleotide phosphate
NBT	nitro blue tetrazolium chloride
NCoA-2	human nuclear receptor coactivator 2
Nfs1	cysteine desulfurase
ng	nanogram

NIF	nitrogen fixation systems
NLS	nuclear localization sequence
nM	nanomolar
nm	nanometer
NMR	nuclear magnetic resonance
<i>nmt1</i>	no message with thiamine
NRAM1	natural resistance-associated macrophage protein 1
NRAMP2	non-specific divalent metal transporter
O	oxygen
O_2^-	superoxide ion
OD ₆₀₀	absorbance at 600 nm
OH [•]	hydroxyl radical
PAGE	polyacrylamide gel electrophoresis
P-box	proximal box
PBS buffer	phosphate buffered saline
PCR	polymerase chain reaction
PMS	phenazine methosulfate
PMSF	phenylmethylsulfonyl fluoride
ppm	part per million
PTM	post translational modification
qPCR	quantitative PCR
qRT-PCR	quantitative real-time polymerase chain reaction
RNA	ribonucleic acid

ROS	reactive oxygen species
rpm	round per minute
s	second
<i>S. cerevisiae</i>	<i>Saccharomyces cerevisiae</i>
<i>S. pombe</i>	<i>Schizosaccharomyces pombe</i>
S ²⁻	sulfide ion
SDH	succinate dehydrogenase
SDS	sodium dodecyl sulfate
SOD	superoxide dismutase
Ssq1	heat shock protein SSQ1
Str1/2/3	siderophore iron transporter 1/2/3
SUF	sulfur mobilization system
t	time
TAE	tris base, acetic acid and ethylenediaminetetraacetic acid
TCA cycle	citric acid cycle
TCEP	tris(2-carboxyethyl)-phosphine hydrochloride
TOF	time of flight
Tris	2-amino-2-hydroxymethyl-propane-1,3-diol
Trp	tryptophan
V	volts
Xho1	type II restriction enzyme
Yfh1	yeast frataxin homolog 1
ZIP	zinc transporter

β ME

β -mercaptoethanol

$\Delta\%D$

the difference of deuterium incorporation

ACKNOWLEDGMENTS

I would like to thank my research advisor, Dr. Laura Busenlehner for her training, support, encouragements, and patience during my Ph. D. research. This dissertation is only possibly with her constant guidance and advice. Her enthusiasm and working attitude always encourage me to be a better scientist.

I would also like to thank my committee members, Dr. John Vincent, Dr. Carolyn Cassady, Dr. Kevin Shaughnessy and Dr. Carol Duffy for their valuable advice and help through my studies and research.

I am also thankful to Dr. Steven Marcus and members of Marcus lab for instructions of yeast culture and technologies. I especially thank Dr. Jenny and members of Jenny lab, Dr. Marco Bonizzoni, and Dr. Patrick Frantom for allowing me to use their instruments and their valuable suggestions. I also thank Dr. Qiaoli Liang for the assistance with mass spectrometry. The financial support from the National Science Foundation and The University of Alabama Research Grant Committee Award is greatly appreciated. I also would like to acknowledge the support from The University of Alabama and the Chemistry Department.

I would like to thank the current and past group members of Busenlehner Lab, especially Leslie Gentry, Mier An and Harsimran Singh for their support during my research.

Finally, I would like to thank my family and friends for all their love and support.

CONTENTS

ABSTRACT.....	ii
LIST OF ABBREVIATIONS.....	iv
ACKNOWLEDGMENTS	xii
LIST OF TABLES	xvii
LIST OF FIGURES	xviii
CHAPTER 1. IRON HOMEOSTASIS AND ITS BIOLOGICAL FUNCTIONS.....	1
1.1. The Functions of Transition Metals in Living Organisms.....	1
1.2 Iron Biochemistry and Homeostasis in the Fission Yeast <i>S. pombe</i>	2
1.2.1 The Redox Chemistry of Iron and Free Radicals in Biological Systems	2
1.2.2 Iron Assimilation and Homeostasis in <i>Schizosaccharomyces pombe</i>	5
1.3 Iron Metabolism	7
1.3.1 Heme Synthesis and Regulation	11
1.3.2 Fe/S Cluster Assembly and Regulation	12
1.4 Human Diseases Related to Fe/S Cluster Assembly	15
1.4.1 Friedreich’s Ataxia (FRDA)	16
1.4.2 The Biochemical Characteristics of Frataxin Homologues	17
1.5 Scope of This Section of the Dissertation Research	19
CHAPTER 2. DISSECTING THE IN VIVO FUNCTIONS OF FRATAXIN IN <i>S. POMBE</i>	21
2.1. Introduction	21

2.2	Materials and Methods	24
2.2.1	Materials	24
2.2.2	Yeast Strains and Cell Cultures	24
2.2.3	Plasmid Construction	25
2.2.4	Co-transformation of pREP3X/Fxn1 and pREP4X/Isu1 into <i>S. pombe</i>	25
2.2.5	Overexpression of Fxn1	25
2.2.6	Purification of Fxn1–6His from <i>S. pombe</i>	26
2.2.7	Serial Dilution Growth Assays	26
2.2.8	Respiration Assays	27
2.2.9	Quantitative RT-PCR	27
2.2.10	Preparation of <i>S. pombe</i> Whole Cell Lysates	29
2.2.11	Western-blot Analysis	29
2.2.12	Isolation of <i>S. pombe</i> Mitochondria	29
2.2.13	Iron Content Analysis	30
2.2.14	Aconitase Activity Assay	30
2.2.15	Succinate Dehydrogenase Activity Assay	31
2.2.16	Superoxide Dismutase and Catalase Activity Assays	31
2.2.17	Expression and Purification of Fxn1 from <i>E. coli</i>	32
2.2.18	Sulfo-SBED Labeling and Crosslinking Reactions	33
2.2.19	Statistics	34
2.3	Results	34
2.3.1	Cellular Growth Defect Induced by Fxn1 Overexpression	34
2.3.2	Characterizing the Level of Fxn1 Overexpression and its Maturation in <i>S. pombe</i>	39

2.3.3	Fxn1 Overexpression in Mitochondria Leads to Iron Accumulation	42
2.3.4	Activities of Mitochondrial Fe/S Enzymes Increase Upon Mitochondrial Fxn1 Overexpression	49
2.3.5	Fxn1 Overexpression Cells Have Increased Oxidative Stress	50
2.3.6	Fxn1 Interactions with Other Mitochondrial Proteins	53
2.4	Discussion	62
2.4.1	The <i>in vivo</i> Function of Fxn1 in <i>S. pombe</i>	62
2.4.2	Protein-Protein Interactions with Fxn1	65
2.5	Future Work	66
2.6	Biological Implications	67
CHAPTER 3. CADMIUM, BREAST CANCER AND HUMAN ESTROGEN RECEPTOR ALPHA		68
3.1	The Bioinorganic and Biochemical Characteristics of Cadmium	68
3.2	Cadmium Toxicity	69
3.3	Xenoestrogens and Human Breast Cancer	72
3.4	Structure and Functions of HER α	73
3.5	Scope of the Dissertation Research	80
CHAPTER 4. THE STUDY OF CADMIUM BINDING TO HUMAN ESTROGEN RECEPTOR AND RELATED STRUCTURAL CHANGES.....		81
4.1	Introduction	81
4.2	Methods and Materials	85
4.2.1	Materials	85
4.2.2	Expression and Purification of Full-length HER α in <i>E. coli</i>	86
4.2.3	Expression and Purification of Full-length HER α in <i>S. pombe</i> Cells	87
4.2.4	Western-blot Analysis	88

4.2.5	Purification of HER α LBD	88
4.2.6	Preparation of Apo-hER α LBD	90
4.2.7	Tandem Mass Spectrometry	90
4.2.8	Free Thiolate Quantitation	91
4.2.9	Fluorescence Titration of LBD with Estradiol and Cd ²⁺	91
4.2.10	Amide Hydrogen/Deuterium Exchange Mass Spectrometry	91
4.3	Results.....	93
4.3.1	The Purification of Full-length HER α from <i>E. coli</i> and <i>S. pombe</i>	93
4.3.2	The Purification of the Ligand Binding Domain	97
4.3.2	Quantification of the Reduced Thiol Groups in Apo-LBD	97
4.3.3	Estradiol Titration of LBD	99
4.3.4	Cd ²⁺ Titration of LBD	99
4.3.5	The Deuterium Incorporation of E2-LBD	100
4.3.6	The Deuterium Incorporation of Cd ²⁺ -LBD	106
4.4	Discussion	108
4.4.1	Barriers to Structural Characterization of Full-length HER α	108
4.4.2	Estrogen Binding to the HER α Ligand Binding Domain	109
4.4.3	Cadmium Binding to the HER α Ligand Binding Domain	113
4.4.4	Localization of the Cd ²⁺ Binding Site within the LBD	113
4.5	Future Work	118
	REFERENCES	120

LIST OF TABLES

1.1.	The two major types of Fe/S clusters, their basic characteristics, and example proteins ..	13
2.1.	The major observations of frataxin overexpression in different organisms	22
2.2.	The primers used in qRT-PCR experiments	28
2.3.	The relative transcript levels of interested genes, normalized to <i>act1</i> as the housekeeping gene	52

LIST OF FIGURES

1.1.	The structures of heme, [2Fe-2S] and [4Fe-4S] clusters	3
1.2.	The iron uptake pathways of <i>S. pombe</i>	6
1.3.	The primary iron uptake pathway of <i>S. pombe</i> , the high affinity iron import system	8
1.4.	Regulation of iron homeostasis of <i>S. pombe</i> through the transcription factor Fep1	9
1.5.	Iron metabolism in eukaryotic cells	10
1.6.	The Fe/S cluster biogenesis machinery in mitochondria	14
1.7.	The sequences and structural alignment of frataxin homologues	18
2.1.	The overexpression of Fxn1 in <i>S. pombe</i> mitochondria causes cells growth inhibition....	36
2.2.	The co-overexpression of Fxn1 and Isu1 in <i>S. pombe</i> mitochondria causes exacerbated cell growth inhibition	37
2.3.	The respiration rate significantly decreased for cells with high levels of mitochondrial Fxn1	38
2.4.	The growth defect of Fxn1 overexpression transformants was partially relieved under anaerobic growth conditions	40
2.5.	Fxn1 mRNA and protein overexpression levels	41
2.6.	The MALDI-ToF spectra of mature form Fxn1-6His	43
2.7.	Native gel electrophoresis of Fxn1 overexpression demonstrates the existence of Fxn1 oligomers	44
2.8.	Overexpression of Fxn1 in mitochondria causes cellular iron accumulation and up-regulated iron importing system	45
2.9.	Increased amount of the red BPS-Fe ²⁺ complex on cells surface indicates the increased Frp1 activity and thus up-regulated iron importing pathway	47

2.10.	The resistance of Fxn1 overexpression transformants to specific and non-specific iron chelators	48
2.11.	Aconitase and SDH activities increase at protein levels as Fxn1 overexpressed in mitochondria	51
2.12.	The low level overexpression of Fxn1 in mitochondrial elevates the cellular resistance to H ₂ O ₂	54
2.13.	Increased SODs and catalase activity were observed for cells overexpress Fxn1	55
2.14.	Structure of Sulfo-SBED	57
2.15.	The control reactions of photo-activated chemical crosslinking	58
2.16.	Photo-activated chemical crosslinking to identify proteins that interact with <i>S. pombe</i> Fxn1	60
2.17.	Photo-activated chemical crosslinking Fxn1 and <i>S. pombe</i> extracts	61
3.1.	The schematic structure of a four Cys zinc finger	71
3.2.	The three major domains in hER α	74
3.3.	The DNA binding domain of hER α	75
3.4.	The monomeric ligand binding domain of hER α	77
3.5.	The structural overlay of hER α /LBD-E2 complex and hER α /LBD-raloxifene complex..	78
3.6.	Important amino acid residues for hER α /LBD estradiol binding	79
4.1.	The structure of 17 β -estradiol and the possible amino acid residues involved in Cd ²⁺ binding and activation of hER α	82
4.2.	The expression and purification of full-length hER α in pET-21b in CD146 <i>E. coli</i> strain	94
4.3.	The expression and purification of MBP-6His-hER α from BL21(DE3)pLysS cells	95
4.4.	The purification process and final product of full-length hER α -6His in <i>S. pombe</i>	96
4.5.	The purification and LC-MS/MS mapping of hER α LBD	98
4.6.	The fluorescent titration of E2 and Cd ²⁺ to purified LBD	101

4.7.	The HDX–MS profiles of apo–LBD, E2–LBD, and Cd ²⁺ –LBD (1)	102
4.8.	The HDX–MS profiles of apo–LBD, E2–LBD, and Cd ²⁺ –LBD (2)	103
4.9.	The solvent accessibility and dynamic changes of hER α LBD upon E2 binding, determined by HDX–MS	105
4.10.	The solvent accessibility and dynamic changes of hER α LBD upon Cd ²⁺ binding	107
4.11.	The protein sequence alignment of full-length hER α and hER β	112
4.12.	The possible binding site(s) of Cd ²⁺ in hER α LBD	116
4.13.	The Au ⁺ binding sites in hER α LBD	117

CHAPTER 1

IRON HOMEOSTASIS AND ITS BIOLOGICAL FUNCTIONS

1.1 The Functions of Transition Metals in Living Organisms

Human bodies contain trace amounts of transition metals, less than 0.1% of total body weight (1, 2). Transition metals can be divided into two groups based on their functions in cells, the essential metals and the non-essential/non-native heavy metals. Essential metals are important components for many proteins and are required for function, either as the catalytic center of enzymes or by maintaining the proper protein conformation (3, 4). These include such metals as iron, copper, zinc, cobalt, and manganese among others (4). Depletion of essential metals could lead to decreased enzyme activity, misfolded proteins, and dysregulated metabolism, while excess amounts of essential metals could be toxic and cause cellular damage (3, 4). Organisms have developed delicately regulated homeostasis systems to carefully control the redox species and concentration of these essential metals (1).

Non-native heavy metals such as cadmium, lead and mercury do not have biological functions but may instead inhibit normal cellular functions and lead to cellular damage (5). Cells do not have specific mechanisms to uptake these metals, and the absorption of heavy metals are through the non-specific divalent metal transporter proteins or specific ion channels proteins with similar chemical properties (6). Nevertheless, there are also defense mechanisms to help the cell deal with heavy metals, primarily through chelating them with the sulfhydryl rich proteins, such as metallothionein (MT) (7).

1.2 Iron Biochemistry and Homeostasis in the Fission Yeast *S. pombe*

Iron, the most abundant metal on the planet, is also the metal component of two of the most important inorganic cofactors in biological systems, heme and iron/sulfur (Fe/S) clusters (**Figure 1.1**). Iron acquisition is difficult and potentially harmful under our modern oxygenated atmosphere as soluble ferrous iron (Fe^{2+}) is unstable and easily oxidized to ferric iron (Fe^{3+}). Ferric iron has low solubility in an aqueous environment ($K_{sp} = 10^{-39}$ M) and, thus, forms an insoluble ferric hydroxide precipitate (5, 6). The concentration of soluble Fe^{3+} at neutral pH is estimated to be 10^{-18} M (8, 9). Delicately balanced iron uptake and metabolism pathways were evolved to successfully maintain biologically available Fe^{2+} concentrations in healthy organisms. Both Fe^{2+} and Fe^{3+} are Lewis acids of different strengths. Based on Lewis acid/base theory, ferric iron is a hard acid with an octahedral ionic radius of 0.67 \AA , which makes it prefer hard ligands such as oxygen (*e.g.*, phenolate and carboxylate) (8). On the other hand, ferrous iron has an octahedral ionic radius of 0.83 \AA and acts as a softer acid, with preferred ligands such as nitrogen (*e.g.*, imidazole and pyrrole) and sulfur (*e.g.*, thiolate and thioether) (8).

1.2.1 The Redox Chemistry of Iron and Free Radicals in Biological Systems

The most common biological oxidation states of iron are Fe^{2+} and Fe^{3+} , although Fe^{1+} , Fe^{4+} , and Fe^{5+} are often found in short-lived, catalytic intermediate states. The one electron transfer between Fe^{2+} and Fe^{3+} is easily accomplished with the redox potentials from -0.5 V to $+0.6 \text{ V}$, though the standard redox potential of the $\text{Fe}^{3+}/\text{Fe}^{2+}$ couple in water is $+0.77 \text{ V}$ (8, 9). This redox chemistry is reversible in biological systems only when the redox potential of complexed iron falls between $+0.82 \text{ V}$ to -0.32 V , which is the accessible range of biological oxidants (*e.g.*, dioxygen at pH 7.0) and reductants (*e.g.*, NADH) (9).

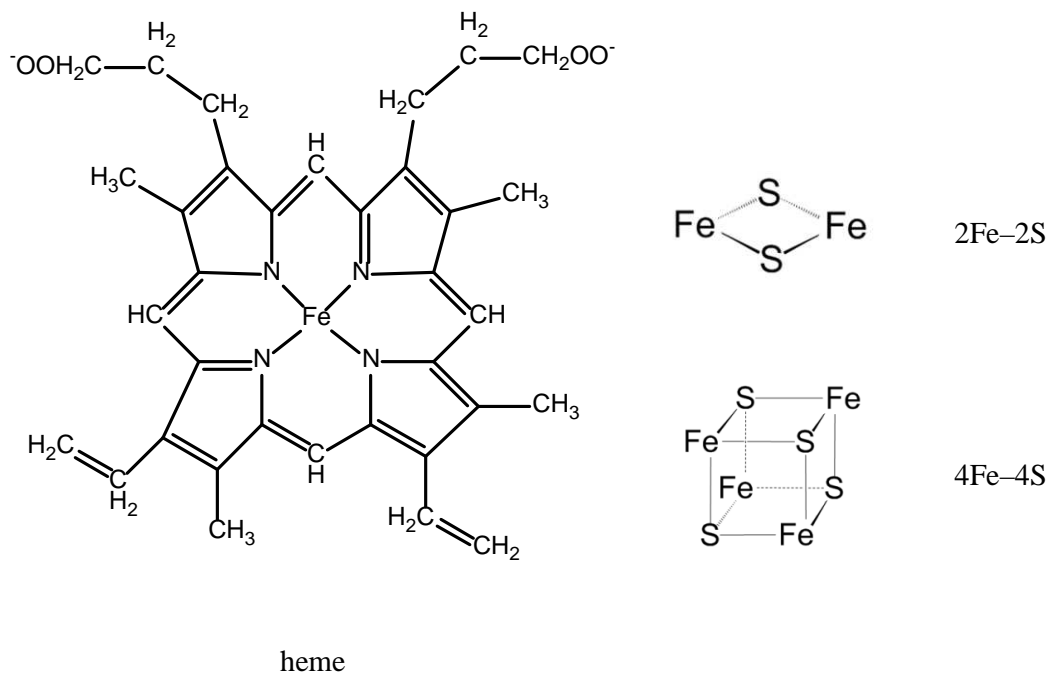


Figure 1.1. The structures of heme, [2Fe-2S] and [4Fe-4S] clusters.

The redox chemistry of iron makes it a useful cofactor for electron transfer processes, but it can also donate electrons to molecular oxygen or hydrogen peroxide to form superoxide ions and hydroxyl radicals. Under normal conditions in eukaryotic cells, less than 0.1% of electrons leak through the electron transport chain to molecular oxygen to produce the superoxide ion O_2^{\square} (10). Superoxide ions do not penetrate biological membranes, and most of the time superoxide ion is inactivated by superoxide dismutases (SOD) in mitochondria (*e.g.*, MnSOD, SOD2) or in the cytosol (*e.g.*, CuZnSOD, SOD1) by the following reaction (11):



The product, hydrogen peroxide (H_2O_2) is relatively stable compared to the lifetime of the superoxide ion, and it can diffuse through membranes into the cytosol and nucleus, where enzymes like glutathione peroxidase (in mitochondria and cytosol) or catalase (in peroxisomes) convert H_2O_2 into water and molecular oxygen (12). However, if peroxide encounters non-bound (“free”) reduced transition metals, especially Fe^{2+} and Cu^+ , it can undergo Fenton chemistry to produce the hydrogen radical (OH^{\bullet}) (13).



Due to its high reactivity, the hydroxyl radical has a very short half-life *in vivo* ($\sim 10^{-9}$ sec) (14) compared to its lifetime in the atmosphere (≤ 1 sec), and the radical will react with biological molecules such as DNA, lipids and proteins (15). Fe/S cluster containing proteins are also vulnerable to the hydroxyl radical, which can inactivate Fe/S clusters through oxidation which impairs protein function. Because the hydroxyl radical is one of the most powerful and dangerous oxidants for organisms, iron levels must be tightly controlled to avoid these adverse reactions.

1.2.2 Iron Assimilation and Homeostasis in *Schizosaccharomyces pombe*

Maintaining an appropriate concentration of biologically available ferrous iron is critical for cell viability, and imbalanced iron homeostasis greatly affects human health (16). Eukaryotic cells must acquire iron from their environment or from food, and this process is tightly regulated. Iron uptake and intracellular regulation are two very complicated processes that are easier to understand in a unicellular, eukaryotic model system like yeast. Iron homeostasis in the budding yeast *Saccharomyces cerevisiae* (*S. cerevisiae*) is well described, but distinct differences exist between budding yeast and mammalian cells. These include different iron uptake pathways, crosstalk between Fe/S cluster assembly and heme synthesis, and regulatory mechanisms (17-19). Therefore, studying iron homeostasis in the fission yeast *Schizosaccharomyces pombe* (*S. pombe*), which is evolutionarily more similar to eukaryotes (20), provides another angle to look into this critical biological process.

Fission yeast has two distinct iron uptake pathways as shown in **Figure 1.2**. The first pathway is the non-reductive iron uptake of ferrichrome-chelated iron. Ferrichrome is a cyclic siderophore (*i.e.*, extracellular metal scavenger) that chelates iron with high affinity using oxygen and nitrogen ligands (**Figure 1.2A**) (21). This intact chelate molecule is brought into the cell by Str1/2/3 transport proteins (17). The other pathway is reductive iron transport, which is important for cell viability in iron-deficient conditions (**Figure 1.2B**) (22). The ferric reductase Frp1 is found on the surface of *S. pombe* cellular membranes. Frp1 reduces environmental Fe³⁺ to Fe²⁺, which is transported through the membrane by the high affinity iron uptake pathway composed of Fio1 and Fip1 proteins or by the metal transporter Fet4 (17). The O₂ concentration in the environment determines which elemental iron uptake pathway is used (22). Under aerobic

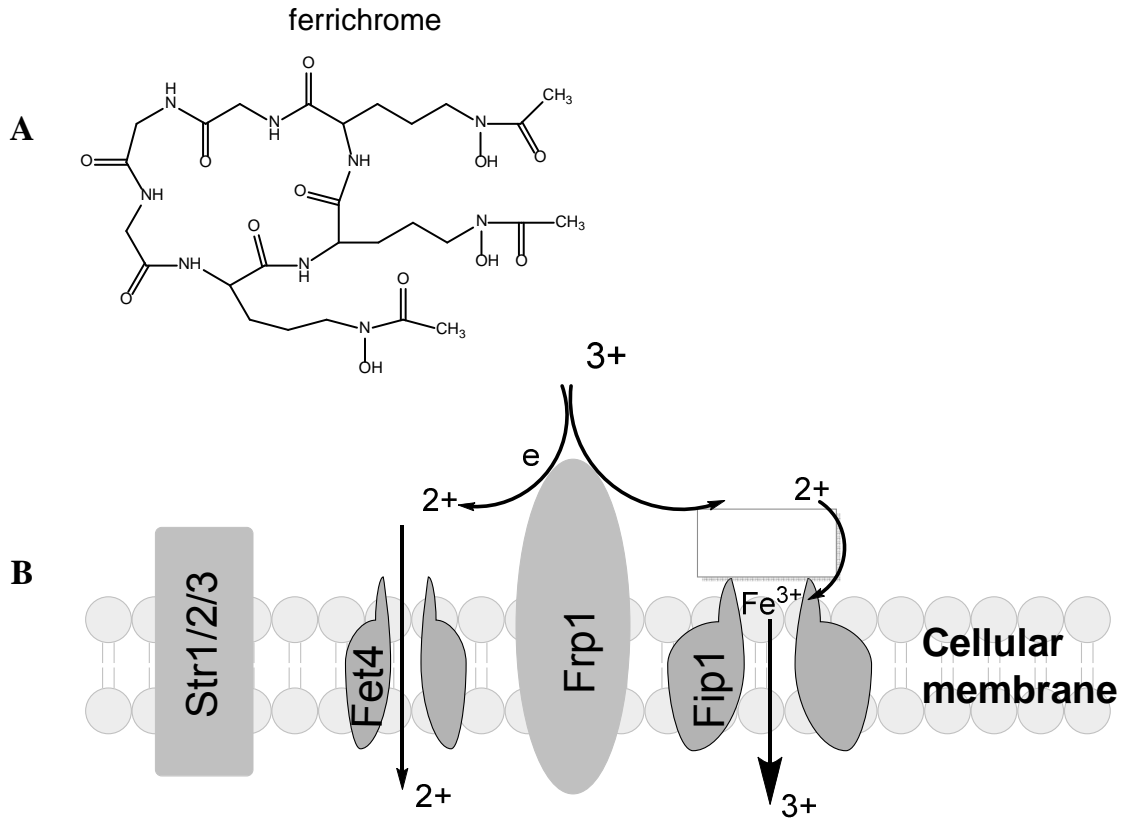


Figure 1.2. The iron uptake pathways of *S. pombe*. (A) Str1/2/3 proteins are the siderophore transport channels. (B) Fet4 is a divalent metal transporter, Frp1 is the membrane ferric reductase, and Fio1/Fip1 is the high affinity iron uptake pathway (17).

conditions, the Fio1/Fip1 high-affinity iron import system is the primary iron uptake pathway (**Figure 1.3**) and is very similar to the high-affinity iron uptake pathway in the budding yeast *S. cerevisiae* (17). In this pathway, the Fe^{2+} produced by Frp1 is oxidized to Fe^{3+} by the multicopper oxidase Fio1, but this Fe^{3+} does not equilibrate with bulk Fe^{3+} . Instead, it is transported into the cell by the associated Fip1 transmembrane iron permease (22). The activity of this pathway is up-regulated by iron depletion to restore intracellular iron concentrations as needed (23). Under anaerobic conditions, Fe^{2+} (supplied by Frp1) is transported through the non-specific divalent metal ion transporter Fet4, which is a homologue of human NRAM1 (17). This pathway is considered to be of lower affinity and is less efficient (17).

S. pombe controls iron assimilation pathways through regulated gene expression of the proteins involved in iron uptake. The uptake genes are regulated by the Fep1 transcriptional factor and include *fio1*⁺ (ferrous iron oxidase), *fip1*⁺ (transmembrane iron permease), and *frp1*⁺ (ferrireductase) (24). As illustrated in **Figure 1.4**, when cellular iron is abundant, Fep1 represses expression of target uptake genes by binding to the “GATA” DNA motif in the operator/promoter regions upstream of these genes. This basically turns off expression since additional iron uptake is not required. When iron is depleted, Fep1 releases from the promoter of these genes, allowing for transcription and further expression of proteins required for iron acquisition (24). Evidence suggests that the Fep1 transcription factor senses and binds iron using cysteine residues, but further molecular detail is unknown at this time (23).

1.3 Iron Metabolism

After iron enters the cytosol, the iron can be stored in the protein ferritin or metabolized (**Figure 1.5**). Ferritin is a multimeric storage protein that can hold up to hundreds-to-thousands of iron atoms as an insoluble iron-oxy-hydroxide mineral core (9). Iron from ferritin can be

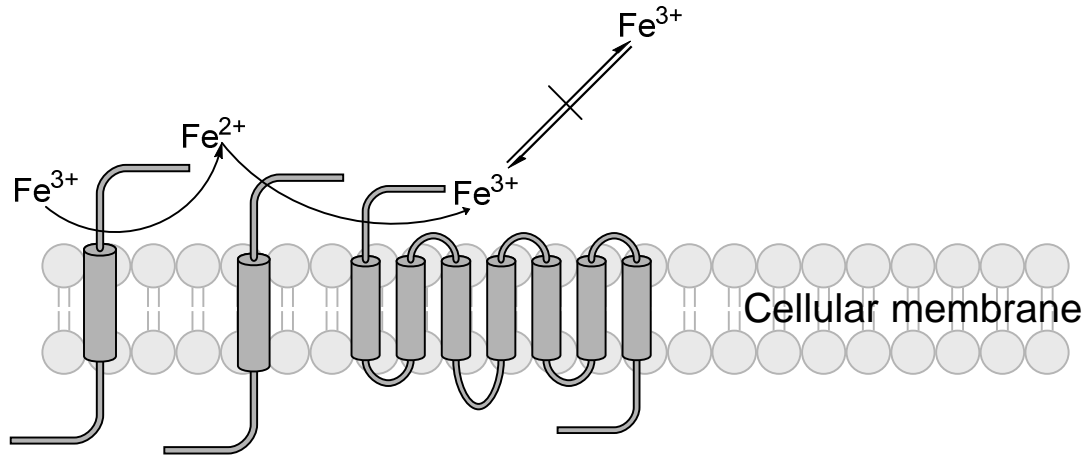


Figure 1.3. The primary iron uptake pathway of *S. pombe*, the high affinity iron import system. Environmental Fe^{3+} is reduced by Frp1, and the Fe^{2+} is oxidized back to Fe^{3+} by the ferrous oxidase Fio1. Fe^{3+} is then transported into cytosol by Fip1 without equilibrating with environmental Fe^{3+} (22).

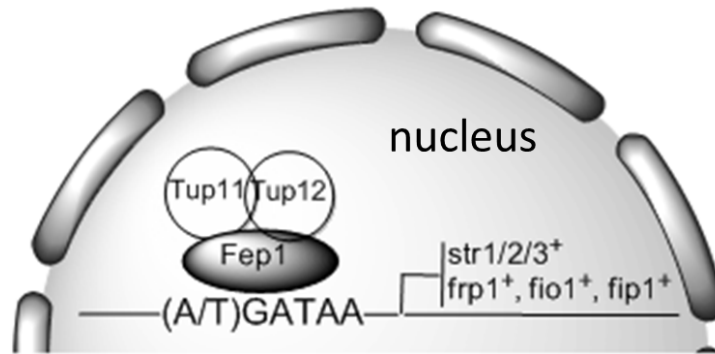


Figure 1.4. Regulation of iron homeostasis of *S. pombe* through the transcription factor Fep1. With abundant iron, Fep1 binds to the DNA sequence (A/T)GATAA and represses the transcription of genes involved in iron uptake, including *str1/2/3⁺*, *frp1⁺*, *fio1⁺*, and *fip1⁺*. Upon iron depletion, the Fep1 is released, and the transcription of iron uptake genes is increased (17).

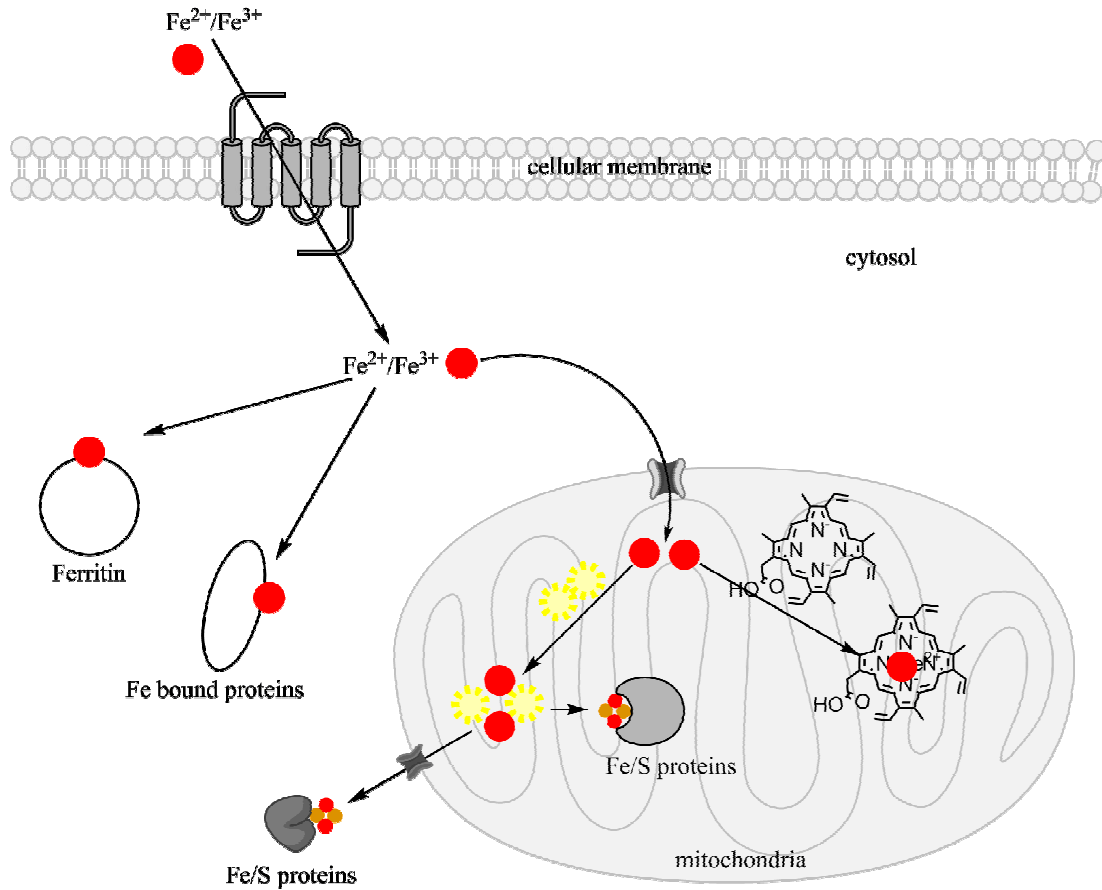


Figure 1.5. Iron metabolism in eukaryotic cells. Imported cellular iron can be stored in ferritin or bound to Fe containing proteins. Fe can also be transported into mitochondria, where it is used to synthesize Fe/S clusters and heme. Red circles (Fe), orange circles (S) (26).

utilized in Fe/S cluster synthesis and heme synthesis with unknown mechanism (25). Fe/S cluster and heme containing proteins are highly involved in energy production, detoxification, DNA replication, and other important cellular functions (27). For eukaryotic cells, most Fe/S clusters are produced in mitochondria, while the synthesis of heme can occur both in the mitochondria and the cytosol (28).

1.3.1 Heme Synthesis and Regulation

Heme is involved in various biological functions such as electron transport, detoxification, gas sensing, and signal transduction (28). The synthesis of heme is highly conserved. Seven steps are required to synthesize the protoporphyrin IX precursor, after which the enzyme ferrochelatase (FeCH) inserts ferrous iron into the porphyrin macrocycle to form heme (**Figure 1.1**). Because of the hydrophobicity of porphyrin, many enzymes in this pathway are found at or in the mitochondrial inner membrane (28). Mechanistic and structural details of how human FeCH inserts iron into protoporphyrin IX has been clarified recently (29, 30). In humans and *S. pombe*, FeCH contains a [2Fe-2S] cluster, while *S. cerevisiae* FeCH does not. Evidence suggests that the Fe/S cluster in FeCH functions as a structural cofactor and biological sensor rather than in catalysis (28). This Fe/S cluster in FeCH also suggests a direct connection between Fe/S clusters assembly and heme synthesis, the two major iron utilization pathways.

The regulation of heme synthesis enzymes is performed post-transcriptionally, especially at the rate limiting enzyme 5-aminolevulinate synthase (ALAS), which catalyzes the condensation of glycine with succinyl-CoA to form δ -aminolevulinic acid (28). It is also suggested that heme synthesis is controlled by the levels of biologically available iron and by oxygen (28). How mitochondria supply iron to heme synthesis is still not clear, but a putative

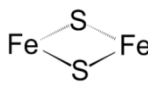
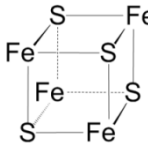
iron chaperone frataxin has been suggested to transfer iron to FeCH, although support for this is waning (31).

1.3.2 Fe/S Cluster Assembly and Regulation

There are two major types of Fe/S clusters (**Table 1.1**) and they are among the most ancient and conserved protein cofactors from archaeobacteria to humans (32). Fe/S cofactors perform many functional roles, such as catalysts, structural stabilizers and environmental sensors (32). Although the synthesis of Fe/S clusters from inorganic iron and sulfur is difficult and potentially harmful under an oxygenated atmosphere, there are many advantages of using Fe/S clusters in proteins. For example, the iron in Fe/S clusters can easily donate or accept electrons by cycling between Fe^{2+} and Fe^{3+} , which allows them to regenerate as catalysts (33). In addition, by changing the coordination environment, Fe/S clusters redox potentials can vary from -0.5 V to $+0.3$ V (9). Compared to the slow but spontaneous formation of [2Fe-2S] clusters with inorganic iron and sulfur under anaerobic condition, biological Fe/S cluster assembly is more efficient (34). Since free iron and S^{2-} are toxic to most cells (35-37), the Fe/S cluster assembly machinery contains many proteins that are responsible for supplying iron, liberating inorganic sulfur from cysteine, providing the scaffold for Fe/S clusters assembly, and transferring the Fe/S cluster to apo Fe/S proteins (**Figure 1.6**) (34).

Fe/S cluster assembly machinery is highly conserved throughout evolution, and many key component proteins are homologous from bacteria to eukaryotes. Generally, these machineries can be divided into four distinct groups: (1) nitrogen fixation systems (NIF, present in azeotropic bacteria) (36), (2) sulfur mobilization system (SUF, found in *E. coli* and plastids of plants) (36), (3) Fe/S cluster system (ISC, present in bacteria and mitochondria of eukaryotic cells) (38), and (4) cytosolic Fe/S cluster assembly system (CIA, only found in eukaryotic cells) (32). The

Table 1.1. The two major types of Fe/S clusters, their basic characteristics, and example proteins.

Cluster	Name	Formal valence	EPR value	Protein
	2Fe-2S	1Fe ²⁺ , 1Fe ³⁺	1.89, 1.95, 2.05	Human ferrochelatase
		2Fe ³⁺	–	
	4Fe-4S	3Fe ²⁺ , 1Fe ³⁺	1.88, 1.92, 2.06	Aconitase
		2Fe ²⁺ , 2Fe ³⁺	–	
		1Fe ²⁺ , 3Fe ³⁺	2.04, 2.04, 2.12	

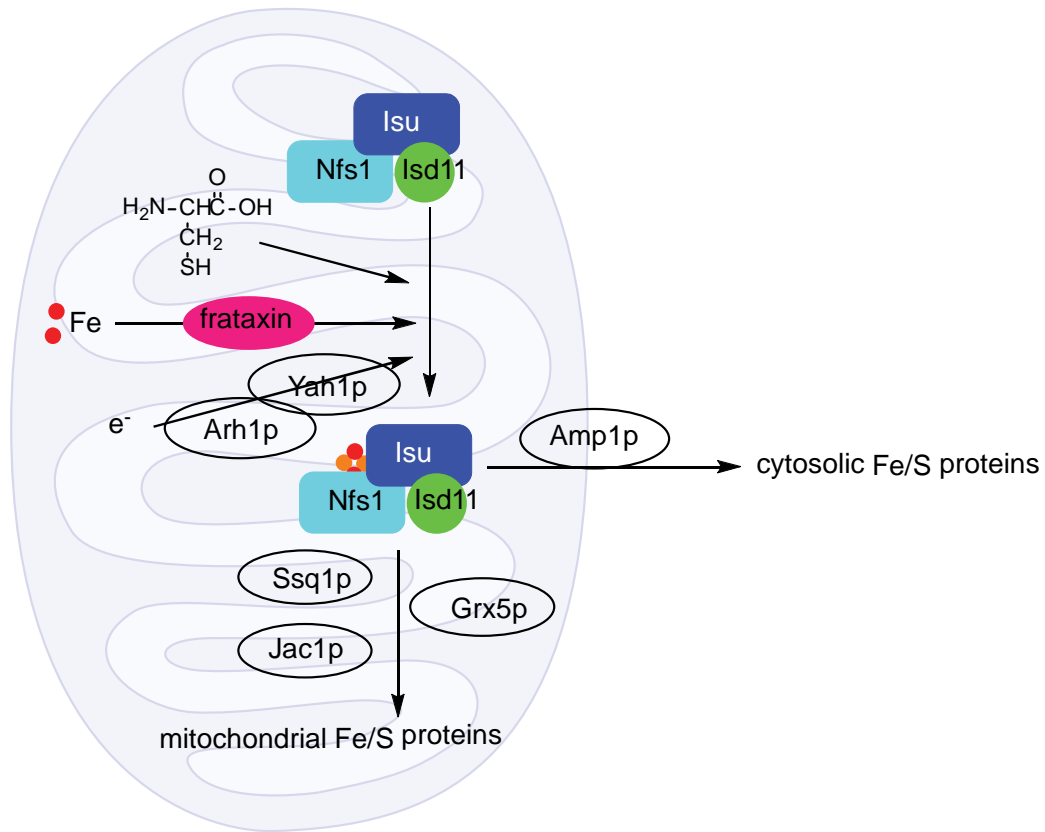


Figure 1.6. The Fe/S cluster biogenesis machinery in mitochondria. Fe²⁺ enters the mitochondria through the Mrs3/Mrs4 transporter (not shown). Fxn1 may or may not act as an iron chaperone for the Fe-S assembly complex but is involved in synthesis through its interactions with the cysteine desulfurase Nfs1, the accessory protein Isd11, and the scaffold protein Isu1 onto which the clusters are assembled. Electrons are provided by ferredoxin Yah1 and ferredoxin reductase Arh1. The insertion of Fe-S clusters requires chaperone proteins Ssq1, Jac1, and Grx5 (34).

process of Fe/S cluster assembly can be divided into three major steps in *S. pombe*, starting with the release of sulfide from L-cysteine by the cysteine desulfurase Nfs1 that requires the accessory protein Isd11. Then, the sulfur is transferred to the scaffold protein Isu1 where the Fe/S clusters are assembled using iron that may be provided by the iron chaperone Fxn1. At the final step, the mature Fe/S clusters are released from Isu1 by the chaperone system that contains Hsp70, Ssq1 ATPase, and Jac1. The glutaredoxin Grx5 may also be involved in the process (39). In mitochondria, these Fe/S clusters are transferred and inserted to apo Fe/S proteins such as aconitase and succinate dehydrogenase (35), while cytosolic and nuclear Fe/S protein maturation requires the ABC transporter Atm1 (ABCB7 in humans), which localizes in the inner membrane of mitochondria (39).

With all the important functions of Fe/S proteins, the production of Fe/S clusters is under tight control, since excess Fe/S clusters can disassemble to form insoluble iron sulfide (40). In bacteria, the regulation of Fe/S protein assembly is transcriptionally controlled by IscR (41), but an IscR homologue has not been discovered in eukaryotic systems. Instead, it is proposed in yeast that regulation occurs via the activity of the cysteine desulfurase, since the cysteine desulfuration is the rate limiting step of the pathway (42).

1.4 Human Diseases Related to Fe/S Cluster Assembly

Fe/S cluster proteins are important in most of the processes required for life, so the failure to produce enough functional Fe/S cluster proteins causes dysfunction in multiple systems, which leads to cell death or other negative effects (35). Complete deletion of genes involved in Fe/S protein assembly are always lethal at the embryonic level, while partially inactivated genes due to mutations are more common but still compatible with life (35). Mutations in genes encoding for human frataxin (*S. pombe* homolog Fxn1), GLRX5, and ISCU (*S. pombe* homolog

Iso1) are known to cause human diseases and syndromes. GLRX5 facilitates the transfer of Fe/S clusters from the scaffold to target proteins, and its deficiency (about 10% of the normal level) causes inherited human sideroblastic anemia (43). A splice mutation in the gene encoding ISCU causes an inherited skeletal muscle disease, with muscle weakness, exercise-induced acidosis, and myoglobinuria (muscle degeneration and excretion of myoglobin) (44). Biochemical examination of the affected muscle cells showed significant iron accumulation and loss of aconitase activity, a key Fe/S cluster containing enzyme in the TCA cycle. Another common disease related to Fe/S cluster assembly is Friedreich's ataxia (FRDA), which is related to reduced protein levels of the putative iron chaperone frataxin (45). Since it is more difficult to work with human cells, a yeast model system is beneficial to study these diseases. This dissertation research will use the *S. pombe* system as a model for FRDA.

1.4.1 Friedreich's Ataxia (FRDA)

FRDA is an autosomal recessive neurodegenerative disorder, and it is one of the most common autosomal recessive ataxias in Caucasians. The prevalence is 2 to 4 patients per 100,000 individuals, and 1 to 2 carriers per 100 individuals (46). The major clinical features include progressive spinocerebellar neurodegeneration, gait and limb ataxia, muscle weakness, and cardiomyopathy (47). Development of the FRDA starts during childhood, and cardiomyopathy-induced cardiac infarction is generally the cause of death. The biochemical markers of FRDA include increased cellular and mitochondrial iron content and decreased mitochondrial Fe/S cluster containing protein activity (45).

FRDA is mostly caused by an expanded GAA repeat in the first intron of the *FXN* gene (from 40–60 copies in healthy people to >200 copies in FRDA patients), which encodes the mitochondrial protein frataxin (48). Most patients are homozygous of the GAA expansion, but

about 4% are compound heterozygous with mutations (*e.g.*, nonsense, missense, deletions, insertions) (47). These genomic changes cause the reduced *FXN* mRNA levels, decreasing the functional frataxin protein level to about 5–30% of normal levels (47). The expression level of functional frataxin is related to the severity of the clinical symptoms, as patients with about 50% frataxin level show no sign of disease and the complete depletion of frataxin leads to embryonic death (49).

1.4.2 The Biochemical Characteristics of Frataxin Homologues

Frataxin is a small, but highly conserved mitochondrial protein with homologues in all eukaryotes and most prokaryotes. In eukaryotes, frataxin homologues are encoded by genomic DNA. Frataxin is imported into mitochondria, and its N-terminus is processed by the mitochondrial processing peptidase MPP1 (50-53). The alignment of full-length human frataxin (hFxn), *S. cerevisiae* frataxin (Yfh1) and *S. pombe* (Fxn1) (**Figure 1.7A**) reveals significant conservation in the C-terminal domain (54). The similarity is further demonstrated by the overlay of the three-dimensional structures of Yfh1, hFxn, and the predicted structure of Fxn1 residues 41–151 (**Figure 1.7B**) (55, 56). There is no structure of the *S. pombe* frataxin homologue, but the amino acid residues on the acidic helix and C-terminus are highly conserved, thus, it is most likely that *S. pombe* Fxn1 shares similar if not identical structure with hFxn.

Mature hFxn and Yfh1 are highly soluble monomers in the absence of iron. With excess iron and aerobic conditions, yeast Yfh1 can form oligomers *in vitro* (57, 58), and the trimeric form of Yfh1 has been suggested as the predominant species *in vivo* under stress conditions (59). However, whether oligomerization of human frataxin occurs is still under debate. When a mutant form of Yfh1 that does not form oligomers was introduced into *S. cerevisiae* without endogenous

A

```

sp|Q16595|FRDA_HUMAN      MWTLGRRVAVGLLASPSPAQAQTLTRVPRPAELAPLCGRRLRDTDIDATCTPRASSNQR 60
sp|O74831|FRDA_SCHPO     -----MQSLRAAFRRRTPIFLKPYEFS----- 22
sp|Q07540|FRDA_YEAST     ---MIKRSLASLVRVSSVMGRRYMIAAAGGERARFCPAVTNKKN----- 41
                          : .. : * :

sp|Q16595|FRDA_HUMAN      GLNQIWNVKQSVYLMNLRKSGTLGHPG----SLDETTYERLAEETLDSLAEFFEDLAD 115
sp|O74831|FRDA_SCHPO     -----TNVFGRLCRYYSQVRHNG-----ALTDLEYHRVADDTLDVLNDFEDLLE 67
sp|Q07540|FRDA_YEAST     -----HTVNTFQKRFEVSSDTGQVVPQEVLNLPLEKYHEEADDYLDHLLDSLEELSE 93
                          ..: . : * *..*::**:* :

sp|Q16595|FRDA_HUMAN      KPYTFEDYDVSFSGSVLTVKLGDLGTYVINKQTPNKQIWLSSPSSGPKRYDWTGKN--W 173
sp|O74831|FRDA_SCHPO     EVG-KKDYDIQYANGVITLMLG-EKGTYVINKQPPAHQIWLSSPVSGPKHYEYSLKSKTW 125
sp|Q07540|FRDA_YEAST     AHP-DCIPDVLSHGVMLEIP-AFGTYVINKQPPNKQIWLASPLSGPNRFDLLNGE--W 149
                          *.. **:* : *****.* :***** ** *::: :

sp|Q16595|FRDA_HUMAN      VYSHDGVSLHELLAAELTKALKTKLDLSSLAYSGKDA 210
sp|O74831|FRDA_SCHPO     CSTRDEGTLGILSSEFSKWFSPLEFKKSEDF---- 158
sp|Q07540|FRDA_YEAST     VSLRNGTKLTDILTTEEVEKAISKQ----- 174
                          :: .* :*: * * :.

```

B

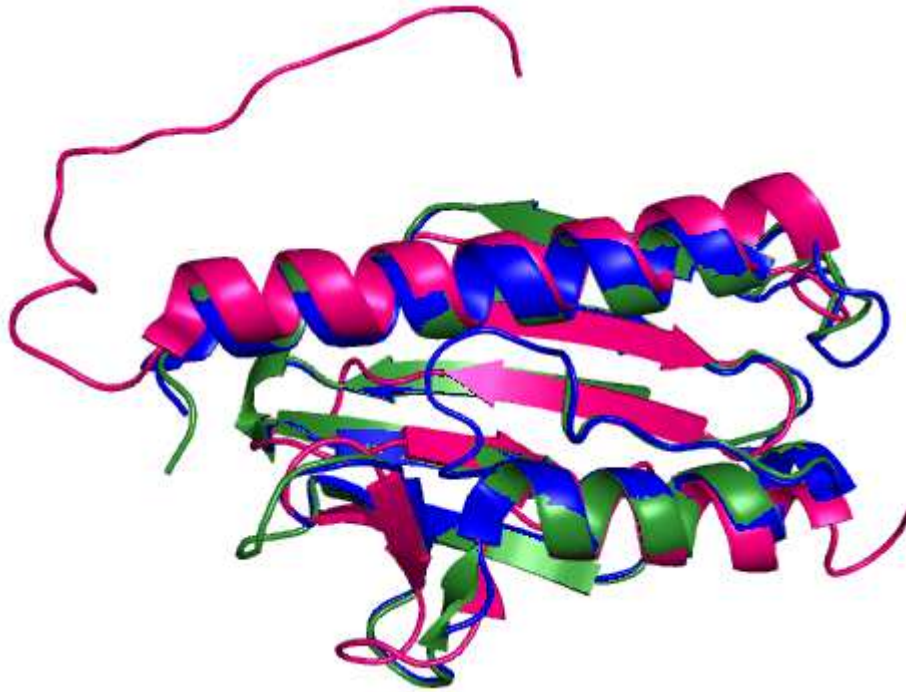


Figure 1.7. The sequences and structural alignment of frataxin homologues. (A) Sequence alignment and (B) structures of human frataxin hFxn (blue, PDB: 1EKG), *S. cerevisiae* Yfh1 (pink, PDB: 2GA5) and *S. pombe* Fxn1 model (green) (55, 56, 61).

Yfh1, the cells continued to function (60). This observation demonstrated that Yfh1 oligomerization is dispensable for function *in vivo*. As for hFxn, the mature form of hFxn⁸¹⁻²¹⁰ (residues 81–210) only exists as a monomer, while the less processed isoform hFxn⁴²⁻²¹⁰ behaves similarly to Yfh1 and can oligomerize under certain conditions (62). It is not clear if human oligomerization of frataxin is functional.

The functions of frataxin have been intensively studied during the last 15 years using *in vivo* and *in vitro* methods, and some important knowledge has been obtained. (1) Frataxin binds three metal ions with nanomolar to micromolar affinities at the N-terminus, the end of acidic ridge and the end of β_1 -strand (63). (2) Frataxin is involved in Fe/S cluster assembly (62). (3) Frataxin is important for cell viability (62). (4) Frataxin is part of the mitochondrial Fe/S cluster assembly machinery. Since frataxin is involved in FRDA, many model systems have been created, including *Saccharomyces cerevisiae*, *Caenorhabditis elegans*, *Drosophila melanogaster*, *Mus musculus* and human cell lines (64-76). The possible functions of frataxin include a key role in Fe/S protein assembly by providing iron (77) or as a modulator to regulate the activity of the Nfs cysteine desulfurase (78). Frataxin may also directly provide iron to various mitochondrial proteins, such as aconitase (79), ferrochelatase (31, 56) and succinate dehydrogenase (80). Lastly, since some frataxin homologues form oligomers in the presence of iron *in vitro*, it may also function as an iron storage protein (81).

1.5 Scope of this Section of the Dissertation Research

The goals of the studies presented in Chapter 2 of this dissertation were to: (1) construct a model system in which the *S. pombe* frataxin homologue is overexpressed in mitochondria with controlled expression levels; (2) identify the *in vivo* consequences of *S. pombe* frataxin overexpression, including the viability and other phenotypic characterizations; (3) characterize

iron homeostasis pathways in frataxin overexpressing cells, (4) elucidate the activities of some critical Fe/S cluster enzymes; and (5) gain insight into the overall function of frataxin in *S. pombe*.

CHAPTER 2

DISSECTING THE IN VIVO FUNCTIONS OF FRATAXIN IN *S. POMBE*

2.1. Introduction

The disease Friedreich's ataxia (FRDA) is an autosomal recessive neurodegenerative disorder caused by a decrease in the levels of frataxin in mitochondria (48). The biochemical hallmarks of FRDA development include significant iron accumulation, loss of activities of Fe/S cluster containing proteins (45). Frataxin is involved in Fe/S cluster synthesis, though the exact function is not fully understood (38). Most of our knowledge about frataxin function comes from FRDA model systems with reduced frataxin protein expression levels in target cells or organisms, especially the budding yeast *Saccharomyces cerevisiae* (45, 64-76). These model systems have provided excellent insight into the development of FRDA, tissue specificity, and possible functions of frataxin. However, cellular viability strongly depends on proper mitochondrial function, especially iron metabolism and iron homeostasis. It is difficult to distinguish the direct effects that of frataxin depletion from the ones caused by imbalanced iron homeostasis or disrupted iron metabolism. Thus, characterizing the phenotypes of frataxin overexpression in a simple, but well-studied organism could provide complementary knowledge to possible frataxin function.

Frataxin overexpression has been performed in *S. cerevisiae*, *Drosophila melanogaster*, and *Mus musculus* and human cell lines. The major observations are listed in **Table 2.1** (82-86). Some of the results are contradictory, which is likely due to the differences in iron homeostatic

Table 2.1. The major observations of frataxin overexpression in different organisms.

Organism/ cell lines	Overexpression level	Major observations	Reference
Human colon carcinoma	N.D.	Increased aconitase activity and oxidative metabolism	Schulz et al, 2006 (88)
Mouse embryonic fibroblast cells	2–8 fold	Activated mitochondrial respiration	Ristow et al, 2000 (87)
Mouse	N.D.	Increased aconitase activity	Pook et al, 2001 (82)
Mouse	4–10 fold	No change in systemic iron metabolism; Cardiotoxicity not relieved	Miranda et al, 2004 (83)
<i>Drosophila</i>	3–5 fold	Increased total antioxidant activity	Runko et al, 2008 (84)
<i>Drosophila</i>	N.D.	Decreased viability and life span; Decreased aconitase activity; Increased oxidative stress	Navarro et al, 2011 (86)
<i>S. cerevisiae</i>	2–18 fold	Deregulation of iron uptake; Impaired Fe/S cluster assembly and respiration; Increased resistance to oxidative stress	Seguin et al, 2009 (85)

N.D. is not determined.

and metabolic pathways or to the level of frataxin overexpression. For example, in mice frataxin overexpression did not lead to any noted negative effects (82, 83, 87, 88), while in budding yeast the overexpression caused iron accumulation, decreased aconitase activity and oxidative stress (85). The other example is that *Drosophila* frataxin overexpression lead to organ-specific effects, including resistance to oxidative stress and had longer life span (84, 86). With these possible differences in mind, the fission yeast *S. pombe* was chosen as a model organism to study the *in vivo* impacts of *S. pombe* frataxin homologue overexpression.

S. pombe shares many genes and characteristics with *S. cerevisiae*, but they are about 600 million years apart in evolution (89). *S. pombe* is considered to be more similar to mammals than *S. cerevisiae* in that its genes contains introns, it undergoes chromatin modifications, it contains RNA-dependent RNA silencing machinery, and it reproduces through binary fission (17). *S. pombe* has the smallest, fully sequenced genome in haploid eukaryotes, genetic manipulation and the cell growth conditions methods are well described, and many *S. cerevisiae* standard methods can be applied to *S. pombe* with few modifications. *S. pombe* frataxin Fxn1 is 42% identical to hFxn, and the ISC Fe/S cluster synthesis machinery in *S. pombe* is equivalent to the ISC system in humans (90). These studies will shed light onto the relationship of frataxin to Fe/S cluster biogenesis and iron homeostasis in an effort to better understand the etiology of Friedreich's ataxia.

For this dissertation research, an *S. pombe* strain was generated in which the frataxin homologue *fxn1* was overexpressed under the control of a thiamine repressible *nmt1* promoter from the plasmid pREP3X (91) to study the *in vivo* effects of Fxn1 overexpression in *S. pombe*. The high levels of Fxn1 expression caused severe cellular growth inhibition, mitochondrial dyregulation, increased oxidative stress, as well as iron accumulation and up-regulated iron

import. Despite the presence of oxidative stress in these cells, the activities of Fe/S cluster containing enzymes such as aconitase and succinate dehydrogenase were surprisingly increased. Based on this study, we conclude that Fxn1 overexpression elevated the activities of Fe/S enzymes, possibly through the up-regulation of Fe/S cluster synthesis and led to imbalanced iron metabolism. These changes in iron homeostasis lead to increased oxidative stress and loss of mitochondrial function. This research supports that mitochondrial Fxn1 up-regulates the efficiency of Fe/S cluster assembly.

2.2 Materials and Methods

2.2.1 Materials

Thiamine, uracil, ascorbate acid and hydrogen peroxide were purchased from Fisher (Fairlawn). Edinburgh Minimal Media (EMM) was purchased from MP Biomedicals (Solon). Glucose, sodium citrate, HPLC water, and triton X-100 were obtained from EMD Millipore (Billerica). Adenine and manganese chloride were purchased from ACROS Organics (Ward Hill). The BCA assay kit was obtained from Thermo Pierce (Rockford), the iron standard solution from Perkin Elmer (Shelton) and the SOD activity assay kit from Sigma. The catalase activity assay kit was obtained from Cayman Chemical.

2.2.2 Yeast Strains and Cell Cultures

Schizosaccharomyces pombe strain used in this study was wild-type SP870 ($h^{90} ade6-210 leu1-32 ura4-D18$) (from D. Beach). *S. pombe* transformants were grown in the Edinburgh Minimal Media (EMM) with 250 mg/L adenine and uracil each (EMM+AU). *S. pombe* cells were transformed with indicated plasmids using the standard lithium acetate procedure (92).

2.2.3 Plasmid Construction

Plasmids used in this study were pREP3X (93), pREP3X/Fxn1, pREP3X/Fxn1 Δ 2–11, pREP3X/Fxn1–6His, pDeut/6His–Fxn1 and pREP4X/Isu1. The coding sequences of *fxn1* and *isu1* were amplified from *S. pombe* genomic DNA by PCR and ligated into respective vectors to produce the recombinant plasmids. Plasmids pREP3X/Fxn1 Δ 2–11 and pREP3X/Fxn1–6His were constructed by deleting the base pairs encoding amino acids residues 2–11 in the *fxn1* sequence or inserting the CATCATCATCATCAT (6His) sequence at the 3'-end of *fxn1* in pREP3X/Fxn1, respectively, using QuikChange Lightning site-directed mutagenesis (Agilent Technologies).

2.2.4 Co-transformation of pREP3X/Fxn1 and pREP4X/Isu1 into *S. pombe*

The plasmids pREP3X/Fxn1 and pREP4X/Isu1 were mixed in a 1:1 ratio (w/w), and 1 μ g was added to chemically induced *S. pombe* competent cells (92). The colonies were selected and maintained on the EMM+A agar with 50 μ M thiamine.

2.2.5 Overexpression of Fxn1

S. pombe cells transformed with plasmids pREP3X, pREP3X/Fxn1 or pREP3X/Fxn1–6His were maintained on the EMM+AU agar medium with 50 μ M thiamine. Each transformant was grown overnight in EMM+AU with 50 μ M thiamine at 30 °C with shaking to mid-log phase. Cells were harvested with centrifugation, and the cell pellets were washed twice with EMM+AU before inoculation into fresh EMM+AU medium containing 50 μ M, 50 nM or 10 nM thiamine (94). All cultures were grown at 30 °C for 72 h, and cells were inoculated into new culture when necessary to maintain a cell density of $\leq 1 \times 10^7$ cells/mL. Samples for all assays are prepared from the final cultures unless specifically indicated.

2.2.6 Purification of Fxn1–6His from *S. pombe*

Cells transformed with pREP3X/Fxn1–6His were cultured in EMM+AU with 50 nM thiamine for 72 h until mid-log phase, and the cells were harvested with centrifugation at 3000×g for 2 min at 4 °C. The cell pellets were resuspended with basic buffer (50 mM NaH₂PO₄, 300 mM NaCl, and 5 mM βME, pH 7.0) to a final density of 2×10⁹ cells/mL. Cells were lysed with vigorous vortex with acid-washed glass beads at 4 °C and centrifuged at 12000 rpm for 3 min at 4 °C. The supernatant was incubated with HisPur Cobalt resin (Thermo) overnight at 4 °C with gentle shaking. The Fxn1-6His protein was eluted with 150 mM imidazole in basic buffer per manufacturer's instructions. The protein was desalted with a Millipore C18 Ziptip (Billerica) and eluted in 50% acetonitrile with 0.1% formic acid. The eluted protein was mixed into 6 mg/mL dihydroxybenzoic acid (DHB) matrix with 1:5 ratio and spotted on a stainless steel target. The Brüker Ultraflex MALDI-ToF mass spectrometer was calibrated with a standard protein mixture. The mass spectra of Fxn1–6His was collected and averaged at 60% laser power. Spectra were analyzed by flexAnalysis v3.3 (Brüker Daltonics).

2.2.7 Serial Dilution Growth Assays

Growths of transformants were analyzed with serial dilution spotting assays. An overnight culture was set up for each transformant in EMM+AU with 50 μM thiamine at 30 °C and grown to mid-log phase, then cells were washed twice with EMM+AU and inoculated into EMM+AU culture for 24 h at 30 °C with shaking. The cultures were washed and serial diluted to 1×10⁷, 2×10⁶, 4×10⁵, 8×10⁴, and 1.6×10⁴ cells/mL, respectively. Three microliters of diluted samples were spotted on EMM+AU agar plates supplied with additional chemicals and thiamine, as indicated. Photographs were taken after five days of aerobic or anaerobic growth in an O₂-deficient chamber at 30 °C.

2.2.8 Respiration Assays

The respiration rates of the transformants with 50 μ M, 50 nM or 10 nM thiamine were measured with Strathkelvin Model 782 dissolved oxygen measuring system coupled with Clark-type microcathode oxygen electrode (North Lanarkshire, Scotland) (95). The instrument was calibrated before use. One milliliter (1×10^7 cells/mL) of each final culture was added to the cuvette and the oxygen concentration was recorded when the reading was stable and again after a 5 min incubation. The oxygen consumption rate was calculated as ng/(mL·min) per 10^6 cells.

2.2.9 Quantitative RT-PCR

Three transformants of pREP3X and pREP3X/Fxn1 were each cultured in EMM+AU with 50 μ M, 50 nM or 10 nM thiamine for 72 h at 30 °C. The extraction of total RNA from the final cultures was performed with the Ambion RiboPure Yeast kit (Austin, TX). The RNA concentration and purity was determined by an Agilent 8453 UV-visible spectrometer, with $A_{260}/A_{280} \geq 2.1$, $A_{260}/A_{230} \geq 1.5$. The integrity of purified RNA was verified by a 1.5% TAE-agarose gel. The synthesis of cDNA from 1 μ g extracted total RNA was performed using the Quanta qScript cDNA synthesis kit (Gaithersburg, MD). Quantitative PCR was performed using the Quanta PerfeCta SYBR Green Supermix in a Bio-Rad MyiQ real-time PCR detection system (Hercules, CA). The primers for genes are listed as **Table 2.2**. The cycling conditions were 95 °C for 3 min followed by 40 cycles of 95 °C for 10 sec, then 58 °C for 30 sec. After each run, a melt curve analysis was performed to ensure a single PCR product was amplified and detected. Three technical replicates were performed for each sample. The relative expression levels were determined by threshold cycle (C_t) value, which was calculated using the actin gene *act1* as the housekeeping gene (96) according to equations 1 and 2 (97).

Table 2.2. The primers used in qRT-PCR experiments.

Gene		Sequence
<i>act1</i>	Forward	5'- AACCCCAAATCCAACCGTGAG -3'
	Reverse	5'- CGACCAGAGGCATACAAAGAC -3'
<i>fxn1</i>	Forward	5'- ATCCCCAGTA AGTGGTCCC -3'
	Reverse	5'- TCGCTCGATAAGATTCCTAGTAG -3'
<i>acon1</i>	Forward	5'- TAAACCGTCCTCTCACATATTCA -3'
	Reverse	5'- GCATCCTGACAAGCAACACG -3'
<i>sdh1</i>	Forward	5'- TCAAGCCAGCCTTTAAGAGC -3'
	Reverse	5'- CAGTATGGGACCTCGTAGGA -3'
<i>sdh2</i>	Forward	5'- GAGCAAGATCCTACCTTAACG -3'
	Reverse	5'- AATATTCATCGCACAAGACCCG -3'
<i>isu1</i>	Forward	5'- CTTCTCTTCTTGCCCGTCCA -3'
	Reverse	5'- GTACCCACATTCCGAGGATTG -3'
<i>nfs1</i>	Forward	5'- CGTATGGACAAACCTTCAATGAG -3'
	Reverse	5'- GATAGTCGAGAGGAGAGGTAG -3'
<i>isd11</i>	Forward	5'- AACATCAAAGCTTTTTCCATACACC -3'
	Reverse	5'- CTTCGCAGGATCACTTTC AAC -3'
<i>sod1</i>	Forward	5'- GTGTCGTTACTTTTGAACAAGTC -3'
	Reverse	5'- AGGACCAGCAGAGGTACAAC -3'
<i>sod2</i>	Forward	5'- CTTACAATGCACTTGAACCTGC -3'
	Reverse	5'- ATCGGCCAGCTTCTCCTGA -3'

$$\Delta\Delta C_t = [C_{t(\text{gene})} - C_{t(\text{actin})}]_{(\text{Fxn1})} - [C_{t(\text{gene})} - C_{t(\text{actin})}]_{(\text{pREP3X})} \quad (1)$$

$$\text{Relative mRNA expression} = 2^{-\Delta\Delta C_t} \quad (2)$$

2.2.10 Preparation of *S. pombe* Whole Cell Lysates

Cells of pREP3X or pREP3X/Fxn1 transformants from the final cultures were harvested by centrifugation at 3000×g for 5 min at 4 °C, then the cell pellets were resuspended with Chelex-treated PBS buffer (pH 7.4) with 1 mM PMSF and 1 mM benzamidine to a final density of 2×10⁹ cells/mL. Cells were vigorously vortexed with acid-washed glass beads at 4 °C, and insoluble parts were removed with centrifugation at 12,000 rpm for 2 min at 4 °C. The total protein concentration of the cell lysates was determined by the Thermo Pierce bicinchoninic acid (BCA) assay.

2.2.11 Western-blot Analysis

Isolated mitochondria containing 10 µg total protein was resuspended with 0.5% tween-20 and 10% glycerol and separated on a 15% SDS-PAGE gel. The proteins were transferred to a Whatman Protran nitrocellulose membrane with a Bio-Rad Mini Trans-Blot electrophoretic transfer cell (Hercules, CA). The membrane was blocked with 5% BSA, and Fxn1-6His was detected with mouse monoclonal His-tag primary antibody (Abgent, San Diego, CA) and goat anti-mouse IgG/alkaline phosphatase conjugate secondary antibody (Southern Biotech, Birmingham, AL) using NBT/BCIP staining. Analysis of Fxn1-6His expression levels and distribution was performed using the UVP MultiDoc-It imaging system (Upland, CA) and ImageJ software (<http://rsbweb.nih.gov/ij/>).

2.2.12 Isolation of *S. pombe* Mitochondria

Mitochondria were purified from pREP3X or pREP3X/Fxn1 transformants grown in 50 µM, 50 nM, or 10 nM thiamine for 72 h. Mitochondrial isolation was performed according to

Chiron *et al.* with few changes (98). Purified mitochondria were resuspended in 10 mM imidazole (pH 6.4) with 0.6 M sorbitol. Total protein concentration of the cell homogenate, the homogenate post-mitochondrial separation, and the isolated mitochondria were determined by a BCA assay.

2.2.13 Iron Content Analysis

Total iron content of cell lysate and mitochondria was determined with a bathophenanthrolinedisulfonic acid (BPS) method with minor modifications (99). For cellular iron content, final cultures containing 1×10^8 cells from transformants grown in 50 μ M, 50 nM or 10 nM thiamine were lysed with glass beads and the final volume of lysate was adjusted to 200 μ L each. One hundred microliters of each sample was acidified with 60 μ L of concentrated HCl and heated at 100 °C for 15 min. For mitochondrial analysis, 0.5 mg of isolated mitochondria in each thiamine condition were disrupted with 0.5% Triton X-100 in Chelex-treated water up to 100 μ L and incubated on ice for 5 min. Samples were acidified with 60 μ L concentrated HCl and heated at 100 °C for 15 min. Precipitate was removed by centrifugation at 14000 rpm for 5 min. Then, 100 μ L of supernatant was added to 650 μ L of 0.5 M Tris-HCl (pH 8.5), 100 μ L of fresh 5% ascorbate, and 200 μ L of 0.1% BPS. The sample was incubated for 1 h at 23 °C, and the total iron concentration was determined by the absorbance at 535 nm using Agilent 8453 UV-visible spectrophotometer. A standard calibration curve was prepared from a serial dilution of iron ranging from 4.5 μ M to 107.4 μ M using a calibrated iron standard solution.

2.2.14 Aconitase Activity Assay

Mitochondrial aconitase activity was determined as describe by Pierik, A.J. *et al.* (39). Twenty five micrograms of isolated mitochondria were resuspended with 100 μ L of ice cold buffer (50 mM Tris-HCl, 0.5 mM $MnCl_2$, 30 mM sodium citrate, 0.5% triton X-100, pH 7.4).

Fifty microliters of the resuspended mitochondria was mixed with 50 μL of 50 mM Tris-HCl, 0.5 mM MnCl_2 , 1 mM sodium citrate, and 1 mM L-cysteine at pH 7.4 and loaded to Greiner Bio one 96-well plate (Monroe, NC). The reaction was initiated with 100 μL of 5 mg/mL NADP^+ with 8 units/mL isocitrate dehydrogenase in HPLC water. The formation of NADPH was monitored by the absorption at 340 nm for 30 min at 37 $^\circ\text{C}$ using a BioTek Synergy 2 Multi Detection microplate reader (Winooski, VT). The extinction coefficient for NADPH is $\Delta\epsilon_{340} = 0.06622 \mu\text{M}^{-1}\text{cm}^{-1}$.

2.2.15 Succinate Dehydrogenase Activity Assay

Mitochondrial SDH activity was determined as described by Ackrell, B.A. *et al.* with few modifications (100). Fifty micrograms of isolated mitochondria was added to 890 μL ice cold buffer (50 mM Tris-HCl pH 7.4, 10 $\mu\text{g}/\text{mL}$ antimycin A, 1 mM CaCl_2 , 1 mM KCN, 8 mg/mL sodium succinate) and incubated for 5 min. The solution was rapidly heated to 37 $^\circ\text{C}$ in a quartz cuvette. The reaction was initiated with 100 μL of 0.33% phenazine methosulfate (PMS) and 10 μL of 1% 2, 6-dichlorophenolindophenol (DCIP) at 37 $^\circ\text{C}$. Absorbance at 600 nm was monitored with Cary 100 UV-visible spectrophotometer (Santa Clara, CA) for 15 min. The decrease in absorbance at 600 nm was related to the reduction of DCIP using $\Delta\epsilon_{600 \text{ nm}} = 0.021 \mu\text{M}^{-1}\text{cm}^{-1}$.

2.2.16 Superoxide Dismutase and Catalase Activity Assays

Total superoxide dismutase activity was determined with the Sigma SOD activity assay kit according to product instructions using Greiner Bio one 96-well plates and a BioTek Synergy 2 Multi Detection microplate reader. Each reaction contained $\sim 5 \mu\text{g}$ of total protein from each transformant lysate. The absorbance at 450 nm was monitored for 30 min, and the SOD activity was normalized to the amount of total protein in the reaction.

The total catalase activity was determined with a Cayman Chemical catalase assay kit (Ann Arbor, MI), following the provided protocol. Each reaction contained ~2 μg of total protein from cell lysate. The formation of formaldehyde was followed at 540 nm. One unit for catalase activity equals to the production of 1 nmol/mL formaldehyde per min, and results are normalized to the total protein amount.

2.2.17 Expression and Purification of Fxn1 from *E. coli*

The plasmid pDeut/6His-Fxn1 was transformed into BL21(DE3)/pLysS competent cells and selected on Luria Bertani (LB) agar supplied with 50 $\mu\text{g}/\text{mL}$ kanamycin and 34 $\mu\text{g}/\text{mL}$ chloramphenicol. Colonies were inoculated into 1 L of LB liquid medium containing 50 $\mu\text{g}/\text{mL}$ kanamycin and 34 $\mu\text{g}/\text{mL}$ chloramphenicol. Cells were allowed to grow at 37 °C with vigorous shaking until the OD_{600} reached 0.8, when IPTG was added to a final concentration of 0.2 mM. Cells were incubated for another hour at 37 °C and harvested by centrifugation at 4 °C.

All following purification steps were performed strictly on ice or 4 °C and all buffers are ice cold. The pelleted cells were resuspended into Buffer M (50 mM MES, 100 mM NaCl, 5 mM βME , pH 5.8) supplied with 1 mM PMSF. The resuspended cells were lysed with a Branson Sonifier with an output of 3.5, 50% duty cycle for total of 12 min. The insoluble fraction was removed with centrifugation at 12,000 rpm for 20 min and the supernatant was incubated with 0.015% (v/v) of polyethyleneimine (PEI) for 1 h on ice with gentle stirring. The precipitation was removed by centrifugation at 12,000 rpm for 20 min and Fxn1 remained in the supernatant, which was subjected to ammonium sulfate precipitation at 30% saturation. The precipitate was removed, and additional ammonium sulfate was added to the supernatant until 60% saturation. The precipitated protein contained 6His-Fxn1 and was resuspended and dialyzed against fresh Buffer M to remove ammonium sulfate. The dialyzed protein was loaded on a 50 mL SP

Sepharose Fast Flow column pre-equilibrated with Buffer M. The column was washed with 100 mL of Buffer M and the protein was eluted with a 100 mL of NaCl gradient (100–500 mM) in Buffer M. The protein concentration in each fraction was measured with a UV-visible spectrophotometer at 280 nm, and the fractions with $A_{280} \geq 0.4$ were analyzed by SDS-PAGE. The fractions containing pure Fxn1 were combined and dialyzed against Buffer H (50 mM HEPES, 400 mM NaCl, 5% glycerol, pH 7.4, degassed) inside an anaerobic glovebox to remove reducing agents. Trypsin digestion and MALDI-ToF mass spectrometry identified the protein as Fxn1.

2.2.18 Sulfo-SBED Labeling and Crosslinking Reactions

The purified hFxn and hISCU used in this experiment were provided by Leslie Gentry. All following procedures were performed in an anaerobic glovebox. One milligram of sulfo-SBED was resuspended in 25 μ L dimethylformamide (DMF) to final concentration of 40 μ g/ μ L. Five equivalents of the dissolved sulfo-SBED was added to either hFxn or *S. pombe* Fxn1 and the reactions were incubated in dark at 20 °C for 1 h. The mixture was desalted through a column to remove unreacted sulfo-SBED (Thermo). The crosslinking reactions were performed with a UV lamp at 365 nm, and two sets of each reaction were prepared. Mitochondria isolated from wild-type *S. pombe* SP870 or cell homogenate was lysed with 0.5% CHAPS, and mixed with SBED-Fxn1 with 70:1 ratio (w/w). The negative control reactions to test crosslinking specificity were performed with 10 μ M SBED-hFxn and 20 μ M reduced bovine serum albumin (BSA) or 10 μ M SBED-hFxn only. The positive control reaction contains 10 μ M SBED-hFxn and 20 μ M hISCU. One set of each reaction was floated in a water bath at 4 °C. A Spectroline UV lamp (84 watt, 365 nm) was placed ~10 cm from the top of the liquid surface of reactions. The samples were exposed to UV light for 1 min, mixed, and then allowed to rest at 4 °C for 1 min for a total

UV exposure time of 16 min. The other set of reactions were protected from light and kept at 4 °C as controls.

Under subdued light, the samples were diluted 1:100 (SBED-hFxn with BSA or hISCU) or 1:50 (SBED-Fxn1 with mitochondria or cell homogenate) with chelex-treated 50 mM HEPES buffer, pH 7.4, and 10 μ L was added to 10 μ L 2 \times SDS loading dye with or without fresh β -mercaptoethanol. Proteins were separated on a 15% SDS-PAGE gel in dark for 1 h at 200 V, and then transferred to a Whatman Protran nitrocellulose membrane with a Bio-Rad Mini Trans-Blot electrophoretic transfer cell. The membrane was blocked with 5% BSA fraction V in TBS Buffer (20 mM Tris base, 140 mM NaCl, pH 7.5) for 1 h and then washed 3 times with TBSTT Buffer (TBS buffer with 0.1% Tween-20 and 0.2% Triton X-100) with agitation. The membrane was incubated with a 1:2000 diluted streptavidin-alkaline phosphatase in TBSTT with 1% BSA overnight. The membrane was washed 4 times with TBSTT and stained with 0.33 mg/mL nitrobluetetrazolium and 0.166 mg/mL 5-bromo-4-chloro-3'-indolyphosphate *p*-toluidine in 100 mM Tris-HCl, 100 mM NaCl, and 5 mM MgCl₂ until color developed.

2.2.19 Statistics

Standard Student's t-tests were performed to examine the significance of reported data.

2.3 Results

2.3.1 Cellular Growth Defect Induced by Fxn1 Overexpression

The expression of Fxn1 from the pREP3X/Fxn1 plasmid is under the control of the thiamine repressible *nmt1* promoter, which is repressed at 16 μ M thiamine and maximally de-repressed in the absence of thiamine (93). To examine the overall cellular effects of Fxn1 overexpression in *S. pombe*, the growth of transformants with pREP3X, pREP3X/Fxn1 and pREP3X/Fxn1 Δ 2–11 were analyzed with serial dilution growth assays (“spotting assays”) on

minimal media agar containing various amounts of thiamine (**Figure 2.1A**). In these experiments, 10 nM thiamine leads to the highest Fxn1 overexpression and 50 μ M thiamine the lowest. Growth is determined by the cell density of the spots after 5 days at 30 °C. Marked growth inhibition of *S. pombe* cells is correlated with the level of exogenous Fxn1 overexpression, with significant loss of cell viability when pREP3X/Fxn1 is fully de-repressed (*i.e.*, no thiamine). To test if this was specific to Fxn1 or if overexpression of other Fe/S biosynthetic proteins would lead to the same growth defect, the Fe/S cluster assembly scaffold protein Isu1 was also overexpressed. Isu1 is known to interact with Fxn1 *in vivo* to assemble Fe/S clusters (62). Interestingly, Isu1 overexpression did not lead to marked growth inhibition as observed for Fxn1 (**Figure 2.1B**), thus observed growth inhibition is specific to high levels of Fxn1. However, if Isu1 is co-overexpressed with Fxn1, the growth defect is exacerbated (**Figure 2.2**). Further, when the N-terminal Fxn1 mitochondrial targeting sequence is disrupted via deletion of residues 2–11 (Fxn1 Δ 2–11) and cannot be imported into mitochondria (101), overexpression of Fxn1 was not inhibitory to cell growth (**Figure 2.2A**) (101). These observations demonstrate that the growth defect observed is due to the increased levels of mitochondrial-localized Fxn1.

To test if mitochondrial function is compromised from Fxn1 overexpression, the cellular respiration rates of pREP3X and pREP3X/Fxn1 *S. pombe* transformants cultured in 50 μ M, 50 nM and 10 nM thiamine were determined through an oxygen consumption assay. Low to moderate Fxn1 overexpression led to a slight increase in respiratory efficiency (1.2–1.3 fold) (**Figure 2.3**). Cells that express the highest level of Fxn1 (10 nM thiamine) have a significantly decreased respiration rate (**Figure 2.3**). Since aerobic growth requires the mitochondrial electron transport chain to reduce oxygen to water and high overexpression of Fxn1 leads to respiratory

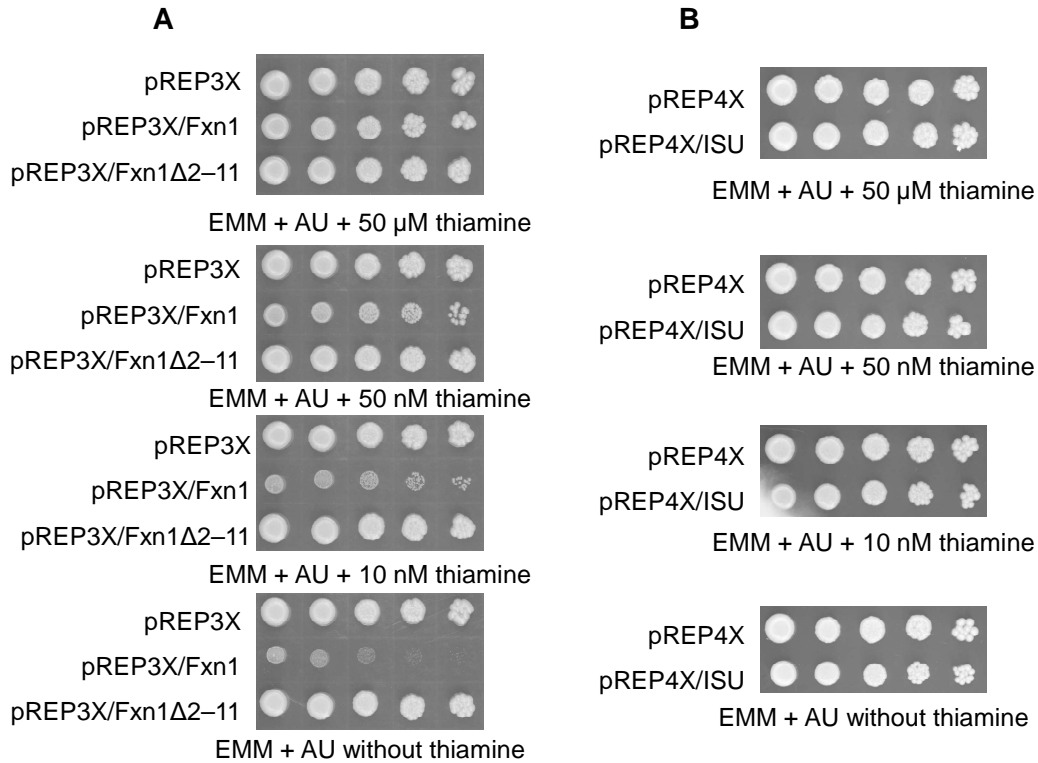


Figure 2.1. The overexpression of Fxn1 in *S. pombe* mitochondria causes cell growth

inhibition. (A) *S. pombe* wild-type cells with pREP3X, pREP3X/Fxn1 or pREP3X/Fxn1Δ2-11 were grown to mid-log phase in EMM+AU without thiamine then resuspended to 1×10^7 cells/mL. Cells were serial diluted (1:5) and 3 μL was spotted on EMM+AU with 0 nM, 10 nM, 50 nM and 50 μM thiamine, as indicated. Plates were incubated at 30 °C for 5 days. (B) *S. pombe* wild-type cells transformed with pREP4X or pREP4X/ISU were grown to mid-log phase in EMM+AL without thiamine then serial diluted (1:5). Three microliters of resuspended cells were spotted on EMM+AL with 0 nM, 10 nM, 50 nM and 50 μM thiamine as indicated. Plates were incubated at 30 °C for 5 days.

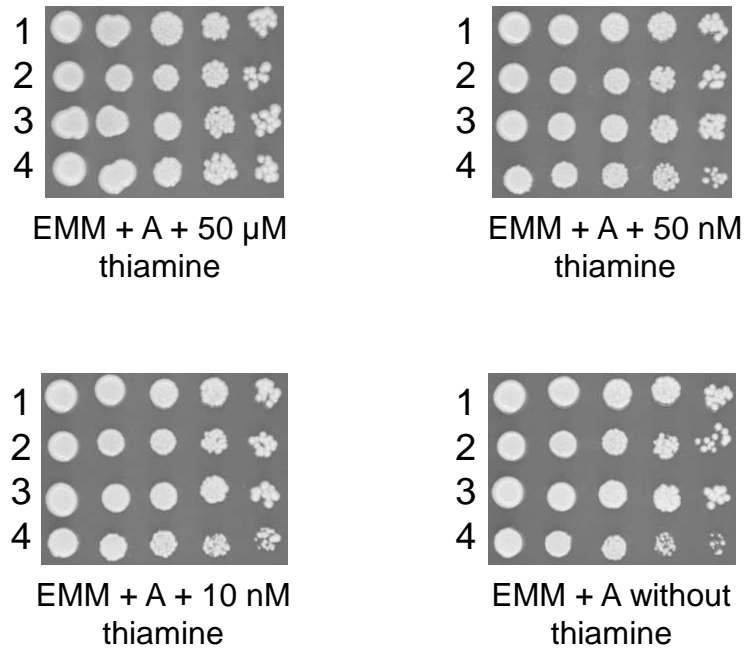


Figure 2.2. The co-overexpression of Fxn1 and Isu1 in *S. pombe* mitochondria causes exacerbated cell growth inhibition. *S. pombe* wild-type cells with the combination of pREP3X + pREP4X (lane 1), pREP3X/Fxn1 + pREP4X (lane 2), pREP3X + pREP4X/Isu1 (lane 3), or pREP3X/Fxn + pREP4X/Isu1 (lane 4) were grown to mid-log phase in EMM+AU without thiamine then resuspended to 1×10^7 cells/mL. Cells were serial diluted (1:5) and 3 μ L was spotted on EMM+A with 0 nM, 10 nM, 50 nM and 50 μ M thiamine, as indicated. Plates were incubated at 30 °C for 5 days. Due to the severe growth inhibition of Fxn1 overexpressing cells in the absence of thiamine, 10 nM thiamine was used as the maximally de-repressed condition.

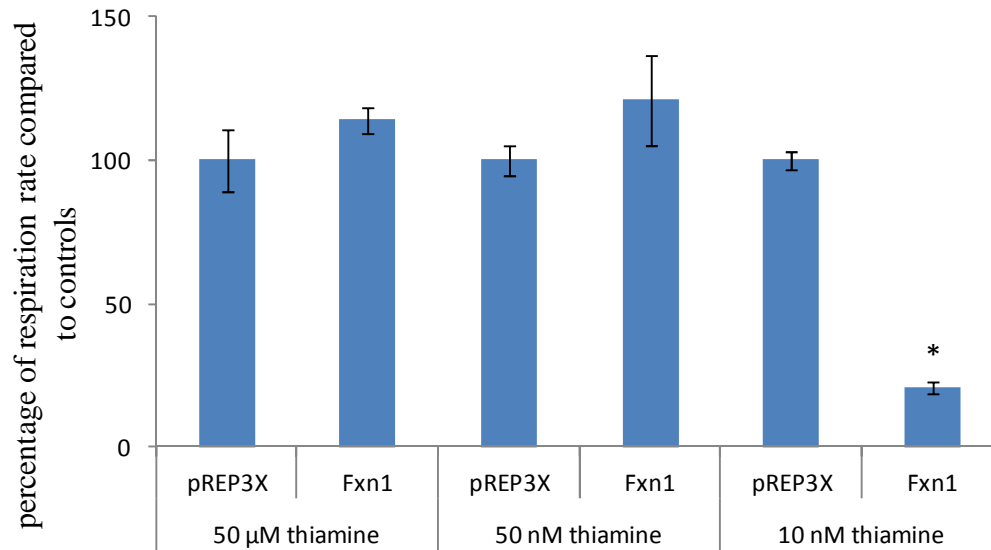


Figure 2.3. The respiration rate significantly decreased for cells with high levels of mitochondrial Fxn1. Respiration rates of 1×10^7 cells/mL of wild-type pREP3X or pREP3X/Fxn1 cells in 10 nM, 50 nM and 50 μM thiamine, as indicated, were measured using an oxygen consumption assay. The oxygen consumption rate was calculated as ng/(mL·min) per 10^6 cells. The data is normalized to the pREP3X transformants control (**p-value* < 0.05; error bars shown as S.E.M., $n \geq 4$).

deficiency, a switch to anaerobic conditions may rescue cell growth by bypassing the electron transport chain. As predicted, Fxn1 overexpressing transformants grown in anaerobic conditions have higher relative cell densities compared to cells grown aerobically (**Figure 2.4**). This indicates the growth defect of cells overexpressing Fxn1 is related to mitochondrial dysfunction, which contributes to the diminished cell viability of *S. pombe* transformants. The growth inhibition is both Fxn1 dose-dependent and dependent on mitochondrial localization.

2.3.2 Characterizing the Level of Fxn1 Overexpression and its Maturation in *S. pombe*

One way to estimate the expression levels of proteins is to measure the mRNA level of respective protein. Quantitative real-time polymerase chain reaction (qRT-PCR) is a very accurate and efficient method to measure mRNA abundance. After mRNA is extracted from cells, reverse transcriptase is utilized to produce cDNA from mRNA. The amount of *fxn1* mRNA transcript from both genomic DNA (endogenous) and pREP3X/Fxn1 plasmid (exogenous) as a function of thiamine concentration was measured with quantitative qRT-PCR (**Figure 2.5A**). Fxn1 mRNA levels are about 14-fold higher than the control pREP3X transformants at the repressible thiamine concentration of 50 μ M, suggesting that *nmt1* is a loosely controlled promoter (91). As the thiamine concentration decreases, the *fxn1* transcript increases to ~ 43-fold in 50 nM thiamine and ~ 387-fold in 10 nM thiamine.

At the protein level, western blots of *S. pombe* mitochondrial extract was probed with an antibody to the 6His-tag at the C-terminus of Fxn1 (**Figure 2.5B**). Western blots reveal that only a trace amount of the ~14 kDa Fxn1–6His protein is expressed at 50 μ M thiamine, which further suggests a leaky *nmt1* promoter. To confirm the residue composition of mature Fxn1, Fxn1–6His was recombinantly expressed from a pET vector in *E. coli*, purified by immobilized metal affinity chromatography, and analyzed by matrix-assisted laser desorption/ionization time of

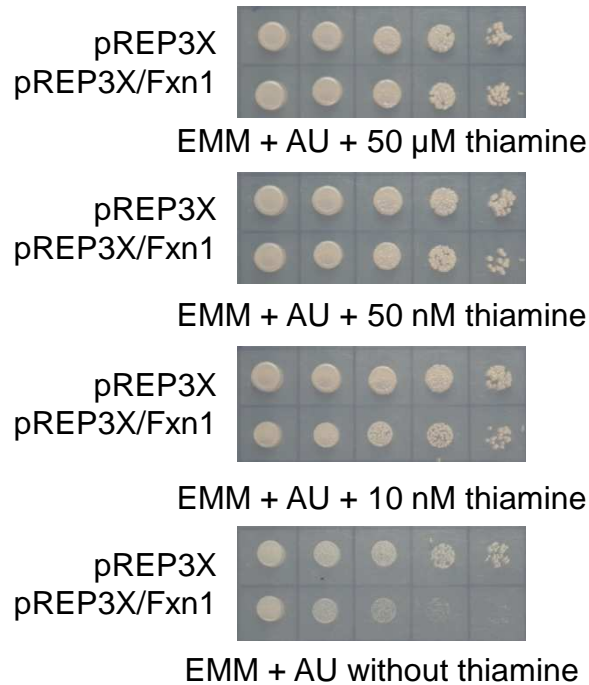


Figure 2.4. The growth defect of Fxn1 overexpression transformants was partially relieved under anaerobic growth conditions. *S. pombe* wild-type cells transformed with pREP3X or pREP3X/Fxn1 were cultured in EMM+AU without thiamine to mid-log phase and then resuspended to 1×10^7 cells/mL. Cells were serial diluted (1:5) and 3 μ L was spotted on EMM+AU with 0 nM, 10 nM, 50 nM and 50 μ M thiamine, as indicated. Plates were incubated in an anaerobic chamber at 30 °C for 5 days.

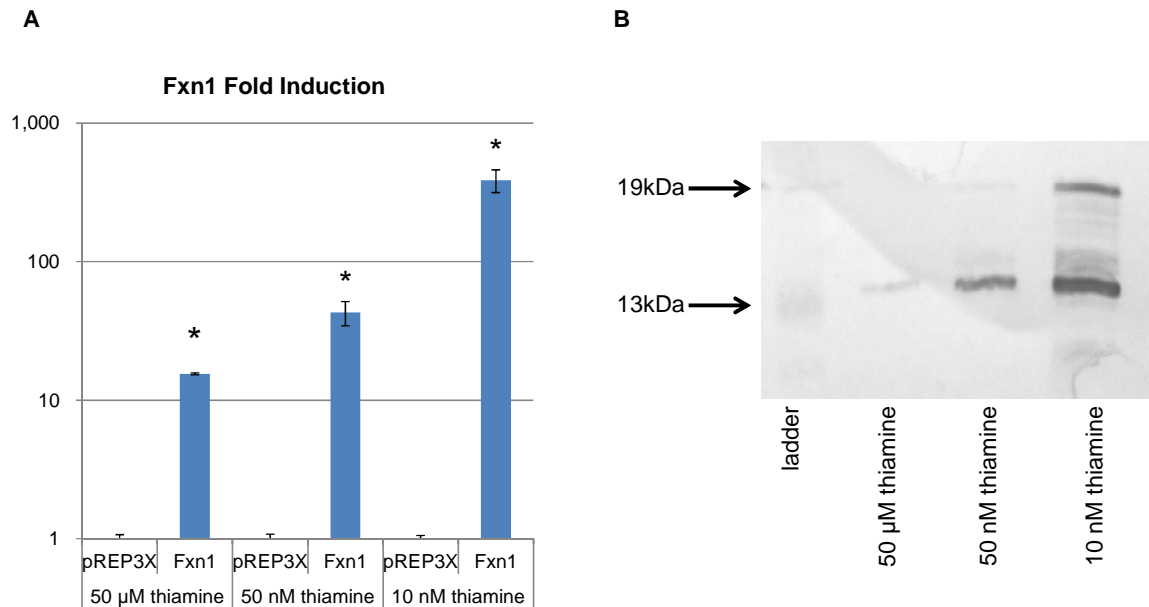


Figure 2.5. Fxn1 mRNA and protein overexpression levels. (A) The relative *fxn1* mRNA levels (both endogenous and exogenous) of pREP3X or pREP3X/Fxn1 transformants cultured in 50 μM, 50 nM or 10 nM thiamine. Standard qRT-PCR and *fxn1* specific primers were used to measure, and α actin was served as housekeeping gene (n = 3). Values were presented as fold-increase compared to control cells, as mean \pm S. E. M., *, $p < 0.05$. (B) A western blot was performed with 10 μg total mitochondrial protein isolated from pREP3X or pREP3X/Fxn1-6His transformants cultured in 10 nM, 50 nM or 50 μM thiamine. Fxn1-6His protein was visualized with an anti-His antibody and alkaline phosphatase staining. Lane 1: ProSieve pre-stain ladder; lane 2: Fxn1-6His mitochondria, 50 μM thiamine; lane 3: Fxn1-6His mitochondria, 50 nM thiamine; lane 4: Fxn1-6His mitochondria, 10 nM thiamine.

flight (MALDI-ToF) mass spectrometry (**Figure 2.6**). The molecular weight of Fxn1–6His detected by MALDI-TOF is 14,668 Da. This matches the predicted molecular weight of residues 38–158, which is now referred to as the “mature” form of Fxn1. Thus, the first 37 amino acid residues contain the mitochondrial localization sequence and are removed during maturation. As the thiamine concentration is lowered, expression of mature Fxn1–6His protein increases and a ~19 kDa non-processed isoform is clearly observed at 10 nM thiamine (**Figure 2.5B**). Thus, the overexpression of Fxn1 leads to incomplete processing to the mature form, but its abundance is relatively low compared to the 14 kDa form. High levels of Fxn1 expression caused not only the formation of a non-processed 19 kDa isoform, but also aggregation based on native PAGE (**Figure 2.7**). At this time, it is not clear which isoform causes the aggregation.

2.3.3 Fxn1 Overexpression in Mitochondria Leads to Iron Accumulation

Mitochondria are highly involved in iron metabolism and disruption mitochondrial function often leads to altered whole-cell iron homeostasis (26). Since frataxin is involved in Fe/S cluster synthesis and its deficiency leads to mitochondrial iron accumulation (64), it is possible that cellular and mitochondrial iron concentrations are also affected by mitochondrial Fxn1 overexpression. Indeed, the amount of Fxn1 overexpression correlates with the whole cell iron concentration (**Figure 2.8A**). Cells grown in 10 nM thiamine have the highest iron concentration, which is increased 10-fold over the control. Mitochondrial iron is also elevated at the highest level of Fxn1 overexpression tested (**Figure 2.8B**). Since *S. pombe* does not possess any known iron export pathway (17), the iron accumulation in Fxn1 overexpression strains is likely due to dysregulation of iron uptake and/or mobilization systems.

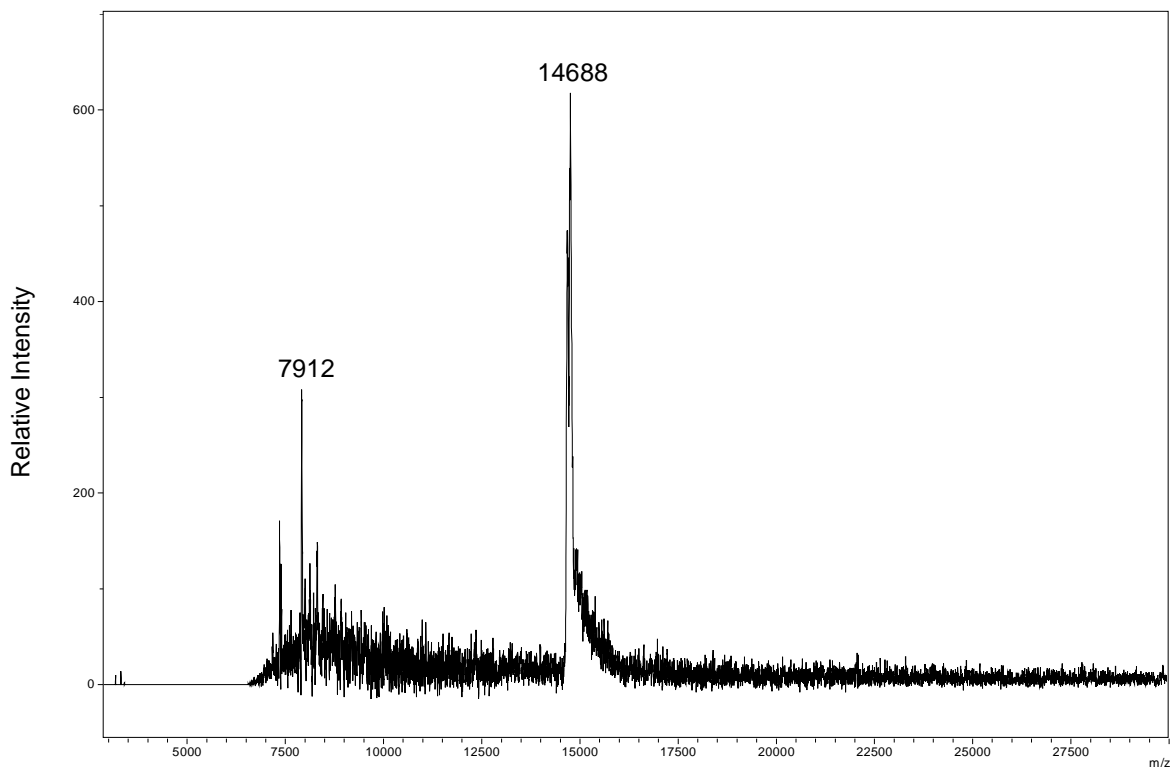


Figure 2.6. The MALDI-ToF spectrum of mature form Fxn1-6His. *S. pombe* with pREP3X/Fxn1-6His was cultured in EMM+AU with 50 nM thiamine for 3 days and the cells were lysed with glass beads. Fxn1-6His was purified with HisPur Cobalt resin following the product manual. The 150 mM imidazole elution was desalted with a C18 Ziptip and eluted in 50% acetonitrile with 0.1% formic acid. The eluted protein was mixed into 6 mg/mL dihydroxybenzoic acid (DHB) matrix with a 1:5 ratio and spotted on a stainless steel target. The mass spectra of Fxn1-6His was collected with a Brüker Ultraflex MALDI-ToF mass spectrometer and averaged at 60% laser power. Spectra were analyzed by flexAnalysis v3.3.

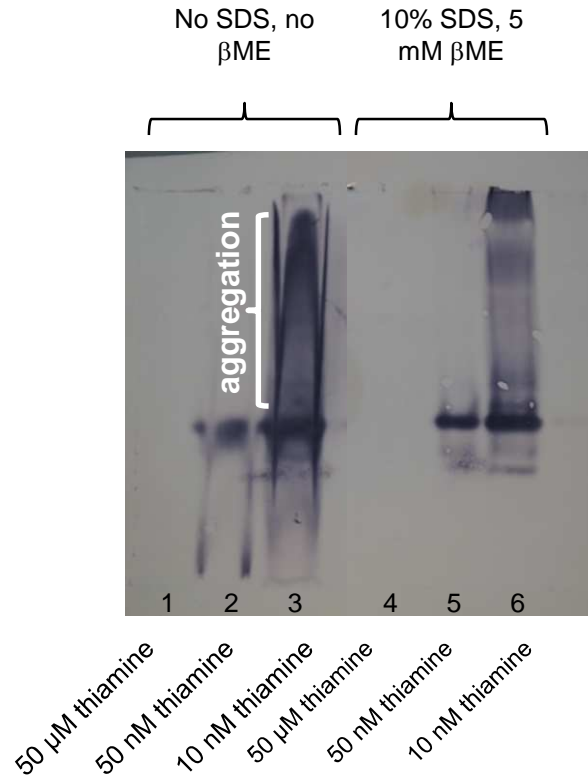


Figure 2.7. Native gel electrophoresis of Fxn1 overexpression demonstrates the existence of Fxn1 oligomers. Ten micrograms of mitochondrial extract expressing Fxn1–6His was separated by 12% native PAGE at 40 mA. Proteins were transferred to a nitrocellulose membrane, probed by an anti-His antibody, and detected with alkaline phosphatase staining. Lanes 1–3 did not contain SDS or β ME, while lanes 4–6 contained 10% SDS and 5 mM β ME. Lane 1, pREP3X/Fxn1–6His mitochondria, 50 μ M thiamine; lane 2, pREP3X/Fxn1–6His mitochondria, 50 nM thiamine; lane 3, pREP3X/Fxn1–6His mitochondria, 10 nM thiamine; lane 4, pREP3X/Fxn1–6His mitochondria, 50 μ M thiamine; lane 5, pREP3X/Fxn1–6His mitochondria, 50 nM thiamine; lane 6, pREP3X/Fxn1 mitochondria, 10 nM thiamine.

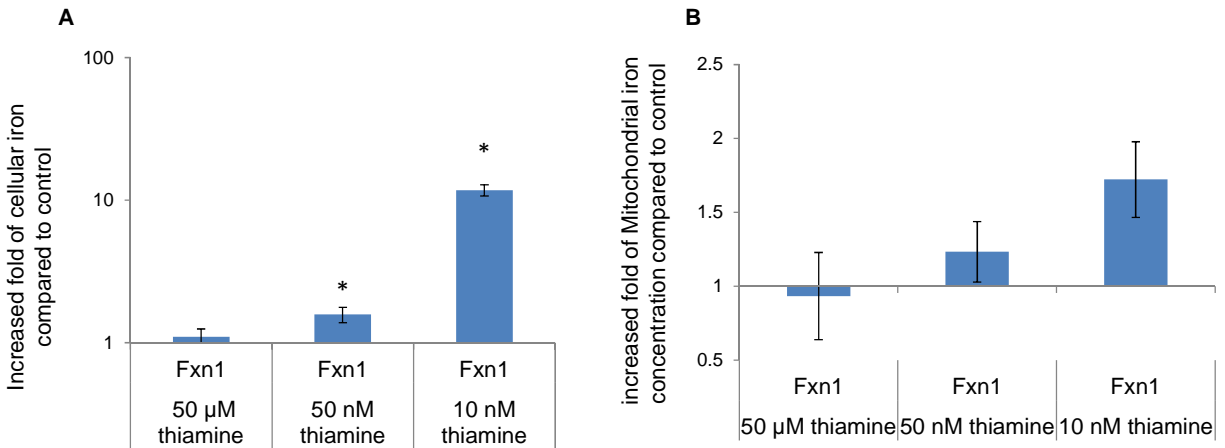


Figure 2.8. Overexpression of Fxn1 in mitochondria causes cellular iron accumulation and up-regulated iron importing system. (A) Total cellular iron was measured by a BPS assay, and normalized to cell density, and compared to the pREP3X transformants controls (asterisks indicate the *p-value* < 0.05, error bars shown as S.E.M., *n* > 5). The whole cell iron concentration increases with Fxn1 overexpression in mitochondria. (B) The mitochondria were purified for each transformant cultured in EMM+AU with 50 μM, 50 nM or 10 nM thiamine. The iron concentration was measured with the BPS method. Iron concentrations were normalized to the protein concentration and compared to the pREP3X transformants cultured under the same condition (asterisks indicate the *p-value* < 0.05, error bars shown as S.E.M., *n* > 5). Mitochondrial iron concentrations slightly increase with Fxn1 overexpression.

As discussed in Chapter 1 of this dissertation, the major of iron uptake pathway in *S. pombe* requires reduction of ferric iron (Fe^{3+}) to ferrous iron (Fe^{2+}) by the cell surface ferrireductase enzyme Frp1, whose activity is up-regulated in iron-limiting conditions (102). The specific iron chelator bathophenanthrolinedisulfonic acid (BPS), which forms a red color upon Fe^{2+} coordination, was used as a colorimetric indicator of Frp1 activity in growth assays. Even with the growth inhibition from Fxn1 overexpression, the enhanced red color of the BPS- Fe^{2+} complex is observed on the surface of Fxn1 overexpression cells, compared to the control strains (**Figure 2.9A**). It is especially noticeable at the moderate overexpression level (50 nM thiamine), where the growth inhibition is not as severe. This observation demonstrates that Fxn1 overexpression led to increased Fe^{3+} reduction at the cell surface, probably by Frp1, which suggests up-regulated iron uptake. When the same spotting assay was performed anaerobically, the red color from BPS- Fe^{2+} is no longer visible (**Figure 2.9B**), indicating the switch from high affinity iron uptake pathway to the low affinity pathway, which is not inducible (17).

To test if the growth defect phenotype of Fxn1 overexpression cells was caused by iron accumulation, growth assays were performed in the presence of cell-impermeable and cell-permeable metal chelators. Chelators tested included ethylenediaminetetraacetic acid (EDTA), bathophenanthrolinedisulfonic acid (BPS), desferoxamine (DFO), and diethylene triamine pentaacetic acid (DTPA). Because *S. pombe* cells synthesize ferrichrome, which binds iron as a siderophore (21) and possibly as iron storage molecule (23), the tolerance of *S. pombe* to iron chelators is higher than *S. cerevisiae*. All chelators tested are inhibitory to the growth of pREP3X control cells to varying degrees; however, the growth of Fxn1 overexpressing strains is not as sensitive to the presence of metal chelators (**Figure 2.10**). Given the iron accumulation in Fxn1 overexpression cells, the presence of chelators is either mobilizing accumulated intracellular

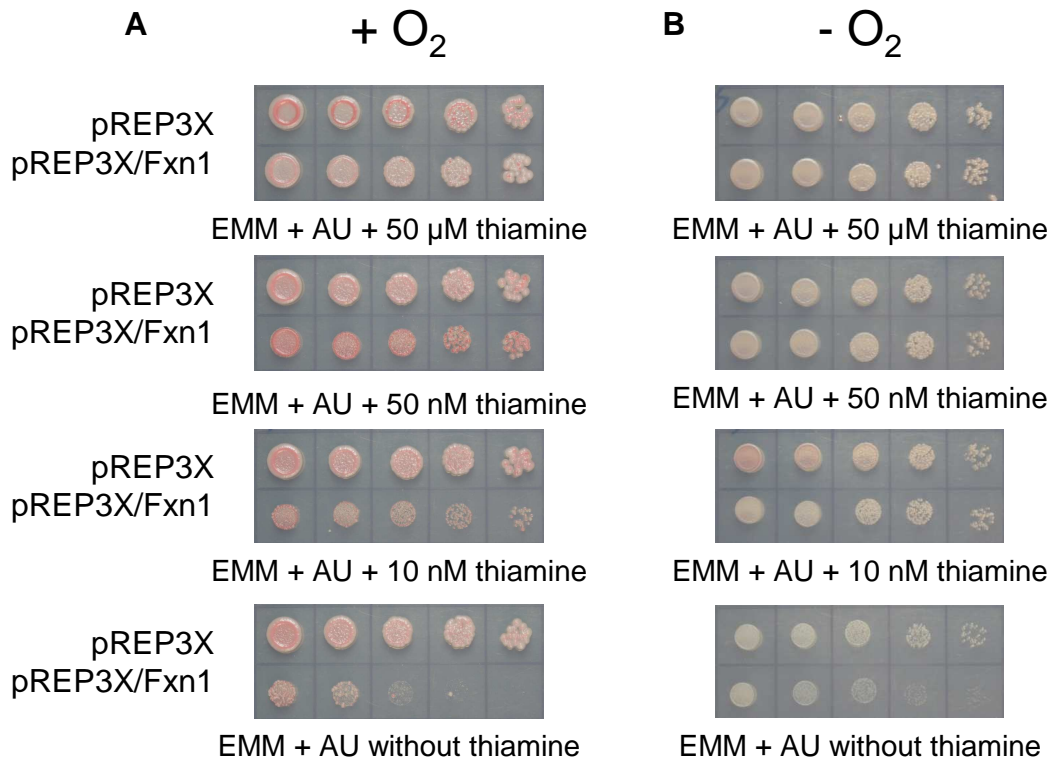


Figure 2.9. Increased amount of the red BPS–Fe²⁺ complex on cells surface indicates the increased Frp1 activity and thus up-regulated iron importing pathway. pREP3X and pREP3X/Fxn1 transformants were grown to mid-log phase in EMM+AU without thiamine then resuspended to 1×10^7 cells/mL. Cells were serial diluted (1:5) and 3 μ L was spotted on EMM+AU and 25 μ M BPS with 0 nM, 10 nM, 50 nM and 50 μ M thiamine, as indicated. Plates were incubated at 30 °C for 5 days aerobically (A) or anaerobically (B).

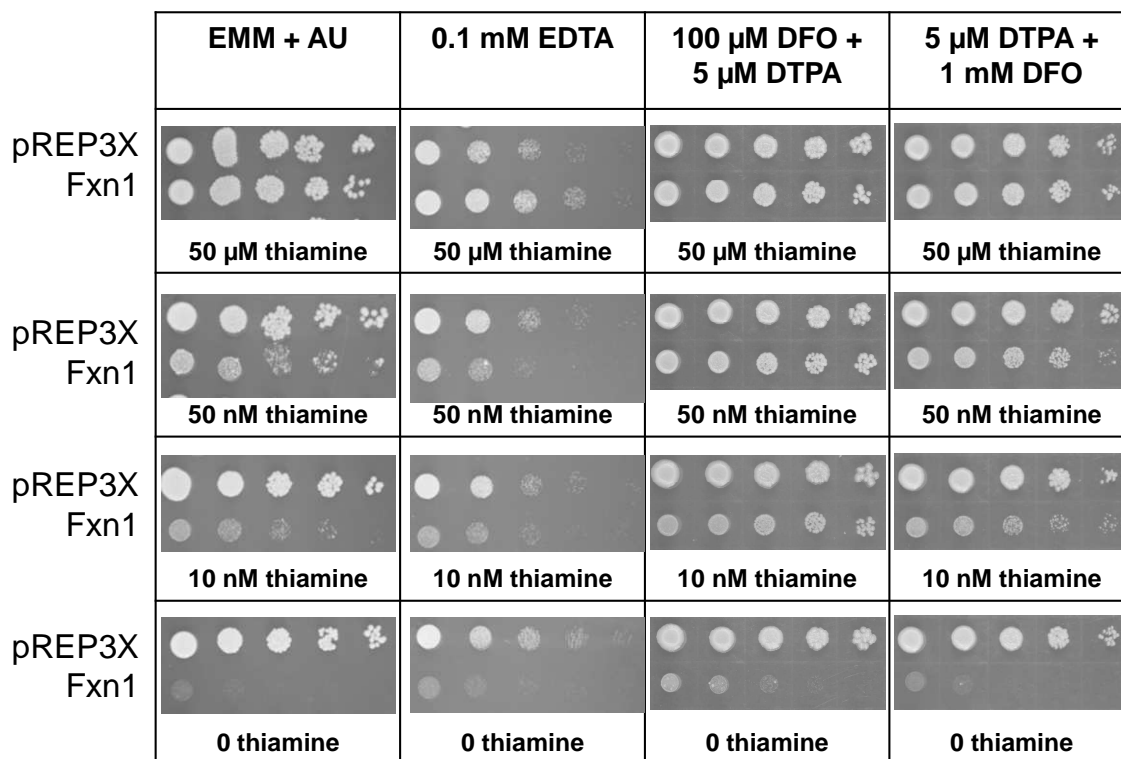


Figure 2.10. The resistance of Fxn1 overexpression transformants to specific and non-specific iron chelators. pREP3X and pREP3X/Fxn1 transformants were grown to mid-log phase in EMM+AU without thiamine then resuspended to 1×10^7 cells/mL. Cells were serial diluted (1:5) and 3 μ L was spotted on EMM+AU with 0 nM, 10 nM, 50 nM and 50 μ M thiamine, with the addition of 0.1 mM EDTA, 100 μ M DFO and 5 μ M DTPA, or 1 mM DFO and 5 μ M DTPA. Plates were incubated aerobically at 30 $^{\circ}$ C for 5 days.

iron or the iron-deplete conditions is inhibiting high-affinity iron uptake via Frp1, which would render cells more resistant to metal chelation.

2.3.4 Activities of Mitochondrial Fe/S Enzymes Increase Upon Mitochondrial Fxn1 Overexpression

Fe/S cluster biogenesis, which primarily occurs in mitochondria, provides essential Fe/S clusters for many mitochondrial proteins and enzymes critical for cell viability (26) and intact Fe/S clusters are functionally required for respiratory cell growth (44). Fe/S cluster synthesis is linked to the regulation of iron homeostasis (19), and frataxin deficiency in model systems causes decreased Fe/S proteins activities due to the loss of catalytic Fe/S clusters (47). Since Fxn1 overexpression cells accumulate both cellular and mitochondrial iron, the Fe/S cluster synthesis machinery could be affected so as Fe/S proteins activities. In addition, the accumulated iron could undergo Fenton chemistry to produce severe oxidative stress, which can also inhibit the activities of Fe/S cluster enzymes. Thus, the activities of two mitochondrial Fe/S enzymes, aconitase and succinate dehydrogenase (SDH), were examined in Fxn1 overexpression cells. These two enzymes are sensitive markers of Fe/S cluster levels and oxidative stress. Aconitase is a mitochondrial TCA cycle enzyme whose activity relies on an intact [4Fe-4S] cluster (103). The Fe/S cluster in aconitase is exposed to solvent and can be modified into [3Fe-4S] cluster by hydroxyl radicals, which makes the activity of mitochondrial aconitase sensitive to oxidative stress. SDH, also known as complex II, is a mitochondrial membrane enzyme that contains three Fe/S clusters and links the TCA cycle to the electron transport chain (104). Compared to aconitase, the activity of SDH is not as severely affected by oxidative stress (45).

In spite of the inhibited *S. pombe* cell growth with increasing Fxn1 concentrations, the activity of mitochondrial aconitase actually increases with Fxn1 overexpression levels, especially

for the cells cultured in 10 nM thiamine (**Figure 2.11A**). Cells overexpressing Fxn1 have also increased SDH activities compared to the control strain at all thiamine levels, but the increase in activity is weakly abrogated at high levels of Fxn1 (**Figure 2.11B**). To test if these increased enzyme activities are due to the transcriptional up-regulation of mitochondrial aconitase or SDH genes (*acon1* and *sdh2*, respectively), quantitative real-time reverse transcriptase PCR (qRT-PCR) was performed with cDNA isolated from Fxn1 transformants cultured in 50 μ M, 50 nM and 10 nM thiamine. The mRNA transcripts for both *acon1* and *sdh2* slightly decrease as Fxn1 expression increases (**Table 2.3**); therefore, the up-regulated aconitase and SDH activities occur at the protein level, most likely due to occupancy of catalytic Fe/S clusters (105).

It is possible that genes encoding proteins of the Fe/S cluster biosynthetic complex are up-regulated to account for the increased iron concentration in Fxn1 overexpressing cells, and the transcription levels of other three components of Fe/S cluster assembly machinery, the cysteine desulfurase Nfs1 that supplies sulfide, the Fe/S cluster scaffold protein Isu1 on which clusters are assembled, and the accessory protein Isd11 with unknown function were determined by qRT-PCR in Fxn1 overexpression cells (**Table 2.3**). No changes in transcript level were observed for Nfs1, while both Isu1 and Isd11 transcript levels increase in relation to Fxn1 levels in mitochondria. This suggests that Fxn1 possibly increases the expression of Fe/S cluster biosynthetic complex proteins, which could lead to a higher iron demand in mitochondria.

2.3.5 Fxn1 Overexpression Cells Have Increased Oxidative Stress

Frataxin deficiency has been linked to oxidative stress, whereas most frataxin overexpression studies demonstrated increased resistance to oxidative stress (82-84, 87, 88, 106). To determine if the Fxn1 mitochondrial overexpression in *S. pombe* produces similar results, a growth assay was performed in the presence of 0.5 mM hydrogen peroxide (107). Hydrogen

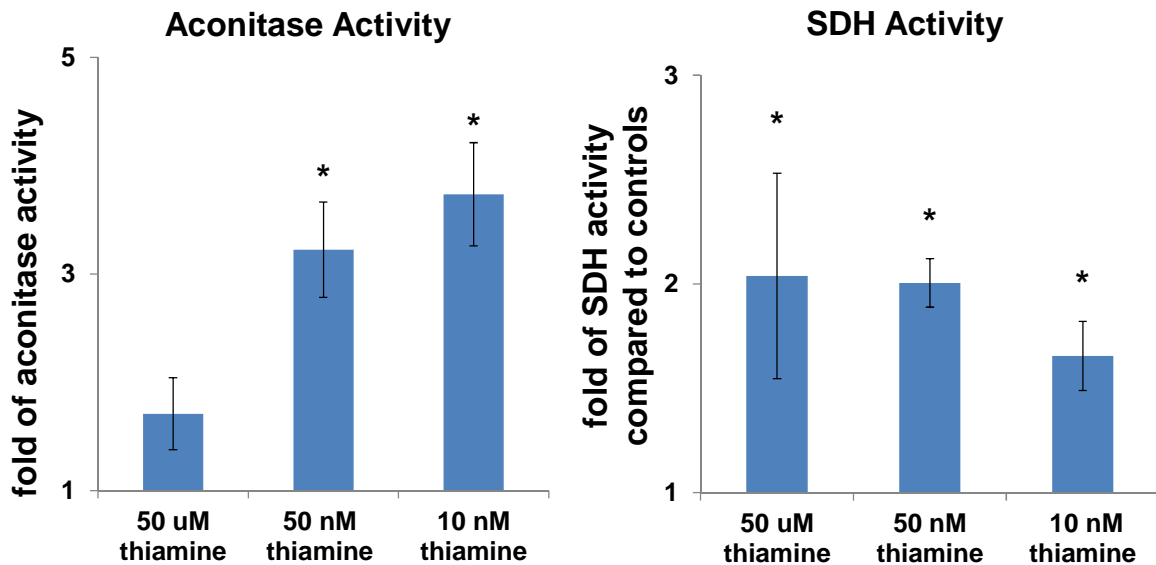


Figure 2.11. Aconitase and SDH activities increase at protein levels as Fxn1 overexpressed

in mitochondria. (A) The aconitase activity was measured with purified mitochondria of pREP3X and pREP3X/Fxn1 transformants cultured in EMM+AU with the indicated amount of thiamine. Results are normalized to the total protein amount loaded to each reaction, and compared with control pREP3X transformant cultured under the same condition ($n > 5$, error bars are shown as S.E.M., asterisks indicate p -value < 0.05). Aconitase activity increased corresponding to the level of Fxn1 overexpression. (B) Succinate dehydrogenase activity was measured for isolated mitochondria of pREP3X and pREP3X/Fxn1 transformants cultured in EMM+AU with indicated amount of thiamine. Results are normalized to the total protein amount loaded to each reaction, and compared with control pREP3X transformant cultured under the same condition ($n > 5$, error bars are shown as S.E.M., asterisks indicate p -value < 0.05). Succinate dehydrogenase activity increased when Fxn1 is overexpressed in mitochondria.

Table 2.3. The relative transcript levels of interested genes, normalized to *act1* as the housekeeping gene.

	50 μ M thiamine		50 nM thiamine		10 nM thiamine	
	pREP3X	pREP3X/ <i>Fxn1</i>	pREP3X	pREP3X/ <i>Fxn1</i>	pREP3X	pREP3X/ <i>Fxn1</i>
<i>fxn1</i>	1.00 \pm 0.06	15.50 \pm 0.26	1.01 \pm 0.07	43.00 \pm 8.50	1.00 \pm 0.05	386.90 \pm 71.90
<i>acon1</i>	1.00 \pm 0.06	0.78 \pm 0.05	1.00 \pm 0.05	0.95 \pm 0.10	1.02 \pm 0.13	0.81 \pm 0.05
<i>sdh1</i>	1.00 \pm 0.04	0.96 \pm 0.11	1.01 \pm 0.09	1.29 \pm 0.05	1.00 \pm 0.01	0.72 \pm 0.07
<i>sdh2</i>	1.00 \pm 0.05	0.82 \pm 0.03	1.01 \pm 0.12	0.94 \pm 0.05	1.00 \pm 0.03	0.62 \pm 0.01
<i>isu1</i>	1.00 \pm 0.06	1.52 \pm 0.29	1.01 \pm 0.07	1.34 \pm 0.19	1.00 \pm 0.02	1.86 \pm 0.46
<i>nfs1</i>	1.01 \pm 0.09	1.20 \pm 0.15	1.05 \pm 0.23	0.97 \pm 0.19	1.00 \pm 0.03	1.04 \pm 0.01
<i>isd11</i>	1.01 \pm 0.10	1.32 \pm 0.08	1.03 \pm 0.18	1.27 \pm 0.22	1.01 \pm 0.12	0.92 \pm 0.04
<i>sod1</i>	1.00 \pm 0.05	1.76 \pm 0.04	1.03 \pm 0.17	1.70 \pm 0.11	1.00 \pm 0.04	1.08 \pm 0.20
<i>sod2</i>	1.00 \pm 0.07	1.33 \pm 0.02	1.01 \pm 0.10	0.84 \pm 0.02	1.00 \pm 0.06	0.95 \pm 0.15

peroxide inhibits the growth of the control cells, but the growth of cells with lower levels of Fxn1 (*i.e.*, 50 μ M thiamine) is not as affected (**Figure 2.12**). This indicates that a slight increase in Fxn1 concentrations leads to increased resistance to peroxide oxidative stress.

It is possible that the activities of antioxidant enzymes such as superoxide dismutase and catalase are up-regulated as an adaptive response during culturing in the different thiamine concentrations to counter the oxidative stress burden in Fxn1 overexpression cells. The transcriptional levels and activities of superoxide dismutase (SOD1/SOD2) were measured for Fxn1 expressing strains at various thiamine concentrations. Both the *sod1* transcript and total enzyme activity increase for all levels of Fxn1 overexpression compared to control cells, but the magnitude does not appear to be correlated to the amount of mitochondrial Fxn1 (**Figure 2.13A** and **Table 2.3**). In addition, total catalase activity also increases for all Fxn1 overexpressing cells but with no correlation to Fxn1 expression levels (**Figure 2.13B**). These observations suggest that cells with increased concentrations of Fxn1 have an endogenously elevated oxidative stress response, consistent with the presence of mitochondrial dysfunction and oxidative stress. In an attempt to rescue the growth defect by counteracting the oxidative stress, the growth assay media was supplemented with various anti-oxidants but no rescue is observed (data not shown). Thus, it is likely that the oxidative stress observed for Fxn1 overexpressing cells is the byproduct of other cellular changes such as iron accumulation.

2.3.6 Fxn1 Interactions with Other Mitochondrial Proteins

To confirm that Fxn1 directly participates in the Fe/S cluster biogenesis pathway and to identify other iron-related pathway(s) in which Fxn1 is involved, photo-activated chemical crosslinking to trap protein–protein interactions was performed with human frataxin (hFxn) and

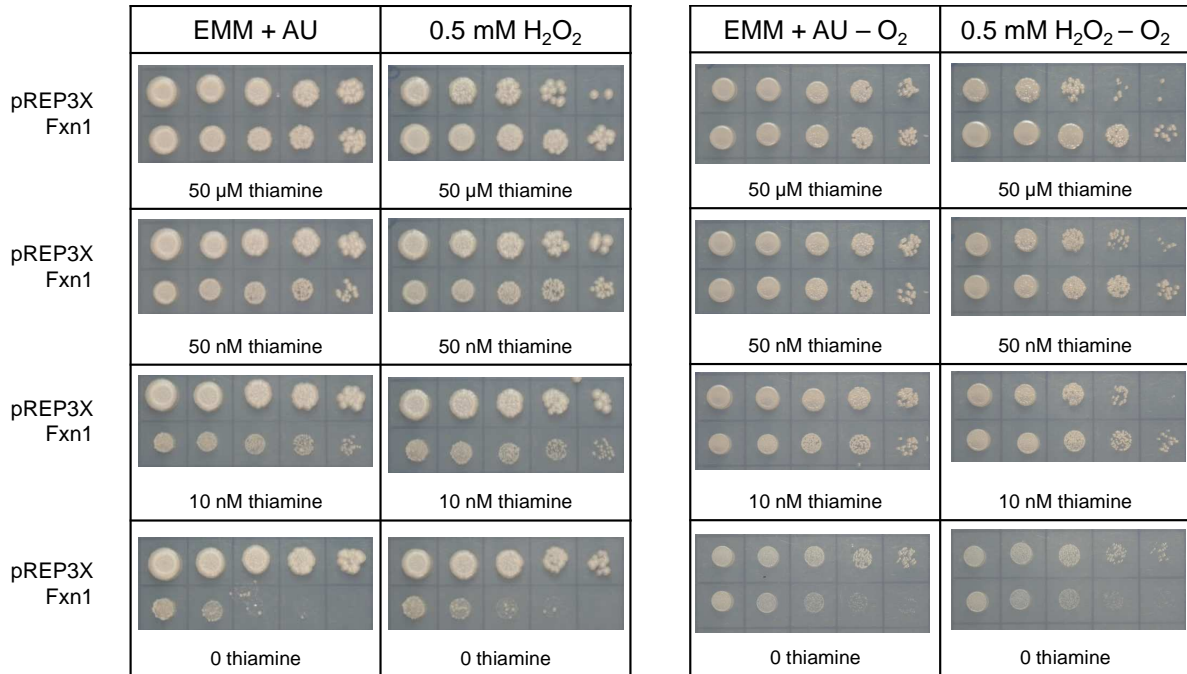


Figure 2.12. The low level overexpression of Fxn1 in mitochondrial elevates the cellular resistance to H₂O₂. pREP3X and pREP3X/Fxn1 transformants were grown to mid-log phase in EMM+AU without thiamine then resuspended to 1×10^7 cells/mL. Cells were serial diluted (1:5) and 3 μ L was spotted on EMM+AU with 0 nM, 10 nM, 50 nM and 50 μ M thiamine, with the addition of 0.5 mM H₂O₂. Plates were incubated at 30 °C for 5 days aerobically or anaerobically as indicated.

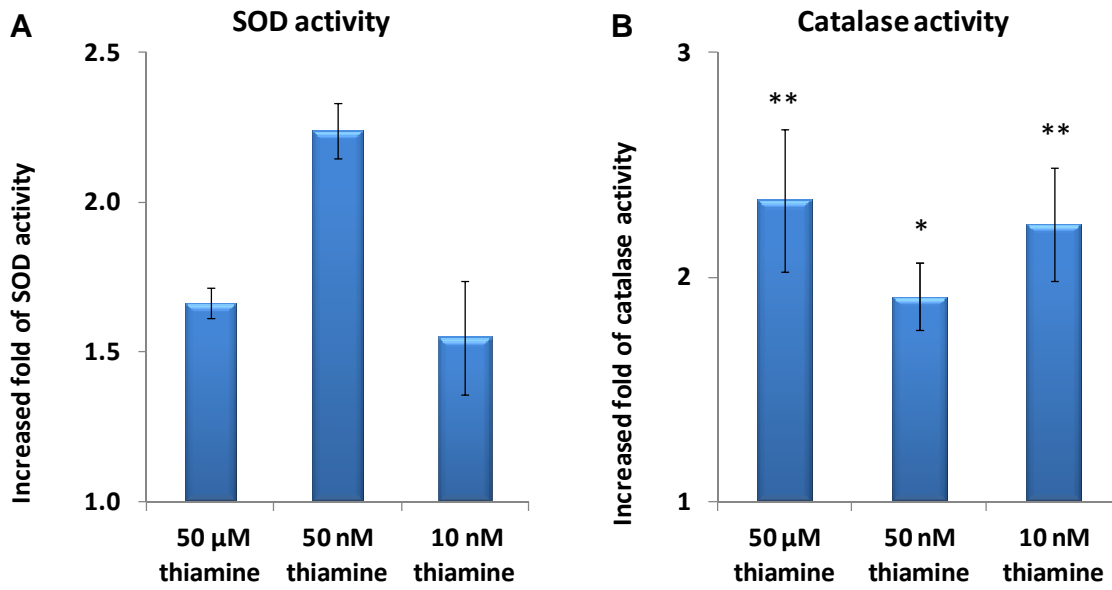


Figure 2.13. Increased SODs and catalase activity were observed for cells overexpress

Fxn1. (A) SOD activity was measured with 5 μ g of cell lysate from pREP3X and pREP3X/Fxn1 transformants cultured in 50 μ M, 50 nM or 10 nM thiamine. The absorbance changes at 450 nm in 10 min were normalized to the total protein amount loaded to each reaction, and values were presented as fold-increase of control cells. (B) The catalase activity was measured with 2 μ g of cell lysate from pREP3X and pREP3X/Fxn1 transformants cultured in 50 μ M, 50 nM or 10 nM thiamine. The absorbance changes at 540 nm were normalized to the total protein amount loaded to each reaction, and values were presented as fold-increase of control cells ($n \geq 4$, error bars are shown as S.E.M., *, p -value < 0.05, **, p -value < 0.01).

its known partner hIsu along with *S. pombe* Fxn1 and mitochondrial protein extract. The trifunctional crosslinker sulfosuccinimidyl-2-[6-(biotinamido)-2-(*p*-azidobenzamido)-hexanoamido] ethyl-1,3'-dithiopropionate (sulfo-SBED) was chosen. Sulfo-SBED contains an *N*-hydroxysuccinimide ester group that covalently modifies lysine amides from hFxn and Fxn1 “bait” proteins, a photoreactive phenyl azide that covalently attaches to the prey protein via C–H bond insertion under UV light, and a biotin group to aid detection and isolation of the prey protein (**Figure 2.14**). Sulfo-SBED also contains a disulfide bond in the linker that can be cleaved with reducing agent to transfer the biotin label from the bait to the prey protein. Photo-reactive chemical crosslinking traps interacting proteins with covalent bonds and provides a great approach to find direct interacting partners of interested proteins, especially when it is coupled with tandem mass spectrometry and computationally aided protein identification such as PeaksClient (108).

To test the specificity of sulfo-SBED crosslinking reaction, hFxn was labeled and mixed with human Fe/S cluster scaffold protein hIsu (or BSA as a control) before UV activation at 365 nm. The reaction products were analyzed with SDS-PAGE and Western-blotting to detect biotinylated proteins. As shown in **Figure 2.15**, SBED-hFxn by itself formed a small amount of oligomers (lane 2), and the biotin label was completely removed with the addition of reducing agent β -ME, as expected (lane 3). When incubated with hIsu and iron, a complex with a molecular weight of about 28 kDa was observed after UV crosslinking (lane 5), and this complex was disassembled with β -ME reduction of the linker disulfide bond (lane 6). Because hIsu has a molecular weight of ~14 kDa which is similar to hFxn, a control reaction with only SBED-hFxn was exposed to UV light (lane 7). The band at 28 kDa that was due to SBED-hFxn dimerization is not as intense as in the hFxn–hIsu reaction (compared to lane 5), and this dimerization was

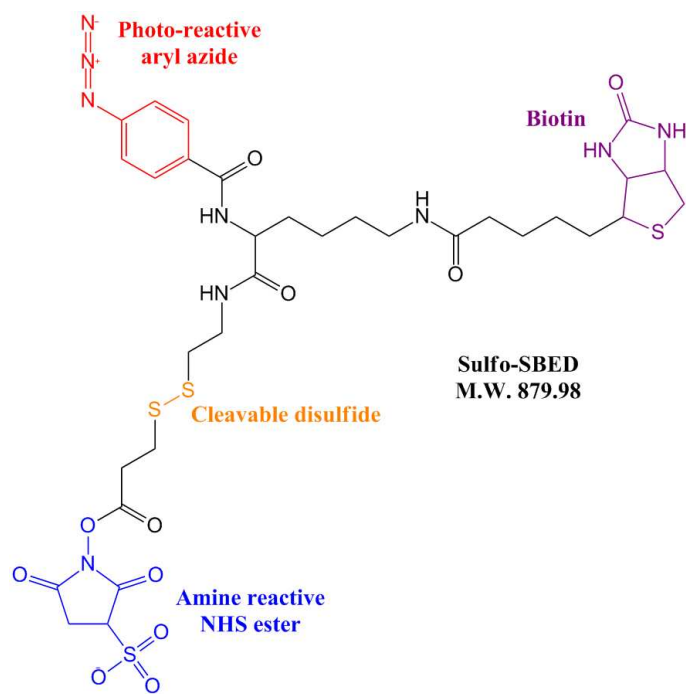


Figure 2.14. Structure of Sulfo-SBED.

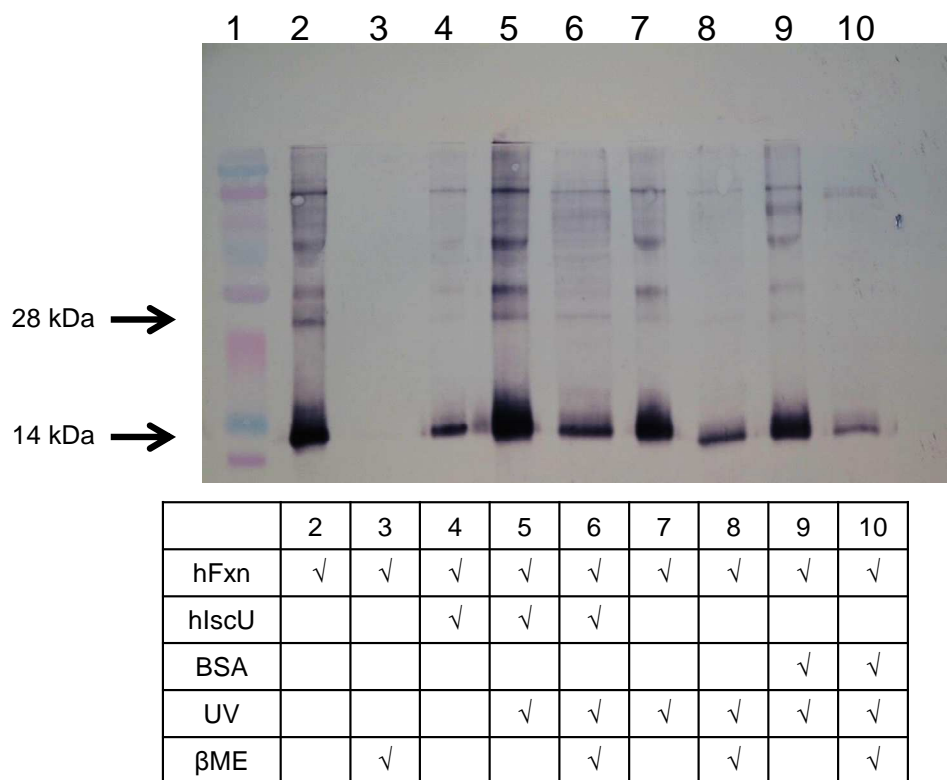


Figure 2.15. The control reactions of photo-activated chemical crosslinking. Western blot of crosslinking reactions with SBED-hFxn and IscU, or SBED-hFxn and BSA was performed with UV activation at 365 nm (as indicated). Samples were analyzed by SDS-PAGE and electrophoretic transfer to a PVDF membrane. Streptavidin-alkaline phosphatase was used for detection of biotin tag. Lane 1: protein molecular ladder; Lane 2: 1 μ M SBED-hFxn; Lane 3: 1 μ M SBED-hFxn reduced by 5 mM β ME; Lane 4: 1 μ M SBED-hFxn mixed with 2 μ M IscU; Lane 5: 1 μ M SBED-hFxn mixed with 2 μ M IscU and UV-activated; Lane 6: 1 μ M SBED-hFxn mixed with 2 μ M IscU and UV-activated then reduced with 5 mM β ME; Lane 7: 1 μ M SBED-hFxn UV-activated; Lane 8: 1 μ M SBED-hFxn UV-activated and reduced with 5 mM β ME; Lane 9: 1 μ M SBED-hFxn mixed with 2 μ M BSA and UV-activated; Lane 10: 1 μ M SBED-hFxn mixed with 2 μ M BSA and UV-activated then reduced with 5 mM β ME.

disassembled with β -ME (lane 8). In addition, SBED-hFxn was incubated with BSA, which is not expected to interact with hFxn, so that non-specific covalent crosslinking can be evaluated. This complex was exposed to UV light, but no band with correct molecular weight for the ~80 kDa for hFxn-BSA complex (lane 9) or ~66 kDa for biotin-BSA after label transfer (lane 10) is observed.

In wild-type *S. pombe* cells, there are about an estimated 3132 molecules of Fxn1 per cell (<http://www.pombase.org/spombe/result/SPCC1183.03c>), thus in the model of Fxn1 overexpression, the w/w ratio of Fxn1 to whole cell lysate is about 1:770. With the consideration of crosslinking efficiency, sulfo-SBED labeled Fxn1 was incubated with mitochondrial extracts or cell lysate with 1:70 w/w ratio and subjected to UV light to detect the interacting partners of *S. pombe* Fxn1 using the scheme outlined in **Figure 2.16**. As shown in **Figure 2.17** lane 2, Fxn1 is labeled with sulfo-SBED, however, the quality of the blot was not ideal. The SBED label was removed with β -ME reduction of the linker disulfide (lane 3). After UV activation, no Fxn1 intramolecular crosslinks are observed (lane 4), which is confirmed after label transfer (lane 5). When Fxn1 was incubated with *S. pombe* cell lysate, multiple faint biotinylated protein bands of molecular weights larger than Fxn1 were observed (lane 6) and biotin label transfer was confirmed (lane 7). The most intriguing observation is when Fxn1 was incubated with *S. pombe* mitochondrial extracts, intense bands at ~20 kDa, ~39 kDa, and 52–80 kDa indicate that Fxn1 physically interacts with multiple proteins. These interacting proteins were purified by streptavidin-agarose resin and subjected to immobilized trypsin digestion and proteomic identification with mass spectrometry. However, the identities of these proteins are still under investigation.

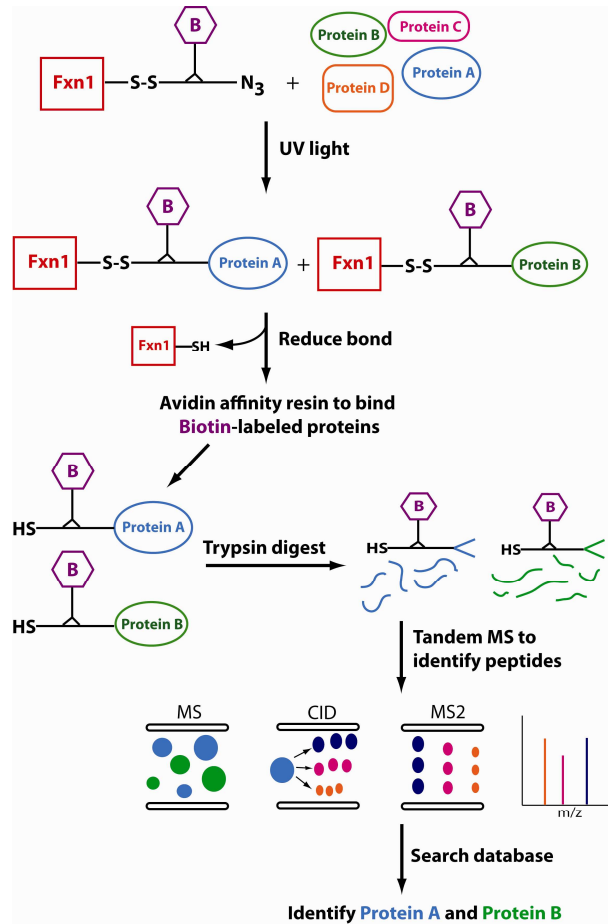


Figure 2.16. Photo-activated chemical crosslinking to identify proteins that interact with *S. pombe* Fxn1. Fxn1 is labeled with sulfo-SBED (bait) then mixed with *S. pombe* mitochondrial extract (prey). Upon UV activation, proteins that form complexes with Fxn1 will become covalently bound. The disulfide bond in the linker is reduced, which releases Fxn1 and transfers the biotin label (purple) to the interacting protein. Biotinylated proteins can be captured by avidin affinity chromatography then digested with trypsin. The digests are subjected to tandem MS/MS spectrometry and the proteins are identified using Peaks and Xlink software.

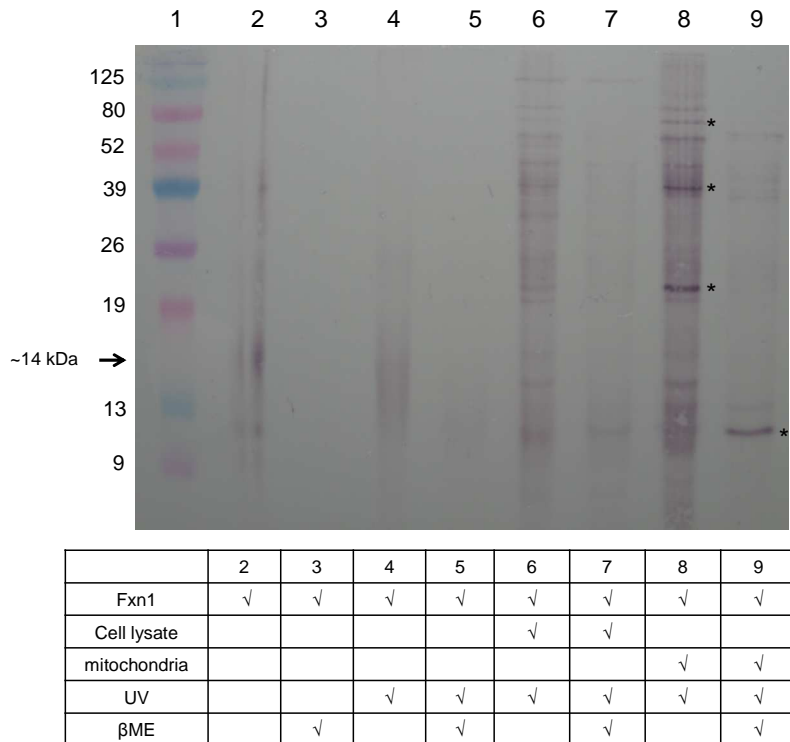


Figure 2.17. Photo-activated chemical crosslinking Fxn1 and *S. pombe* extracts. SBED-labeled *S. pombe* Fxn1 was mixed with either cell lysate or mitochondrial extract. Crosslinking reactions were performed and the biotin tag was detected with the streptavidin-alkaline phosphatase as described. The asterisks indicate the Fxn1–protein complexes with molecular weight about 21 kDa, 39 kDa, and 80 kDa. Lane 1: protein molecular ladder; Lane 2: 1 μ M SBED-Fxn1; Lane 3: 1 μ M SBED-Fxn1 reduced with 5 mM β ME; Lane 4: 1 μ M SBED-Fxn1 UV-activated at 365 nm; Lane 5: 1 μ M SBED-Fxn1 UV-activated at 365 nm reduced with 5 mM β ME; Lane 6: 1 μ M SBED-Fxn1 mixed with 1 g wild type *S. pombe* cell lysate and UV-activated at 365 nm; Lane 7: 1 μ M SBED-Fxn1 mixed with 1 g wild type *S. pombe* cell lysate and UV-activated at 365 nm reduced with 5 mM β ME; Lane 8: 1 μ M SBED-Fxn1 mixed with 1 g wild type *S. pombe* mitochondria and UV-activated at 365 nm; Lane 9: 1 μ M SBED-Fxn1 mixed with 1 g wild type *S. pombe* mitochondria and UV-activated at 365 nm reduced with 5 mM β ME.

2.4 Discussion

2.4.1 The *in vivo* Function of Fxn1 in *S. pombe*

The disease Friedreich's ataxia (FRDA) is caused by the decreased expression of the mitochondrial protein frataxin, which is highly conserved in most organisms and is linked to cellular iron homeostasis (54). Understanding the precise biological functions of frataxin is critical for development of effective treatments for FRDA. Numerous FRDA model systems have been created; however, the functional role of frataxin is still inconclusive (85). This is partially due to the complexity of the phenotypes. How does one distinguish the direct consequence of frataxin deficiency from the secondary ones that are caused by the disruption of the delicately controlled iron homeostasis and mitochondrial functions?

One possible method is to overexpress frataxin in a well-studied model system and characterize the phenotypic changes. The results from frataxin deficiency can then be compared to frataxin overexpression. Overexpression of frataxin has been studied in several organisms, including budding yeast, mice, flies, and human cell lines; however, some of the results are contradictory (17, 73, 83-88, 106). Here we present a study using the fission yeast *S. pombe* model system to study the *in vivo* effects of frataxin overexpression, providing a complementary way to look at the possible functions of frataxin.

Three different levels of exogenous Fxn1 were generated through a thiamine repressible promoter and the cellular responses compared: high (~387-fold), moderate (~43-fold) and low (~15-fold). A significant growth deficiency under aerobic conditions was observed for moderate and high levels of Fxn1, but not when the mitochondrial localization sequence was disrupted (Fxn1 Δ 2-11). This demonstrates that the growth defect is related to the increased mitochondrial

Fxn1 levels, but similar growth inhibition is not observed for other proteins overexpressed in mitochondria (109, 110).

Similar to the overexpression of frataxin in *S. cerevisiae* (85), at high levels of frataxin overexpression in *S. pombe* caused the formation of unprocessed isoform and aggregation. The hypothesis raised by Vaubel and Isaya (62) that the larger isoform can form oligomers while the smaller isoforms tends to exist as monomers provides a great explanation for our observations with *S. pombe* Fxn1. Although the highest level of Fxn1 expression is beyond the normal scale of *in vivo* protein concentrations, we could not exclude the possibility that the ratio of the two isoforms changes in response to the environmental changes. It is also possible that when such a high level of Fxn1 is expressed in mitochondria, the enzymes involved in Fxn1 maturation (*i.e.*, proteolytic processing) are overwhelmed, thus the larger isoform is observed. It is known that the N-terminus of frataxin is involved in protein oligomerization in humans and in yeast (62), so the observed *S. pombe* Fxn1 oligomers are likely the consequence of the unprocessed Fxn1. The degree of growth defect may be related to the amount of the full-length Fxn1 or the amount of oligomerization which essentially reduces the level of biologically functional Fxn1, but a more detailed examination is required, such as analytical size exclusion chromatograph.

Along with the severe growth inhibition, Fxn1 overexpressing cells exhibited significantly decreased cellular respiration (~20% of control respiration). A typical hallmark of respiratory deficiency is the generation of reactive oxygen species (ROS) from incomplete reduction of molecular oxygen by the electron transport chain (111). Fxn1 overexpressing cells at all levels exhibited an increased activity of the radical scavenger enzyme SOD, which indicates an increased endogenous superoxide anion formation and oxidative stress (112). The mRNA for mitochondrial SOD also increased with Fxn1 levels, indicating the cells respond to

oxidative stress both at the cellular level and mitochondrial level. This induced cellular response explains why low Fxn1 overexpression led to resistance to exogenous H₂O₂. In addition, activity assays indicate that catalase activity, an enzyme that combats hydrogen peroxide stress, is up-regulated at all levels of Fxn1 expression. In many cases oxidative stress is a general byproduct of mitochondrial dysfunction, so further investigation is warranted in order to determine the specific cause. One potential mechanism is via deleterious redox chemistry of iron.

It is clear that Fxn1 overexpression also leads to impaired iron homeostasis, as evidenced by the up-regulated Frp1 ferriredutase activity (*i.e.*, high affinity iron import) and the 10-fold increase in total cellular iron at the highest level of Fxn1 expression. These observations are most likely the result of up-regulated iron import by the transcriptional regulator Fep1 (24). Iron-deplete media and the addition of a membrane-permeable iron chelators do lessen the growth inhibition of Fxn1 overexpressing cells; thus, the iron accumulation is directly related to cellular dysfunction, most likely through Fenton-based chemistry with Fe³⁺ to produce ROS (9). Based on these results, Fxn1 overexpression at moderate and high levels disrupts the regulation of iron homeostasis, which leads to iron accumulation and oxidative stress. However, frataxin deficiency also results in iron accumulation and oxidative stress, a hallmark of FRDA (45).

Mitochondrial overexpression of *S. pombe* Fxn1 increased the activities of Fe/S cluster containing enzymes, despite of the severe cellular growth defect, iron accumulation, and oxidative stress. This finding is especially interesting because the [4Fe-4S] cluster of aconitase, for example, is known to be very sensitive to oxidative damage (113) and all signs indicate that cells with high levels of Fxn1 experience oxidative stress. Under these conditions, one would expect aconitase activity to decrease. Our results, however, are fully consistent with those for overexpression of human frataxin in mice and in human cancer cells (83, 88). There are two

hypotheses to explain this curious observation. First is that frataxin physically interacts with aconitase to protect the catalytic Fe/S cluster under oxidative stress conditions or repair the damaged [3Fe-4S] cluster as an iron chaperone (79, 80). The other possibility is that increased Fxn1 levels stimulate Fe/S synthesis independent of the iron concentration. This is proposed because low levels of Fxn1 overexpression led to increased Fe/S cluster enzymes activities, but with only slightly increased iron concentrations.

Based on these findings, we hypothesize that one of the major functions for Fxn1 is to stimulate the efficiency of Fe/S cluster assembly machinery (38, 114). (1) With weak overexpression of Fxn1, the efficiency of Fe/S cluster biogenesis is increased, which leads to increased activities of Fe/S cluster enzymes as well as slightly up-regulated iron uptake. The increased cellular iron could cause increased oxidative stress through Fenton chemistry, thus, the oxidative defense system is up-regulated. (2) When moderate levels of Fxn1 are expressed, biologically available iron is consumed by Fe/S cluster biogenesis, which up-regulates the iron import system to bring in more iron to meet mitochondrial demand. (3) At the highest level of overexpressed Fxn1, the phenotype becomes complicated. Additional mitochondrial Fxn1 maintains the production of Fe/S clusters and the turnover of damaged Fe/S clusters in enzymes, but the accumulated iron and the increased oxidative stress overwhelms the mitochondrial functions, which leads to the decreased respiration rate and growth defect. With all the findings above, we suggest that frataxin regulates the efficiency of the Fe/S cluster assembly, and the Fe accumulation as well as oxidative stress is indirect results.

2.4.2 Protein-Protein Interactions with Fxn1

Understanding the proteins that interact with frataxin is very important to clarify the exact function of frataxin. Many proteins are suggested to physically interact with frataxin,

including the preassembled Isu1-Nfs1-Isd11 Fe/S cluster synthesis complex (54), the heme synthesis enzyme ferrochelatase (31), and the TCA cycle enzyme aconitase (79). Some of these interactions could be transient, which means the interaction of frataxin with other proteins cannot always be observed with traditional methods such as co-immunoprecipitation (co-IP) (114). The trifunctional crosslinker sulfo-SBED labels protein of interest and forms covalent bonds with prey proteins through the photo-reactive phenyl azide so that transient protein interactions could be captured and analyzed. As demonstrated in this study, SBED-hFxn formed a crosslinked complex with hIscU and transferred the biotin label after reduction of the disulfide linker. In addition, a crosslinked complex could not be formed with a non-specific protein like BSA. This indicates that this technique detects specific complexes between SBED-frataxin and prey protein(s). We utilized the crosslinker sulfo-SBED in a proteomics approach to detect the potential *S. pombe* protein partners of Fxn1 in mitochondria. The observation of multiple biotin-labeled complexes provides evidence for multiple interaction partners. Future work will be focused on identifying these complexes.

2.5 Future Work

To address the unexplained observations in this dissertation research, further experiments are necessary. (1) To identify the isoform that forms oligomers at high levels of Fxn1 overexpression, Fxn1-6His cultured in 10 nM thiamine can be purified and analyzed by analytical size exclusion chromatography to determine the number of subunits in oligomers, and the collected fractions can be further analyzed with MALDI-ToF to determine the molecular weight of subunits. This will provide information about the type of Fxn1 isoforms. (2) Electron paramagnetic resonance spectroscopy and Mössbauer spectroscopy can be used to characterize the oxidation state and coordination of accumulated iron in *S. pombe* cells and intact *S. pombe*

mitochondria as was described for *S. cerevisiae* by Lindhal and colleagues (115). These experiments will provide much needed information about the nature of the accumulated iron, whether it is bioavailable or contained in ferric complexes like ferrihydrite or ferritin. (3) The co-overexpression of Fxn1 and other Fe/S cluster biogenesis machinery components, including Nfs1, Isu1 and Isd11 will provide more evidence that Fxn1 regulates Fe/S cluster synthesis, *i.e.*, the co-overexpression of Nfs1 and Fxn1 may further inhibit the cellular growth. (4) The sulfo-SBED-Fxn1 and mitochondrial extract crosslinking reactions will be optimized to provide higher quality and larger quantities for MALDI-ToF with post-source decay (PSD), which will help to identify the interaction partners of Fxn1 *in vivo*. The tandem MS/MS will be also utilized to identify peptides finger prints.

2.6 Biological Implications

Understanding the functions of frataxin is important to treat and relieve symptoms of FRDA and elevate the life quality of FRDA patients. Current treatments of FRDA include iron chelators and antioxidants, although the effectiveness is not guaranteed and the treatments only slightly extend life expectancy (116). The possibility that frataxin regulates Fe/S cluster assembly has been demonstrated through many *in vitro* experiments and some frataxin knockdown *in vivo* experiments (38). Our result is the first direct evidence that systemically demonstrates that higher levels of mitochondrial frataxin lead to the notable increase in Fe/S enzyme activities (45, 66). While the treatment using iron chelators and antioxidants may be effective in some cases, as they only relieve the consequences of Fe/S enzyme deficiency caused by frataxin depletion, but do not treat the underlying cause of the disease. Future treatment development could focus on the gene therapy and methods to increase the Fe/S cluster biogenesis.

CHAPTER 3

CADMIUM, BREAST CANCER AND HUMAN ESTROGEN RECEPTOR ALPHA

Cadmium is a naturally existing element with electron configuration of $[\text{Kr}] 4d^{10}5s^2$. As such, it shares some characteristics with other group 12 metals such as zinc and mercury, while being unique in many other aspects. Cd^{2+} is the only stable existing Cd ion, because of the filled, stable $4d$ -shell orbitals. Cadmium is not an essential metal, and its presence in organisms generally causes cellular damage. For this reason, Cd^{2+} is classified as a non-native, toxic metal ion. This dissertation chapter will briefly introduce the toxic effects of Cd^{2+} and its relationship to the development of human breast cancer through the function of human estrogen receptor alpha (hER α).

3.1 The Bioinorganic and Biochemical Characteristics of Cadmium

Cd^{2+} is often a Zn^{2+} mimetic in biological systems. The ionic radius of octahedral Cd^{2+} (0.95 Å) is larger than Zn^{2+} (0.88 Å), and it is a soft Lewis acid. Soft metals have large ionic radii, high polarizability, and a preference for coordination by soft Lewis base thiolate groups rather than intermediate/hard bases such as N or O (117). For example, the stability constants ($\log K_{\text{sp}}$) for Cd^{2+} complexes with aspartate (“hard” carboxylate oxygen), histidine (“intermediate” imidazole nitrogen) and cysteine (“soft” thiolate sulfur) are 4.5, 5.4 and 11.0, respectively. This trend clearly demonstrates the preference for softer ligands; however, this is not to say that Cd^{2+} cannot also form complexes with O or N ligands (118).

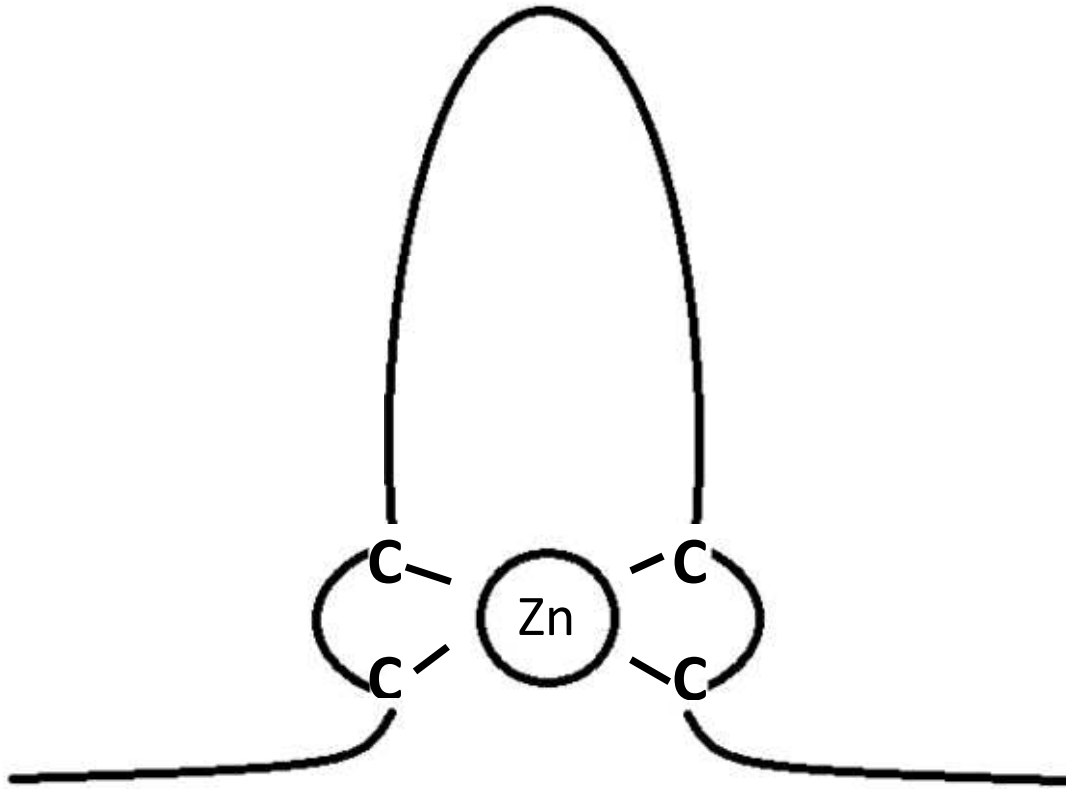
In biological systems, Asp, Glu, Lys, His, and Cys amino acid residues are common ligands for Cd^{2+} with Cys being the most common (118). This coordination preference lays the foundation for cadmium toxicity. Also, essential transition metals have specific homeostasis systems to regulate assimilation and utilization *in vivo*, but Cd^{2+} is not essential, and there is no such regulation. The non-specific uptake of Cd^{2+} ions occurs through several membrane transport channels, including those for Mg^{2+} and Ca^{2+} . Cd^{2+} can also be imported by the non-specific divalent metal transporter NRAMP2, and also by the ZIP Zn^{2+} transporters (7). Imported Cd^{2+} can be coordinated and detoxified by metallothionein (MT), a small cysteine-rich protein with association constants between 10^{14} – 10^{25} M^{-1} (7). MT can coordinate 7 Cd^{2+} ions within 2 binding domains as a part of the detoxification process (119). Glutathione (GSH) is another biomolecule capable of binding and detoxifying Cd^{2+} , but with a lower affinity of 10^9 M^{-1} (120). Thus, “free” solvated Cd^{2+} ions are unlikely in healthy cells.

3.2 Cadmium Toxicity

The major human exposures to cadmium are through the lungs and the gastrointestinal (GI) tract, with different Cd^{2+} absorption rates. Cd^{2+} exposure in lungs is mostly due to inhalation of cigarette smoke, where more than 50% of Cd^{2+} in the lung alveoli can be transferred into the blood (6). The other major exposure pathway is through the GI tract, where the absorption rate is lower and only 5% – 10% of Cd^{2+} in the intestine is transferred into the blood (7). Once Cd^{2+} enters blood, it binds to the proteins albumin and metallothionein, as well as to small antioxidant molecules like glutathione. The metallothionein– Cd^{2+} complex is removed from the blood by the kidneys, but the process is extremely slow, contributing to the 15 year half-life of Cd^{2+} in humans. Chronic exposure to Cd^{2+} is linked to cancers of the prostate, bladder, pancreas, and breast (6). Cd^{2+} is a weak mutagen but a strong co-carcinogen, where it promotes the effects of

other carcinogens. This role of Cd^{2+} has been well described (6), and there are many hypotheses to explain the mechanism(s) of Cd^{2+} carcinogenesis.

The first hypothesis is that Cd^{2+} causes oxidative stress, which leads to DNA damage and propagated mutations (121). GSH and MT, the two molecules responsible for Cd^{2+} detoxification, are highly involved in cellular antioxidant defense. The formation of MT-Cd^{2+} and GSH-Cd^{2+} essentially removes these two molecules from their roles in oxidative defense. The second hypothesis is that Cd^{2+} interferes with DNA repair systems, most likely through the interactions with proteins containing zinc fingers (6). A zinc finger is a protein motif where one zinc ion is tetrahedrally coordinated by four cysteine residues or a combination of cysteine/histidine residues (**Figure 3.1**) (122, 123). Many zinc finger proteins bind DNA as part of their intracellular function. The appropriate zinc finger conformation is critical for DNA binding and, thus, protein function. It is thought that Cd^{2+} can replace Zn^{2+} from the zinc finger motif, disrupt protein conformation, and compromise DNA repair. The dysregulated DNA repair system causes increased DNA mutations that may lead to cancer (6). However, most reports demonstrating that Cd^{2+} can substitute for Zn^{2+} in zinc finger proteins were performed *in vitro*, thus whether the substitution could happen *in vivo* requires further evidence. The last hypothesis is that Cd^{2+} interacts with proteins using non-metal binding sites to disrupt function. For example, Cd^{2+} may bind to and improperly activate human estrogen receptor α (hER α) (124). hER α regulates the transcription of many genes involved in cellular proliferation and pro-apoptosis. Its dysregulation is linked to the development of breast cancers (125), discussed in section 3.3.



4Cys zinc finger

Figure 3.1. The schematic structure of a four Cys zinc finger.

3.3 Xenoestrogens and Human Breast Cancer

Breast cancer, one of the most common cancers in females, is divided into three major groups: ER α positive, HER2 positive, and triple negative (126, 127). About 75% of breast cancers are ER α positive, where cancer cell proliferation is estrogen and estrogen receptor α dependent. HER2 positive cancers comprise 20% to 25% of breast cancer cases and are due to overexpression of the human epidermal growth factor receptor 2 (HER2), which promotes cell proliferation and opposes apoptosis upon the binding of growth factors (126, 127). Triple negative breast cancers (10% – 17% of cancers) lack estrogen and progesterone receptors and do not overexpress HER2 (126, 127).

The development of ER positive breast cancers heavily depends on estrogen and the expression level of estrogen receptors. Lifetime exposure to estrogen leads to a high risk for breast cancer (128). It is known that estrogen-like molecules (*e.g.*, phytoestrogens, xenoestrogens) and estrogen mimetics (*e.g.*, metalloestrogens) can also contribute to the risk of breast cancer, because many of them induce estrogen receptor activity similar to estrogen *in vivo* (124). While phytoestrogens and xenoestrogens resemble the basic structure of estrogen, metalloestrogens are small metal ions and metalloids (124). The metalloestrogens can be divided into two groups, the oxyanions and bivalent cations such as cadmium, lead and nickel (124). Cd²⁺ has been linked to a higher risk of breast cancer in the general population (129-131), but the mechanism has been hard to discern. Because these metalloestrogens exist from water to food, it is important to understand the mechanisms by which these bivalent cations mimic estrogen in the cell.

There is both *in vitro* and *in vivo* evidence that suggests that Cd²⁺ mimics the effects of estrogen through its interaction with hER α , which is the hallmark of ER α positive breast cancers.

For the hER α positive MCF-7 breast cancer cell line, Cd²⁺ mimics the functions of estradiol; it regulates gene transcription (132), gives similar protein expression patterns (128), and stimulates the cell growth. These Cd²⁺-based effects are blocked by antiestrogen. Thus, these observed effects of Cd²⁺ are mediated by hER α . In addition, low levels of Cd²⁺ stimulates the growth of uterine epithelial cells and mammary gland development in ovariectomized rats, which are the classic consequences of increased estrogen levels (128, 133-136). Finally, Cd²⁺ triggers hER α binding to the estrogen response element (ERE) in DNA and stimulates the transcription of the reporter gene luciferase in transfected MCF-7 cells (137). Cd²⁺ is also known to bind hER α directly with nanomolar affinity and block estrogen binding to the ligand binding domain (137). Section 3.4 will describe the structure of hER α in more detail including the ligand binding site and structural consequences of estrogen binding.

3.4 Structure and Functions of hER α

Human estrogen receptor alpha α is encoded by the gene *ESR1* located on locus 6q25.1 (138) and containing 8 exons and 7 introns (139). There are three domains in the processed hER α protein as illustrated in **Figure 3.2**: the N-terminal transactivation domain (AF-1; residues 1–184), the DNA-binding domain (DBD; residues 185–250), and the C-terminal transactivation domain (AF-2; residues 251–595) that contains the ligand binding domain (LBD; residues 311–551) (125).

The AF-1 transactivation domain is involved in protein–protein interactions with the primary transcription machinery to activate transcription of target genes containing the proper response element in the promoter region (140) (125). This domain is solvent exposed with several phosphorylation sites; yet, little is known about its detailed three dimensional structure. In contrast, the structure and function of the DBD is well characterized (125). There are 8 highly

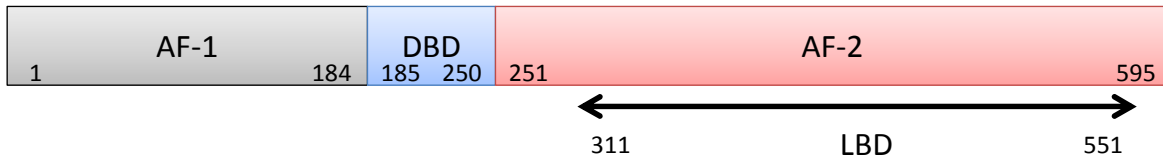


Figure 3.2. The three major domains in hER α . The N-terminal transactivation domain (AF-1; residues 1–184), the DNA-binding domain (DBD; residues 185–250), and the C-terminal transactivation domain (AF-2; residues 251–595) that contains the ligand binding domain (LBD; residues 311–551).

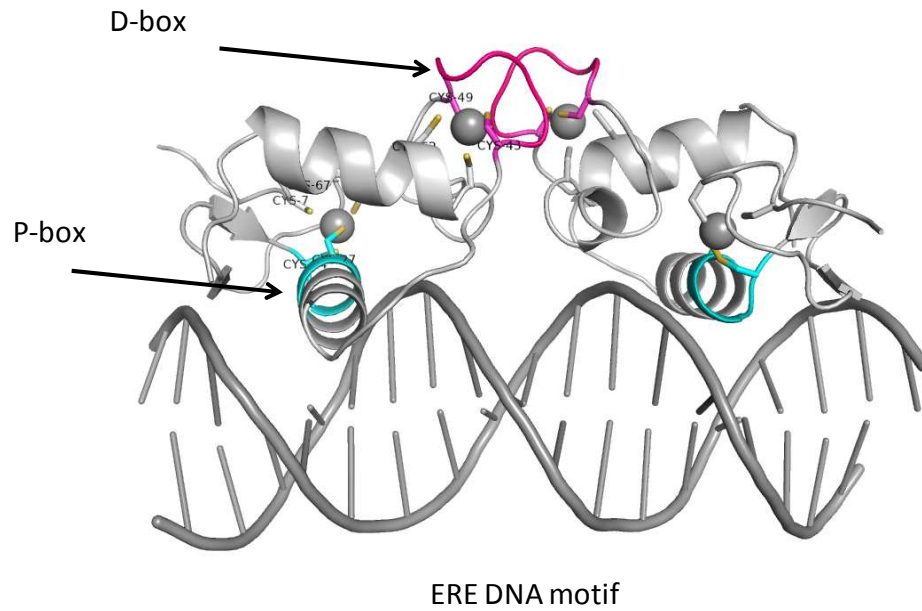


Figure 3.3. The DNA binding domain of hER α . The homodimeric hER α DNA binding domain is bound the estrogen response element DNA is shown. P-box is in cyan, D-box in pink, and Zn²⁺ in grey spheres. (PDB: 1HCQ) (141).

conserved cysteine residues in the DBD that are divided into two groups. Each group coordinates one Zn^{2+} in a tetrahedral geometry as part of a Cys₄ zinc finger motif. The two zinc fingers are different both in structure and function (**Figure 3.3**). The first zinc finger is called the proximal box or P-box finger and is involved in DNA recognition, while the second zinc finger named the distal box or D-box finger is involved in DNA-dependent dimerization of the DNA binding domain (142, 143).

Transactivation domain AF-2 is responsible for ligand recognition, ligand-dependent dimerization, and recruitment of other transcription factors (125). The transcription factor activity of a chimeric protein, which contained the DNA binding domain of yeast transcription activator protein Gal4 fused to the ligand binding domain of hER α (residues 311–553), demonstrated that the LBD alone was capable of estrogen recognition and activation (144). The crystallographic structure shows that the LBD contains 12 α -helices and 2 small β -strands, folded into a three-layered “sandwich” (145). Helices H1–H4 form one layer, helices H5–6, H9 and H10 are the central layer, while helices H7–8 and H11 are arranged as the third layer (**Figure 3.4**). The three layers form the ligand binding cavity. A structural overlay of the hER α LBD bound to estradiol or raloxifene (an anti-estrogen breast cancer therapeutic) reveals that there is little change in the ligand cavity with the exception of helix H12, which is localized at the bottom of ligand cavity (**Figure 3.5**) (145). Upon estrogen binding, helix H12 seals the ligand binding cavity and packs against helices H3, H5–H6, and H11 (125). Helix H12 is considered to be the most critical structural element for ligand-dependent hER α activation and recruitment of co-activator proteins, such as the nuclear receptor co-activator-2 NCoA-2, which further up-regulates the transcription of target genes (146). Besides the proper arrangement of secondary structural elements of the LBD, several amino acid residues are critical for estrogen binding.

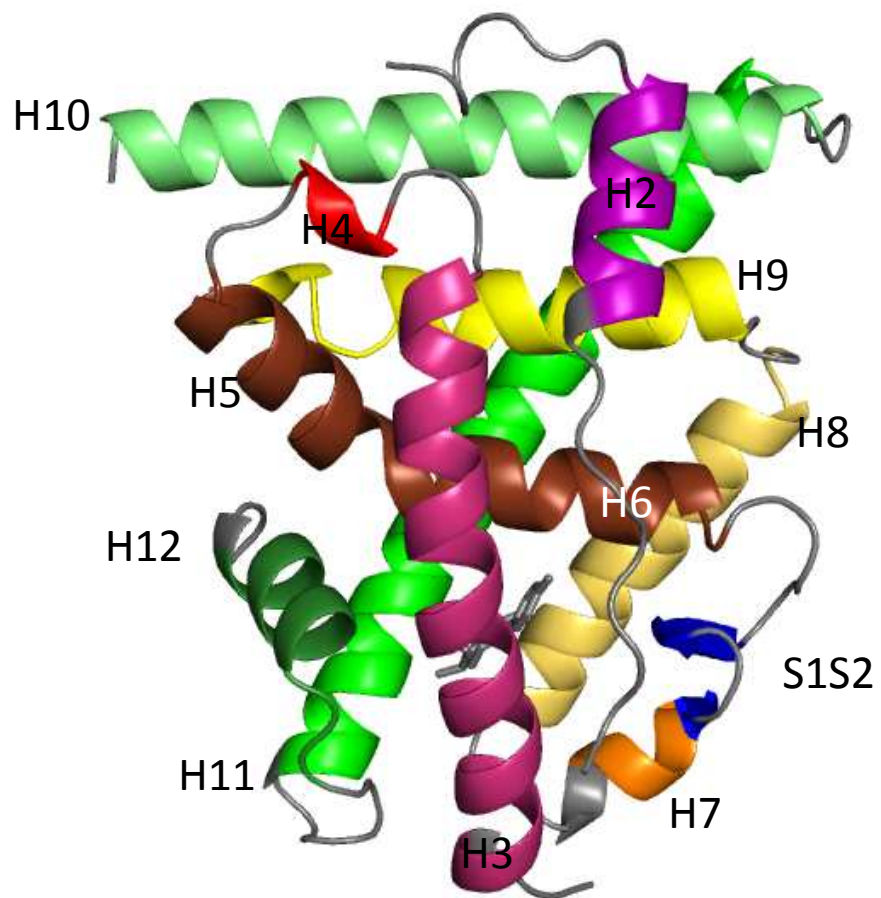


Figure 3.4. The monomeric ligand binding domain of hER α . (PDB: 1ERE) (145).

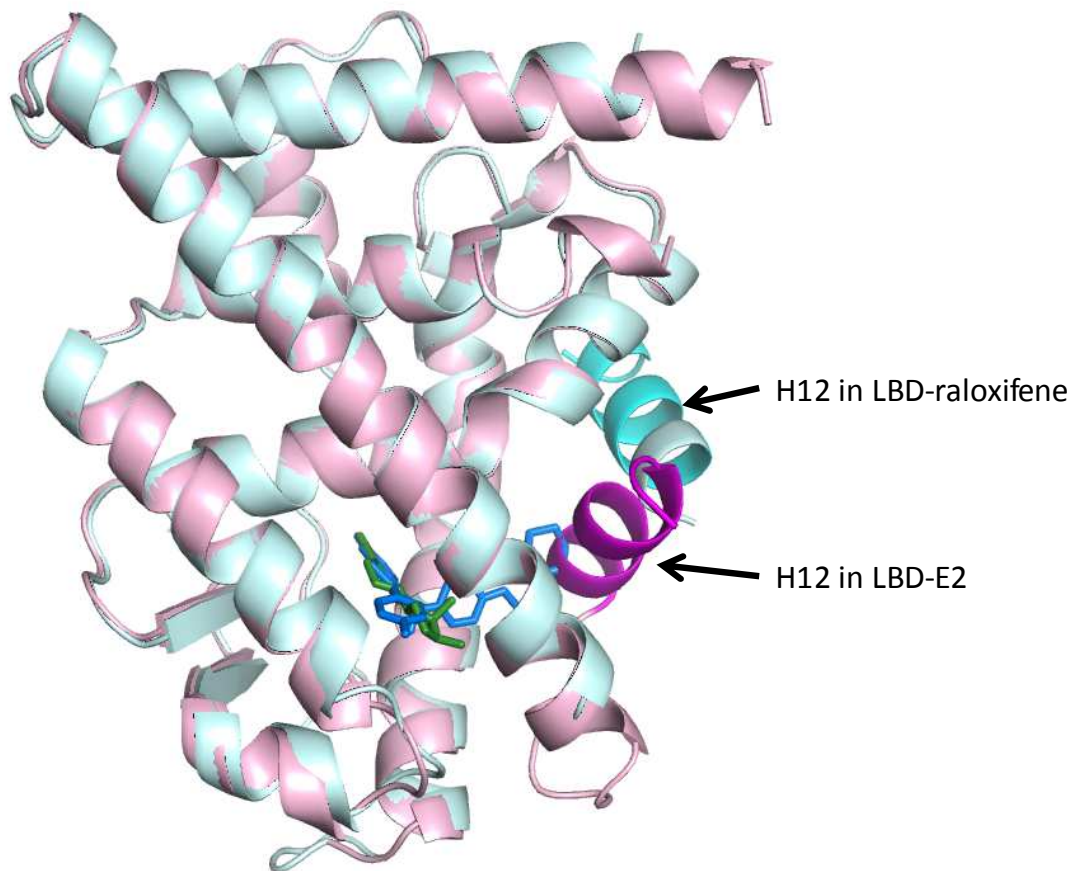


Figure 3.5. The structural overlay of hER α /LBD-E2 complex and hER α /LBD-raloxifene complex. hER α /LBD-E2 (PDB: 1ERE) is in light pink and its H12 in purple, while hER α /LBD-raloxifene in cyan and its H12 in cyan (PDB: 1ERR) (145). The significant position change of H12 is critical for hER α activation.

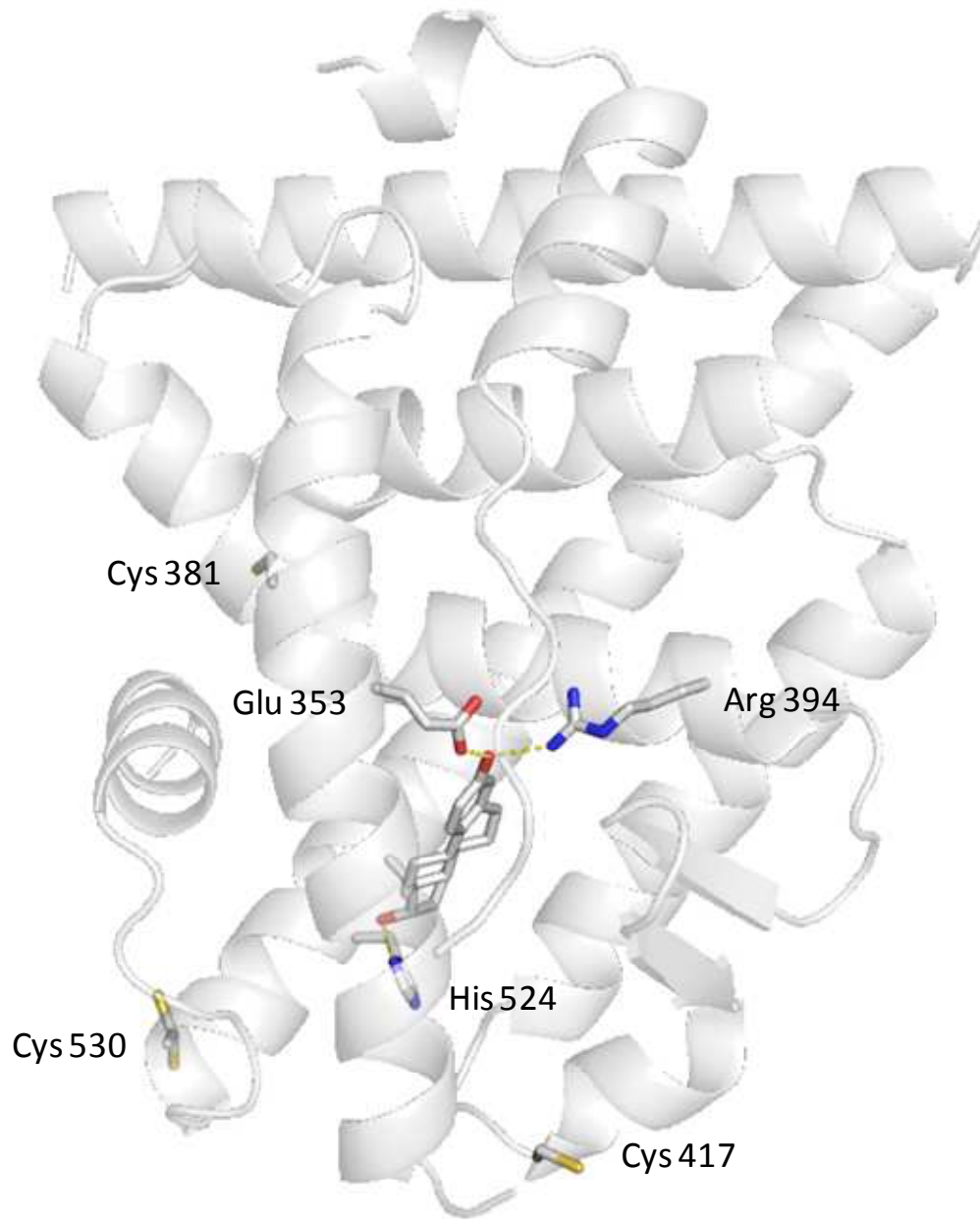


Figure 3.6. Important amino acid residues for hER α /LBD estradiol binding. Residues Glu353, Arg394 and His524 form hydrogen bonds with E2 and are shown in sticks (PDB: 1ERE) (137, 145). Important Cys residues are also indicated (147, 148).

Arg394, His524, and Glu353 form hydrogen bonds with estrogen and mutation of these residues caused lower binding affinity to estradiol (**Figure 3.6**) (145). In addition, some cysteine residues in the LBD are also important for ligand binding, including Cys381, Cys417 and Cys530, and mutants of these residues have significantly decreased estrogen binding affinity (147, 148).

3.5 Scope of the Dissertation Research

The goals of studies in Chapter 4 of this dissertation are (1) to characterize the binding affinity of Cd²⁺ to purified hER α ligand binding domain as compared with estrogen using fluorescence spectroscopy, (2) to study the conformational changes of hER α upon Cd²⁺ or estrogen binding using amide hydrogen/deuterium exchange mass spectrometry, and (3) to identify the possible binding site(s) of Cd²⁺ in hER α ligand binding domain using mass spectrometry and other approaches. This research will determine if Cd²⁺ physically interacts with the hER α ligand binding domain and causes similar structural changes as estrogen that are important for activation, but it will also provide additional knowledge of biological targets of chronic Cd²⁺ toxicity.

CHAPTER 4

THE STUDY OF CADMIUM BINDING TO HUMAN ESTROGEN RECEPTOR AND RELATED STRUCTURAL CHANGES

4.1 Introduction

Human estrogen receptor alpha (hER α) is a transcription factor that regulates the gene expression, cellular proliferation, and cell differentiation upon the binding of its native ligand, 17 β -estradiol (E2) (**Figure 4.1A**). However, some metal ions such as Cd $^{2+}$ are capable of activating the transcription factor function of hER α *in vivo*, and Cd $^{2+}$ is proposed to bind directly to the protein (128, 137). There are two potential Cd $^{2+}$ binding sites: the DNA binding domain (DBD) where Cd $^{2+}$ could replace Zn $^{2+}$ from the zinc finger motif (149, 150) and the ligand binding domain (LBD) where Cd $^{2+}$ binding could trigger the similar conformational changes as estradiol (137).

The changes in protein structure and DNA binding affinity upon Cd $^{2+}$ replacement in the two zinc finger motifs (both the P-box and D-box fingers) has been thoroughly studied *in vitro* with truncated, purified DBD domain comprised of residues 176–250 (149, 150). The Cd $^{2+}$ –DBD complex has similar affinity for the estrogen response element (ERE) DNA motif as the Zn $^{2+}$ –DBD complex (149). The replacement of Zn $^{2+}$ by Cd $^{2+}$ only caused subtle conformational changes in secondary structure based on circular dichroism spectroscopy (150). In these studies, protein denaturation methods were used to prepare the Cd $^{2+}$ –DBD complex and apo–DBD (residues 176–250) (150), thus, additional *in vivo* evidence is required for this hypothesis.

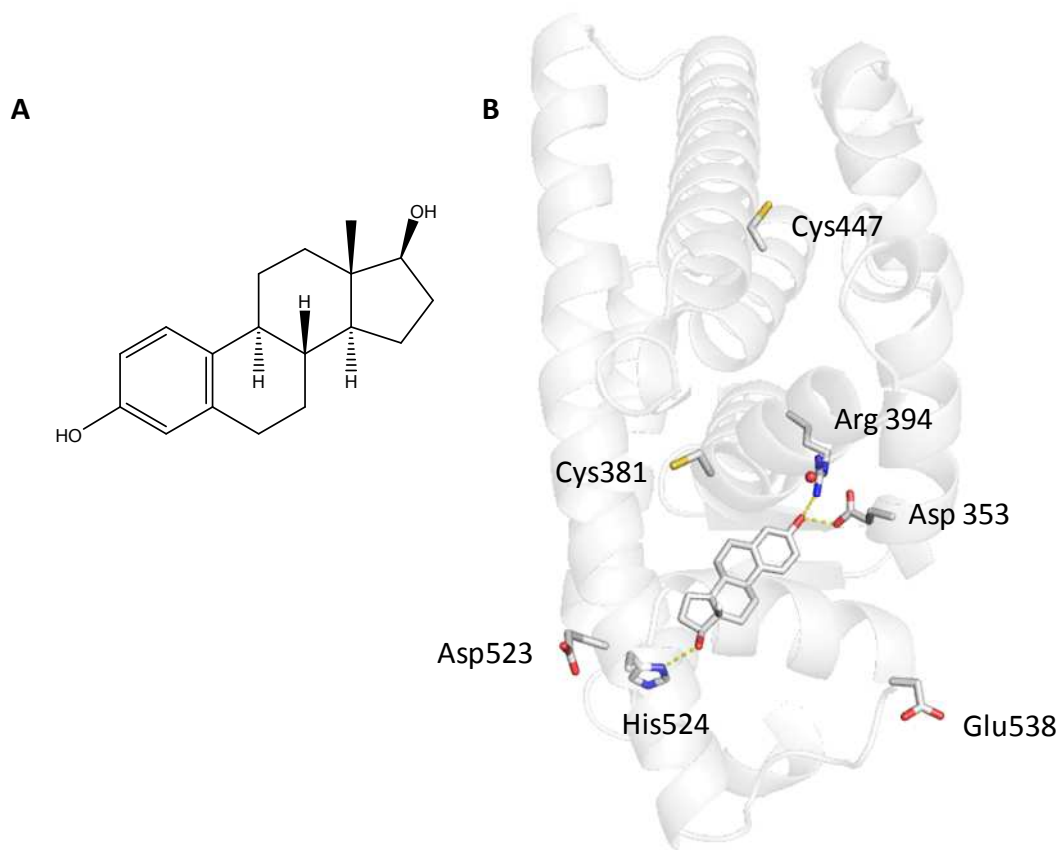


Figure 4.1. (A) The structure of 17β-estradiol. (B) The possible amino acid residues involved in Cd²⁺ binding and activation of hERα, adapted from the report of Stoica *et al* (137) and PDB structure 1ERE (145). Cys381, Cys447, Asp524, His524 and Glu538 were suggested as the possible binding ligands, while Arg394, Asp353 and His524 form hydrogen bonds with E2.

On the other hand, Stoica and coworkers showed that Cd^{2+} binds to the LBD and activated the protein as a transcription factor (137). With purified full-length hER α from MCF-7 cancer cells, they reported that Cd^{2+} binds to hER α with a dissociation constant (K_d) of 0.4 nM and is a non-competitive inhibitor of E2 binding to hER α (137). As a non-competitive inhibitor, it is suggested that Cd^{2+} binds to hER α somewhere other than E2 ligand cavity and changes the three-dimensional structure so that E2 binding is weakened. In addition, hER α site-directed mutants demonstrated that Cys381, Cys447, Glu523, Asp538 and His524 (all in the LBD) were involved in Cd^{2+} binding or activation of hER α (**Figure 4.1B**) (137); however, these amino acid residues may not be directly involved in Cd^{2+} binding. First, these suggested residues are broadly distributed in the protein based on the three-dimensional structure of the LBD, and are unlikely to all participate in Cd^{2+} coordination. Second, the Glu523, Asp538 and His524 residues in Cd^{2+} -LBD complex were not protected in the chemical modification experiments as expected, which indicated these residues may not be directly involved in Cd^{2+} binding (151). Third, mutagenesis of cysteine residues Cys381 and Cys447 resulted in significantly decreased binding affinity for E2, but not for Cd^{2+} (137, 147, 148), which could be the result of an altered protein conformation. Finally, His524 is known to form a hydrogen bond with E2 (145), thus the mutagenesis of this residue could cause considerable changes in E2 binding and hER α activation.

To fully understand the mechanism of Cd^{2+} activation of hER α , knowledge of the hER α structure with E2 and Cd^{2+} is important. Although the individual structure-function relationships of the DBD and LBD have been reported, critical information is still missing as there are no structures of full-length hER α , apo-DBD, or apo-LBD. The lack of this information complicates the study of hER α activation and hinders the research of hER α related diseases and drug development.

Full-length hER α is notoriously difficult to purify (152, 153), and the concentration of commercially-available recombinant hER α purified from human cell lines is about 4 μ M (Thermo Scientific). Because of the low concentrations, neither nuclear magnetic resonance (NMR) spectroscopy nor x-ray crystallography are viable tools to study ligand-induced conformational changes in hER α . Here, we utilize backbone amide hydrogen/deuterium exchange mass spectrometry (HDX-MS) to localize the conformational changes in hER α that occur upon E2 or Cd $^{2+}$ binding in solution. The backbone amide hydrogens participate in hydrogen bonds that stabilize protein secondary structure, such as in α -helices and β -strands, and the rates of breaking and reforming these hydrogen bonds describe the fluctuation of protein conformational states (154). At room temperature and neutral pH, when the protein is exposed to deuterated solvent, the backbone amide hydrogens exchange with deuterium in the environment. The rate of exchange is determined by the rate of hydrogen bond breakage (*i.e.*, protein backbone dynamics), and deuterium access to individual amides (*i.e.*, solvent accessibility), and chemical environment (155). By comparing the amide deuterium incorporation rate profiles of hER α in three different states (*e.g.*, apo-protein, E2-bound, Cd $^{2+}$ -bound), it is possible to localize the binding site(s) and reveal conformational changes as the consequence of ligand binding, which could shed light on hER α activation by metalloestrogens like Cd $^{2+}$ (155).

Griffin and coworkers have reported HDX-MS experiments with hER α LBD (residues 298–554) with E2 with and without E2 showed minimal conformational changes upon E2 binding (156). However, the x-crystallography structures of hER α LBD indicate that E2 forms hydrophobic interactions with the binding cavity of LBD (145), which will greatly block the solvent accessibility as well as the dynamics of involved peptides. Thus, it is necessary to re-

measure the deuterium incorporation rates of hER α LBD upon the binding of E2 and compare it to the changes caused by Cd²⁺ if there are any.

In the present work, we demonstrated that Cd²⁺ binds to the LBD of hER α with 1:1 molar ratio using intrinsic tryptophan fluorescence titrations. In addition, the HDX-MS analysis of apo-LBD, E2-LBD, and Cd²⁺-LBD revealed structural changes for E2-bound versus Cd²⁺-bound hER α LBD. Estradiol binding leads to conformational changes in the dimerization region, the E2 binding cavity, and the loop between helix H11 and helix H12. Cadmium demonstrated some similar changes at both dimerization region and helix H12 despite some differences. To our knowledge, this is the first direct evidence that demonstrates hER α LBD undergoes structural changes upon Cd²⁺ binding, and these changes are similar to the ones caused by E2 binding. This study will contribute to understanding the role of Cd²⁺ as metalloestrogen and clarify the potential impact of heavy metals in the ER-positive breast cancer development.

4.2 Methods and Materials

4.2.1 Materials

All buffers were prepared with Chelex-treated Milli-Q deionized water. The 4-(2-hydroxyethyl)-1-piperazineethanesulfonic free acid (HEPES) was from Calbiochem (Billerica, MA), Tris (2-carboxyethyl)-phosphine hydrochloride (TCEP) from Amresco (Solon, OH), and ethylenediaminetetraacetic acid (EDTA) from VWR. *Escherichia coli* strain BL21(DE3)/pLysS was from Agilent (Santa Clara, CA), Luria Broth and carbenicillin was from Teknova. Chloramphenicol from Genlantis, isopropyl- β -D-thiogalactopyranoside (IPTG) was from EMD. Phenylmethylsulfonylfluoride (PMSF) and 5,5'-dithiobis (2-nitrobenzoic acid) (DTNB) were from Biosynth. Standard metal solutions from PerkinElmer. Potassium phosphate (NaH₂PO₄) was purchased from Fisher Scientific, and the buffers were made with HPLC grade water and

acetonitrile, which were purchased from EMD. Deuterium oxide (D₂O, 99.99%) was purchased from Acros Organics and porcine gastric mucosa pepsin from Sigma.

4.2.2 Expression and Purification of Full-length hER α in *E. coli*

The cDNA encoding full-length hER α was cloned into pET-21b, pCold and pMAL (kindly supplied by Dr. Carol Duffy, University of Alabama) plasmids, respectively, with standard molecular cloning methods. A histidine₆-tag was inserted at the C-terminus of full-length hER α in the vectors of pET-21b and pCold using QuikChange Lighting site-directed mutagenesis. Recombinant plasmids pET-21b/hER α -6His, pCold/hER α -6His, and pMAL/hER α -6His were transformed into *E. coli* strains BL21(DE3)/pLysS or CD146 (kindly supplied by Dr. Carol Duffy, University of Alabama) competent cells for protein expression.

For the expression of pET-21b/hER α -6His and pMAL/hER α -6His, the transformed cells were selected on Luria Bertani (LB) agar supplied with 100 μ g/mL ampicillin and 34 μ g/mL chloramphenicol, and colonies were inoculated into 1 L of LB liquid medium containing 50 μ g/mL carbenicillin and 34 μ g/mL chloramphenicol. Cells were incubated at 37 °C with vigorous shaking until the OD₆₀₀ reached 0.5, at which point IPTG was added to a final concentration of 0.1 mM. The incubation temperature was decreased at a rate of 5 °C per 15 min, until cells reached 20 °C. Cells were incubated overnight with shaking and harvested by centrifugation at 4 °C. The expression of pCold/hER α -6His was performed similarly, except that after the addition of IPTG to final concentration of 0.1 mM, the incubating temperature was decreased to 15 °C for overnight. All following purification steps were performed strictly on ice or 4 °C, and buffers were ice cold.

The *E. coli* cells overexpressing hER α -6His from pREP3X/hER α -6His and pCold/hER α -6His plasmids were resuspended separately with Buffer P (50 mM NaH₂PO₄, 300 mM

NaCl, 5 mM β -mercaptoethanol, pH 7.0) supplied with 1 mM PMSF, then lysed with a Branson Sonifier with an output of 3.5 and a 50% duty cycle for total of 12 min. The insoluble fraction was removed with centrifugation at 12,000 rpm for 20 min. The supernatant was incubated with pre-equilibrated HisPur Cobalt Resin (Thermo Scientific) with gentle shaking overnight at 4 °C. HER α -6His was eluted with 150 mM imidazole in Buffer P. The purification results were analyzed with 12% SDS-PAGE.

The maltose-binding protein fused hER α (MBP-6His-hER α) was overexpressed in *E. coli* strain BL21(DE3)/pLysS. The cells with MBP-6His-hER α protein were lysed as previously described in Buffer P with 1 mM PMSF, and the insoluble fraction was removed with centrifugation. The supernatant was mixed with HisPur Cobalt resin and incubated for 2 h at 4 °C. The mixture was loaded to a 1 \times 10 cm column, and MBP-6His-hER α was eluted with Buffer P supplemented with 150 mM imidazole. The eluted protein was dialyzed against Buffer P to remove imidazole, and the protein concentration was determined by an Agilent UV-visible spectrophotometer at 280 nm, using the extinction coefficient of 0.128 $\mu\text{M}^{-1} \text{cm}^{-1}$. Factor Xa was added with a w/w ratio of 1% of the isolated fusion protein to perform the cleavage to release the MBP tag. The reaction was incubated at 4 °C for 3 h with gentle shaking, and the 6His-hER α was purified using HisPur Cobalt resin. The purification results were analyzed with 8% or 12% SDS-PAGE.

4.2.3 Expression and Purification of Full-length HER α in *S. pombe* Cells

The cDNA encoding full-length ER α was cloned into the plasmid pREP3X with standard molecular cloning protocols, and the 6-Histag was inserted to the C-terminus of hER α with QuikChange Lightning mutagenesis. The recombinant plasmid pREP3X/hER α -6His was transformed into *S. pombe* strain SP870, and the cells were selected and maintained on

Edinburgh Minimal Media (EMM) with 250 mg/L adenine and uracil each (EMM+AU), supplemented with 50 μ M thiamine. For pREP3X/hER α -6His expression, transformed *S. pombe* cells were grown overnight at 30 °C in EMM+AU medium without thiamine until mid-log phase with shaking, then cells were inoculated into 1 L of EMM+AU liquid medium without thiamine to grow 24 h. Cells were harvested with centrifugation at 4 °C.

The *S. pombe* cells with hER α -6His were resuspended with Buffer P with 1 mM PMSF and lysed by vigorous shaking with acid-washed glass beads. The insoluble fraction was removed by centrifugation, and the supernatant was incubated with HisPur Cobalt resin overnight at 4 °C. The hER α -6His was eluted with Buffer P containing 150 mM imidazole and the purification results were analyzed by 12% SDS-PAGE.

4.2.4 Western-blot Analysis

Samples from each purification were analyzed with 8% or 12% SDS-PAGE and the proteins were transferred to a Whatman Protran nitrocellulose membrane with a Bio-Rad Mini Trans-Blot electrophoretic transfer cell (Hercules, CA). The membrane was blocked with 5% BSA, and hER α -6His was detected with mouse monoclonal His-tag primary antibody (Abgent, San Diego, CA) and goat anti-mouse IgG/alkaline phosphatase conjugate secondary antibody (Southern Biotech, Birmingham, AL) using NBT/BCIP staining. Analysis of hER α -6His expression and purity was performed using the UVP MultiDoc-It imaging system (Upland, CA).

4.2.5 Purification of HER α LBD

The DNA sequence encoding the hER α LBD from residue 297 to residue 573 was amplified from hER α cDNA and cloned into pET-21b using restriction enzymes *Xho*I and *Nde*I, and the cloning result was verified by DNA sequencing. Recombinant pET-21b/LBD was transformed into *E. coli* BL21(DE3)/pLysS competent cells. The transformed cells were selected

on Luria Bertani (LB) agar supplied with 100 $\mu\text{g}/\text{mL}$ ampicillin and 34 $\mu\text{g}/\text{mL}$ chloramphenicol. Colonies were inoculated into 1 L of LB liquid medium containing 50 $\mu\text{g}/\text{mL}$ carbenicillin and 34 $\mu\text{g}/\text{mL}$ chloramphenicol. Cells were grown at 37 °C with vigorous shaking until the OD_{600} reached 0.4–0.45, then IPTG was added to a final concentration of 0.2 mM. Cells were incubated for another hour at 37 °C and harvested by centrifugation at 4 °C.

All following purification steps were performed strictly on ice or 4 °C, and all buffers are ice cold unless specifically noted. The cell pellet was resuspended in Buffer A (50 mM Tris, 100 mM NaCl, 5 mM DTT, 5% glycerol) with 1 mM PMSF. The resuspended cells were lysed with a Branson Sonifier with an output of 3.5, 50% duty cycle for total of 12 min. The insoluble fraction was collected with centrifugation at 12,000 rpm for 20 min. The supernatant was removed, and the pellet was washed with Buffer A at a ratio of 10 mL Buffer A per 1 gram of lysis pellet. The pellet was collected by centrifugation at 12,000 rpm for 20 min. Residual buffer was carefully removed, and the pellet was thoroughly resuspended with Buffer A with 1% Triton X-100 at a ratio of 10 mL buffer per gram of pellet. The mixture was stirred for 30 min, followed by centrifugation at 12,000 rpm for 20 min. The liquid was removed, and the pellet was thoroughly resuspended with Buffer B (50 mM Tris, 500 mM NaCl, 5 mM DTT, 5% glycerol) at ratio of 5 mL buffer per gram of pellet. The mixture was stirred for 1 h, and the pellet was collected by centrifugation. This pellet was resuspended with Buffer C (50 mM Tris, 1 M NaCl, 5 mM DTT, 5% glycerol) with ratio of 2.5 mL buffer per gram pellet and stirred overnight. The insoluble fraction was removed by centrifugation, and the supernatant was shown to contain hER α LBD, with an estimated purity $\geq 95\%$ based on 12% SDS-PAGE. The concentration of purified LBD was determined by UV-visible spectrophotometry, the analyte having a molar extinction coefficient of 29.35 $\text{mM}^{-1}\text{cm}^{-1}$ at 280 nm.

4.2.6 Preparation of Apo-hER α LBD

Following procedures were performed in a Vacuum Atmospheres anaerobic glove box ($O_2 < 1$ ppm). Purified LBD was reduced and excess metal ions were removed by the addition of 40 molar equivalents of TCEP and 2 mM EDTA, respectively. The reduced and metal-free LBD was dialyzed against Buffer H (50 mM HEPES, 400 mM NaCl, 5% glycerol, pH 7.4, degassed) at 4 °C with 5 buffer exchanges every 8 h. The Cd^{2+} :LBD ratio was less than 0.1 Cd^{2+} per protein as determined by atomic absorption (AA) spectroscopy using a cadmium EDL lamp and a Cd^{2+} standard curve.

4.2.7 Tandem Mass Spectrometry

The purified full-length hER α -6His and hER α LBD was subjected to pepsin digestion and tandem spectrometry (MS/MS). Thirty micrograms of LBD was diluted with HPLC-grade water to a final concentration of 20 μ M in a 50 μ L total volume. Forty microliters of Buffer Q (0.1 M potassium phosphate, pH 2.3) was added to acidify the protein, followed by 10 μ L of 10 M urea and 2 μ L of 5 mg/mL pepsin stock solution (pepsin:LBD ratio is 1:3) and incubated on ice for 5 min. The produced LBD peptides were separated on a 2 mm \times 50 mm Phenomenex C₁₈ column using an Agilent Technologies 1200 series HPLC, with an elution gradient of 2% to 65% acetonitrile with 0.4% formic acid in water. Tandem MS/MS by collision induced dissociation (CID) was performed with the SmartFragTM setting by the Brüker HCTultra PTM Discovery System mass spectrometer in positive ion mode from 300–1500 m/z (30), and the collision gas was helium. Peptide sequencing results were analyzed by PeaksClient 6 (Bioinformatics Solutions).

4.2.8 Free Thiolate Quantitation

A standard DTNB assay was performed in the glovebox at 25 °C to determine the free thiolate content in apo-LBD. Apo-LBD was diluted to 10 μM with 150 μL of 100 mM Tris, 6 M guanidine hydrochloride (GuHCl), 0.3 mM DTNB, pH 8.0. The sample was incubated in the dark for 30 min and the concentration of thiolate groups was determined with UV-visible spectroscopy at 412 nm, using an extinction coefficient of $13.7 \text{ mM}^{-1} \text{ cm}^{-1}$ (157).

4.2.9 Fluorescence Titration of LBD with Estradiol and Cd^{2+}

Intrinsic tryptophan fluorescence titrations were performed at 25 °C using a Spex Fluoromax-3 fluorimeter (Edison, NJ) with an excitation wavelength at 295 nm. Apo-LBD (3.4 μM) in fresh Buffer D was supplemented with 34 μM TCEP and added to a 2 mL cuvette. The titrants were either 140 μM of CdCl_2 or 100 μM of E2 in Buffer D. The CdCl_2 stock concentration was determined by AA spectroscopy. After each addition of titrant, the sample was equilibrated for 5 min with stirring at 25 °C. Fluorescence emission spectra were collected at 343 nm and corrected for dilution and background fluorescence. Each titration was repeated three times and averaged. The initial fluorescence intensity (F_0) was subtracted from each titration point ($F_i - F_0$), which was plotted against the molar equivalents of ligand:LBD to obtain stoichiometry and also plotted against the concentration of ligand to obtain the binding affinity using **Equation 4.1**.

$$F - F_0 = \frac{[\text{titrant}][\text{LBD}_{\text{total}}]}{K_d + [\text{titrant}]} \quad (4.1)$$

4.2.10 Amide Hydrogen/Deuterium Exchange Mass Spectrometry

The aerobic HDX reactions were performed in triplicate with apo-LBD, E2-LBD (10:1 molar ratio) and Cd^{2+} -LBD (10:1 molar ratio). Deuterium exchange reactions were performed in 0.2 mL thin-walled tubes containing 5 μL of 200 μM LBD stock (apo, with E2 or Cd^{2+}) and were

initiated with 45 μL of deuterium oxide (99.99% atm D_2O). Samples were incubated at 25 $^\circ\text{C}$ with D_2O for 15 s, 30 s, 45 s, 1 min, 2 min, 5 min, 10 min, 30 min and 1 h. The exchange reactions were quenched with 40 μL of ice cold Buffer Q (0.1 M potassium phosphate, pH 2.3) and transferred to an ice bath. Ten microliters of 10 M urea (pH 2.3) and 10 μg of pepsin were added and incubated on ice for 5 min. Pepsin generated peptides were separated by HPLC with a 2 mm \times 50 mm Phenomenex C_{18} column, with the solvent bottles, injector, column and tubing submerged in an ice bath. Solvent A contains 98% HPLC water, 2% acetonitrile, and 0.4% formic acid; while Solvent B contains 98% acetonitrile, 2% HPLC water, and 0.4% formic acid. The elution gradient was 2% to 65% acetonitrile over 15 min. Mass spectra were recorded using positive ion electrospray ionization with a capillary temperature of 270 $^\circ\text{C}$. A control for natural isotope abundance (m_0) was prepared as for other samples except that the protein was diluted with H_2O instead of D_2O . Due to the instability of the LBD in solution, the theoretical number of exchangeable amide hydrogens for each peptide was used as the m_{100} control. HDX-MS data were averaged and processed by HDExaminer (Sierra Analytics, Modesto, CA). The percentage of deuterium incorporation (%D) was calculated as in **Equation 4.2**.

$$\%D = \left(\frac{m_t - m_0}{m_{100} - m_0} \right) \times 100 \quad (4.2)$$

The values m_0 , m_t , and m_{100} are the centroid of the peptides in the non-deuterated, the partially deuterated at time t , and the theoretical fully-deuterated control peptides. The percentage of deuterium incorporation was plotted as a function of time, and the resulting curve for each peptide was fit to single or double first order rate expressions. The difference of deuterium incorporation between apo-LBD and ligand bound-LBD ($\Delta\%D$) was plotted against time (t) for each peptide, and standard student's t-test was performed to analyze the significance.

4.3 Results

4.3.1 The Purification of Full-length hER α from *E. coli* and *S. pombe*

The overexpression of full-length hER α from the plasmid pET-21b was inhibitory to the growth of *E. coli*, and the full-length protein (~66 kDa) was degraded during expression as evidenced by smaller induced protein bands (**Figure 4.2A**, lane 3). Some full-length protein was extracted from inclusion bodies using a denaturing method with 8 M urea (**Figure 4.2A**, lane 5); however, hER α precipitated on renaturation (data not shown). For hER α expressed in the *E. coli* strain CD146, the lysis supernatant was incubated with HisPur Cobalt resin and eluted with imidazole (**Figure 4.2 B**). The recombinant full-length hER α was degraded, and a stock of hER α was obtained with very low concentration (~5 μ M). The vector pCold, which is designed for overexpression insoluble protein in *E. coli* using temperature induction, resulted in no full-length hER α expression (data not shown). Lastly, the expression of fusion protein MBP–6His–hER α was successful; however the protein was also degraded during expression and purification, despite the utilizing of protease inhibitors and strict on-ice procedure (**Figure 4.3**). We managed to purify a small amount of full-length hER α overexpressed from the vector pET-21b and submitted to tandem mass spectrometry, and the purified protein was identified as hER α with low coverage (data not shown). The concentration of protein stock is too low to perform HDX/MS or metal-binding titrations.

Because there are multiple post translational modification (PTM) sites in full-length hER α , and this process only occurs in eukaryotic cells, we tried overexpression of hER α in the yeast *Schizosaccharomyces pombe* using a plasmid under the *nmt1* promoter (no message with thiamine). Indeed, degradation of hER α is significantly relieved (**Figure 4.4A and B**). The purified hER α from *S. pombe* was digested with pepsin and analyzed with tandem mass

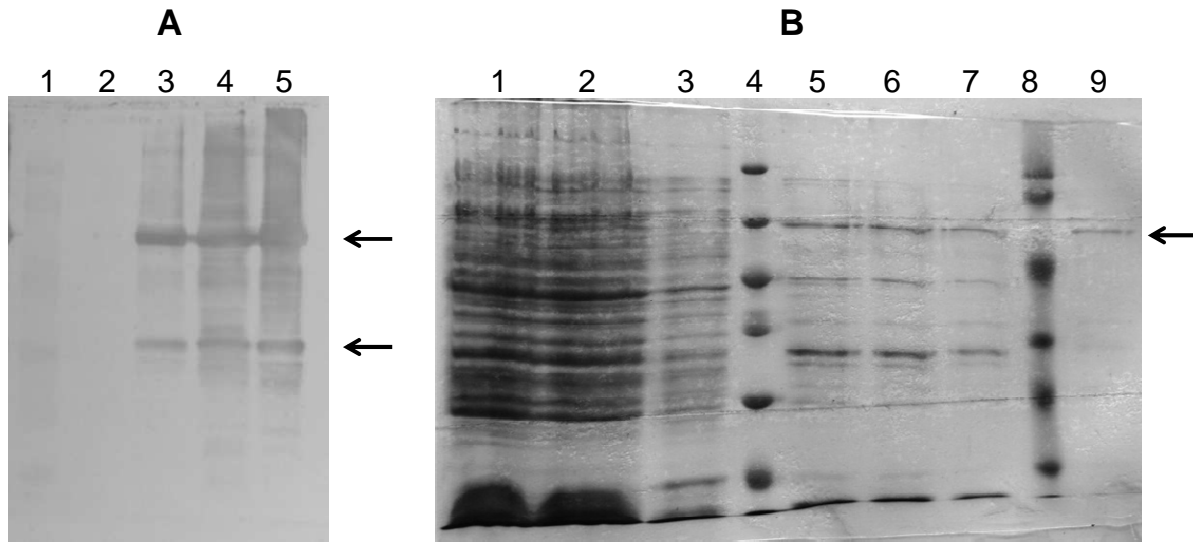


Figure 4.2. The expression and purification of full-length hER α in pET-21b in CD146 *E. coli* strain. (A) The western blotting against hER-6His demonstrates the protein was degraded during expression in the vector pET-21b and CD146 strain, and some full-length protein was in the inclusion bodies. Lane 1, prestain protein ladder; lane 2, the uninduced cells; lane 3, the induced cells; lane 4, lysis supernatant; lane 5, lysis pellet. (B) The purification of hER α from lysis supernatant with Hispur resin. Lane 1, lysis supernatant; lane 2, flowthrough; lane 3, wash; lane 4, prestain protein molecular weight ladder; lane 5, 150 mM imidazole elution fraction 1; lane 6, 150 mM imidazole elution fraction 2; lane 7, 150 mM imidazole elution fraction 3; lane 8, protein molecular weight ladder; lane 9, 250 mM imidazole elution fraction 1; lane 10, 250 mM imidazole elution fraction 2.

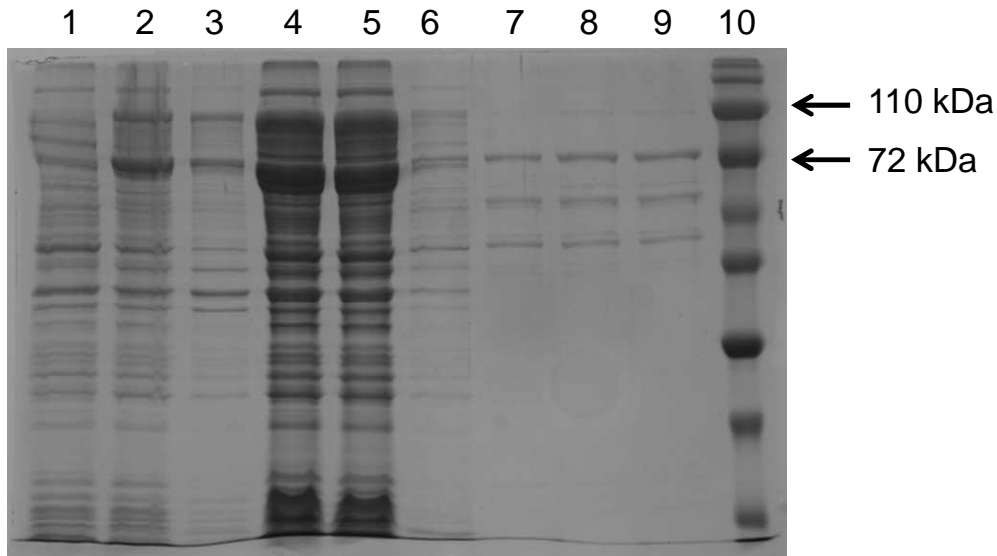


Figure 4.3 The expression and purification of MBP-6His-hER α from BL21(DE3)pLysS

cells. The 12% SDS-PAGE gel of MBP-6His-hER α expression and purification process. Lane 1, uninduced; lane 2, induced; lane 3, lysis pellet; lane 4, lysis supernatant; lane 5, flowthrough of HisPur Cobalt resin column; lane 6, the buffer wash of protein loaded HisPur Cobalt resin; lane 7, the 10 mM imidazole wash of protein loaded HisPur Cobalt resin; lane 8, the 150 mM imidazole elution 1 of HisPur Cobalt resin column; lane 9, the 150 mM imidazole elution 2 of HisPur Cobalt resin column; lane 10, the protein molecular weight ladder.

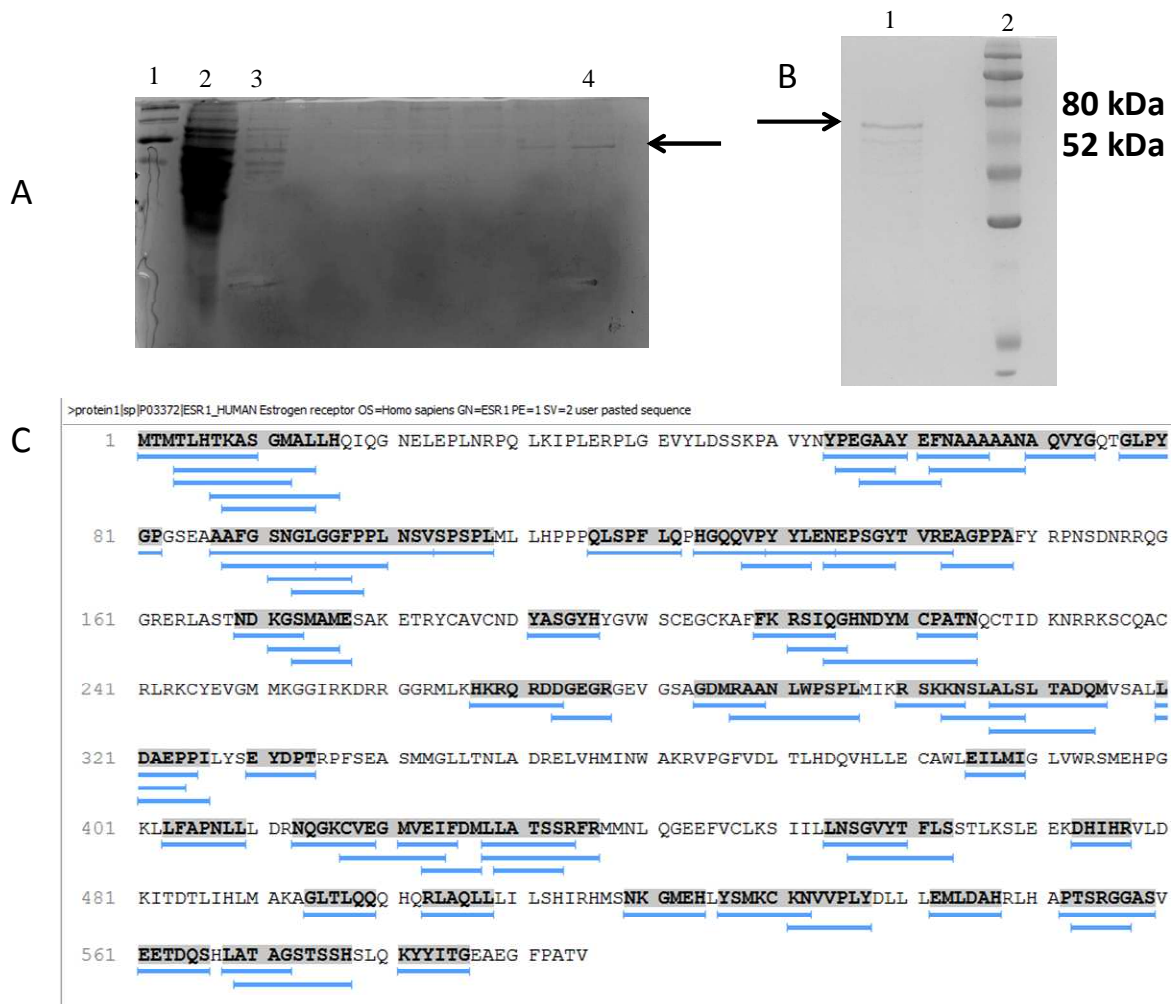


Figure 4.4. The purification process and final product of full-length hERα-6His in *S. pombe*. (A) The HisPur Cobalt resin purification of hERα-6His. Lane 1, protein molecular weight ladder; lane 2, cell lysate of *S. pombe* cells overexpressed hERα; lane 3, the flowthrough of HisPur Cobalt resin column; lane 4, the 150 mM imidazole elution which contains hERα-6His. (B) The 150 mM imidazole elution of HisPur Cobalt resin column was dialyzed against Buffer H through a 50 kDa dialysis membrane (lane 1). (C) The tandem MS/MS mapping result of hERα-6His purified from *S. pombe*.

spectrometry and gave a peptide coverage of 50% (**Figure 4.4C**). However, the concentration of purified hER α was still low, and attempts of to concentrate the protein led to precipitation. Thus, we turned our focus from full-length hER α to the ligand binding domain (LBD).

4.3.2 The Purification of the Ligand Binding Domain

The ligand binding domain of human estrogen receptor α (LBD) was purified by immobilized affinity chromatography and the process was monitored by a Coomassie-stained SDS-PAGE. An overloaded gel demonstrated the purity to be $\geq 95\%$ (**Figure 4.5A**). Pepsin digestion and tandem MS/MS was performed and the peptide sequencing data was analyzed by PeaksClient. The identified peptides covered more than 95% of the LBD amino acid sequence (**Figure 4.5B**), and among them, peptides that cover 71.5% of the LBD amino acid sequence are appropriate for HDX-MS analysis (**Figure 4.5C**). However, the peptides localized at helix H11 are missing, thus we cannot obtain detailed deuterium incorporation profiles for peptides in this region. Thus, we cannot rule out the possibility that this region contains the binding site(s) of Cd $^{2+}$. Since Cd $^{2+}$ is the metal of interest, atomic absorption analysis was also performed to confirm the purified LBD contains less than 0.1 equivalent of Cd $^{2+}$ per monomer.

4.3.2 Quantification of the Reduced Thiol Groups in Apo-LBD

Because reducing agents in buffers are capable of binding Cd $^{2+}$, after purification of apo-LBD, reducing agent was removed via dialysis in an anaerobic chamber. Cysteine residues in LBD may be critical for both E2 and Cd $^{2+}$ binding (*145*), so it was necessary to determine the number of reduced cysteine thiolates in the protein and ensure that thiol-based reducing agents were completely removed. After extensive anaerobic dialysis the concentration of free thiolates of apo-LBD was determined with a DTNB assay (*157*). In this assay, DTNB forms a mixed disulfide with thiolate groups, releasing the yellow 2-nitro-5-thiobenzoate (NBT $^{-}$) ion which can

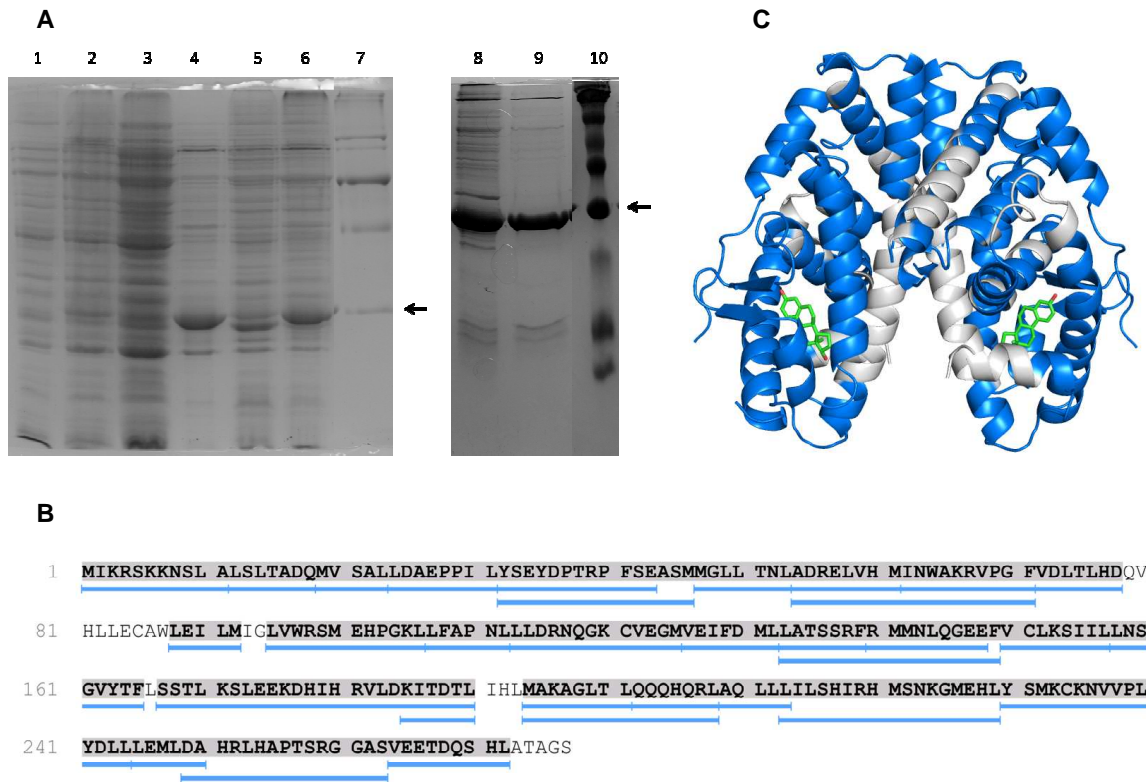


Figure 4.5. The purification and LC-MS/MS mapping of hER α LBD. (A) The 12% SDS-PAGE gel demonstrated the purification process of LBD. Lane 1, uninduced; lane 2, induced; lane 3, lysis supernatant; lane 4, lysis pellet; lane 5, buffer A wash supernatant; lane 6, Buffer A with 0.1% Triton X-100 wash supernatant; lane 7, Rockland protein molecular weight ladder; lane 8, Buffer B wash supernatant; lane 9, buffer C wash supernatant, contains hER α LBD with purity \geq 95%; lane 10, Prosieve protein molecular weight ladder. (B) Peptides that identified by tandem MS/MS cover more than 95% of the LBD amino acid sequence. (C) The location of identified peptides for HDX-MS experiments and data analysis. The usable peptides are highlighted in blue (PDB 1ERE) (145).

be detected spectrophotometrically ($\epsilon_{412} = 13.7 \text{ mM}^{-1}\text{cm}^{-1}$ in 6 M GuHCl). The DTNB assay indicated that the purified protein contained 4.08 ± 0.11 thiol groups per LBD monomer. Thus, all four cysteine residues in apo-LBD were in the reduced state and competent to coordinate metals. We also demonstrated that the reducing agent was removed successfully.

4.3.3 Estradiol Titration of LBD

Each molecule of LBD contains three Trp residues (W360, W383, and W393), and they could be potential indicators of environmental changes upon ligand binding by fluorescence spectroscopy. We titrated the LBD with estradiol (E2) and measured the Trp emission at 343 nm. The fluorescence intensity decreased as a function of E2 concentration so the environment surrounding one or more tryptophan residues was altered in the binding process. The decrease of emission at 343 nm was plotted against the molar equivalents of E2 added, and an approximate 1:1 stoichiometry was confirmed (**Figure 4.6B**). When the emission intensity was plotted against the concentration of E2 in solution at each titration point and fit to a 1 site binding model, a dissociation constant of $0.76 \pm 0.16 \text{ }\mu\text{M}$ was obtained (**Figure 4.6A**). Because the titration was performed under stoichiometric conditions (*i.e.*, there is no “free” E2 in the titration), our reported K_d is considered an upper limit, and the actual K_d is lower than can be measured with this assay. Thus, the purified apo-LBD is capable of binding E2 with correct stoichiometry and high affinity (125).

4.3.4 Cd^{2+} Titration of LBD

Stoica *et al.* reported that Cd^{2+} binds purified full-length hER α with a 1:1 binding stoichiometry and a K_d of 0.4 – 0.5 nM (137). Because this binding constant was determined for full-length hER α , the Cd^{2+} binding stoichiometry and dissociation constant for only the LBD must be determined for our experiments. A fluorescence titration monitored the possible

environmental changes to tryptophan residues caused by Cd^{2+} binding. As shown in **Figure 4.6D**, Cd^{2+} binds to LBD with a binding stoichiometry of 1:1, which agrees with other reports (137). We also determined the dissociation constant of Cd^{2+} -LBD complex is $0.71 \pm 0.12 \mu\text{M}$ as an upper limit of the actual K_d since the titration was performed under stoichiometric conditions (**Figure 4.6C**). Thus, we demonstrated that the purified apo-LBD is capable of binding one Cd^{2+} ion with high affinity as reported for full-length hER α .

4.3.5 The Deuterium Incorporation of E2-LBD

The percentage of deuterium incorporation of peptide backbone amide at a given time is determined by the solvent accessibility (*i.e.*, peptides buried in the core of protein vs. peptides on the surface of protein) and the structural stability (α -helices and β -sheets vs. random coils) (158). The percentage of deuterium incorporated in the first 15 sec of a HDX time course is utilized to estimate the relative solvent accessibility of backbone amides, and the incorporation rate obtained from the full-time length experiments gives information about the conformational flexibility of the backbone in specific regions of the protein. We compared the HDX rate profiles of apo-LBD (in black) to that of E2-LBD (in red) (**Figure 4.7**).

Several LBD peptides showed decreased solvent accessibility upon E2 binding, as determined by the total percentage of deuterium incorporated after 15 sec. Minor decreases occurred for peptides 311–319 (H2) and 422–428 (H8), with larger decreases for peptides 320–327 (H2-loop), 343–349 (H3), 403–410 (S1-loop-S2), 411–423 (H7), 526–540 (H11-loop-H12) (**Figure 4.7 and Figure 4.8**). These peptides are mapped to the LBD three-dimensional crystal structure in **Figure 4.9A**. These three peptides (343–349, 403–410, and 411–423) form the E2 binding cavity and have the largest decreases in deuterium incorporation

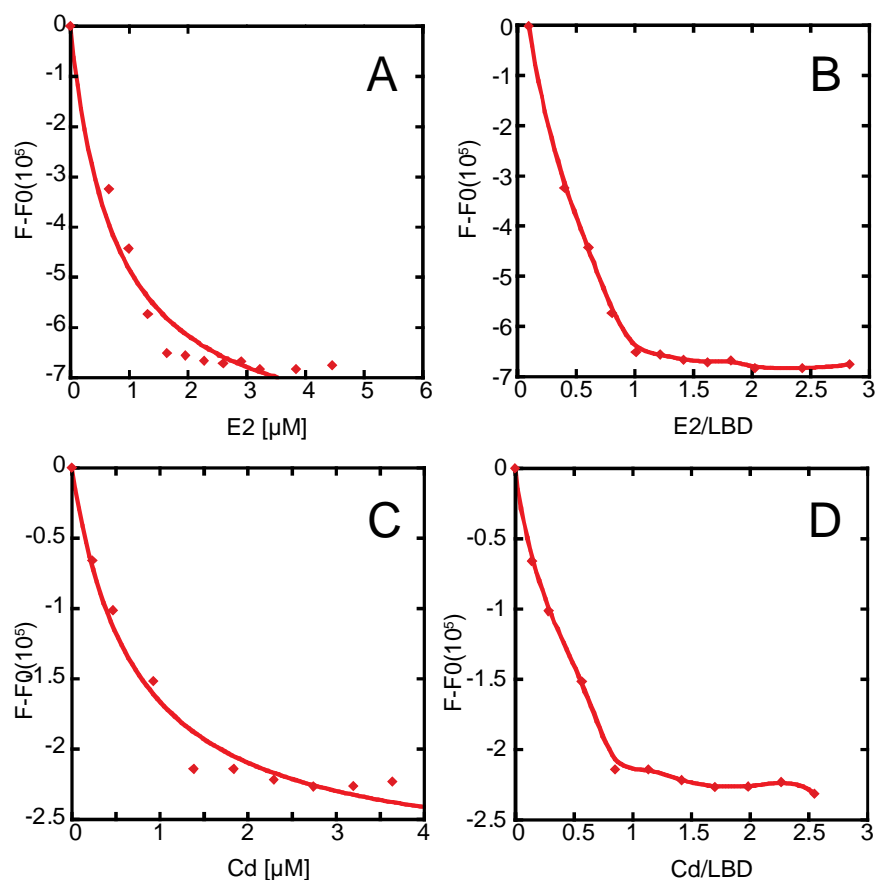


Figure 4.6. The fluorescent titration of E2 and Cd^{2+} to purified LBD. (A) The emission at 343 nm of Trp residues in LBD was corrected for dilution and background fluorescent, then plotted against the concentration of E2. The curve was fitted as described in methods and materials with KaleidaGraph. (B) The emission at 343 nm of Trp residues in LBD was corrected for dilution and background fluorescent, then plotted against the E2 equivalents of LBD. The curve is a smooth connecting of data points. (C) The emission at 343 nm of Trp residues in LBD was corrected for dilution and background fluorescent, then plotted against the concentration of Cd^{2+} . The curve was fitted as described in methods and materials with KaleidaGraph. (D) The emission at 343 nm of Trp residues in LBD was corrected for dilution and background fluorescent, then plotted against the Cd^{2+} equivalents of LBD. The curve is a smooth connecting of data points.

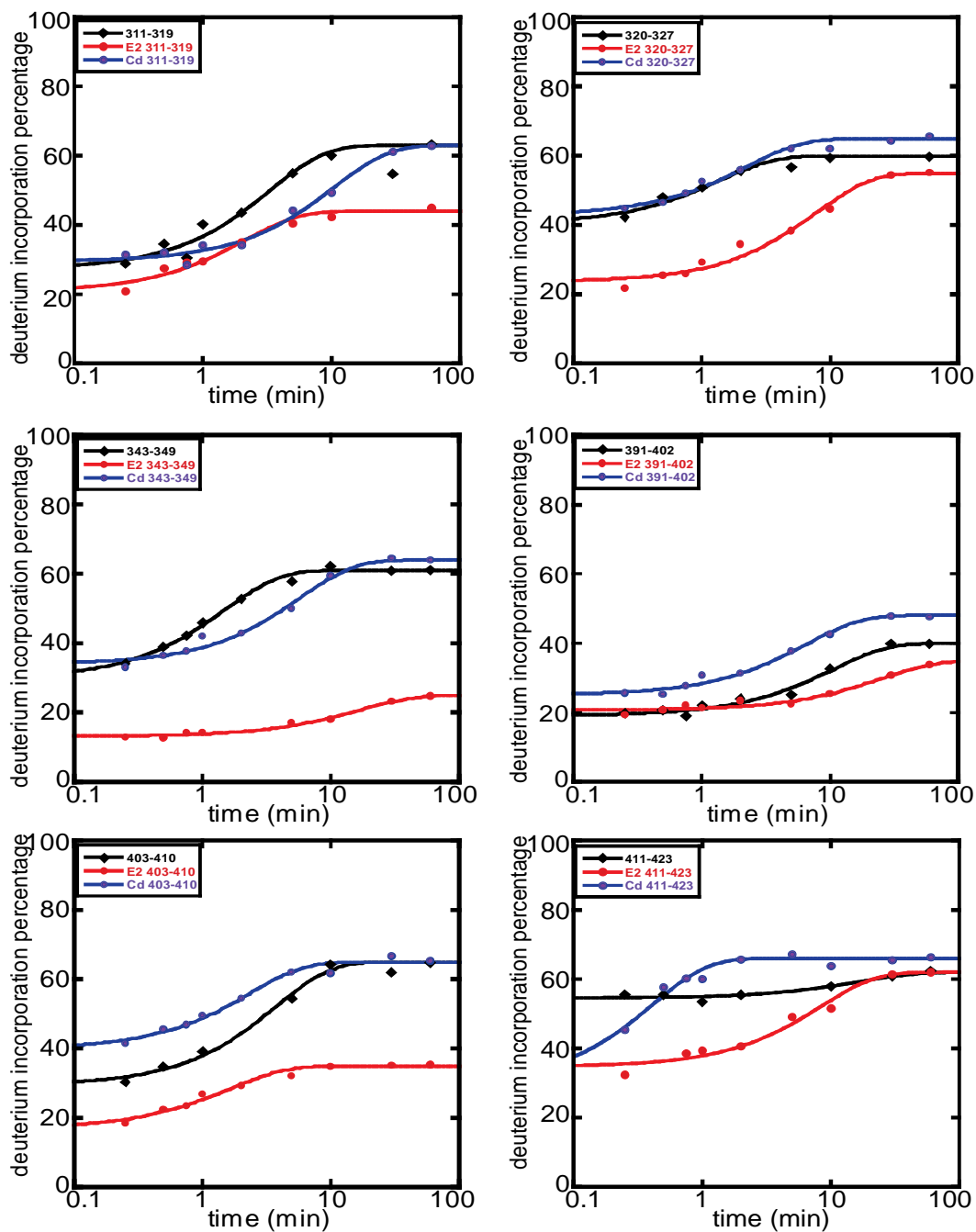


Figure 4.7. The HDX-MS profiles of apo-LBD, E2-LBD, and Cd²⁺-LBD (1). Peptides 311–319, 320–327, 343–349, 391–402, 403–410, and 411–428. The percent deuterium incorporation as a function of time is shown for apo-LBD (black), E2-LBD (red) and Cd²⁺-LBD (blue). Three replicates were performed for each type of LBD complex, and the deuterium incorporation amount was averaged.

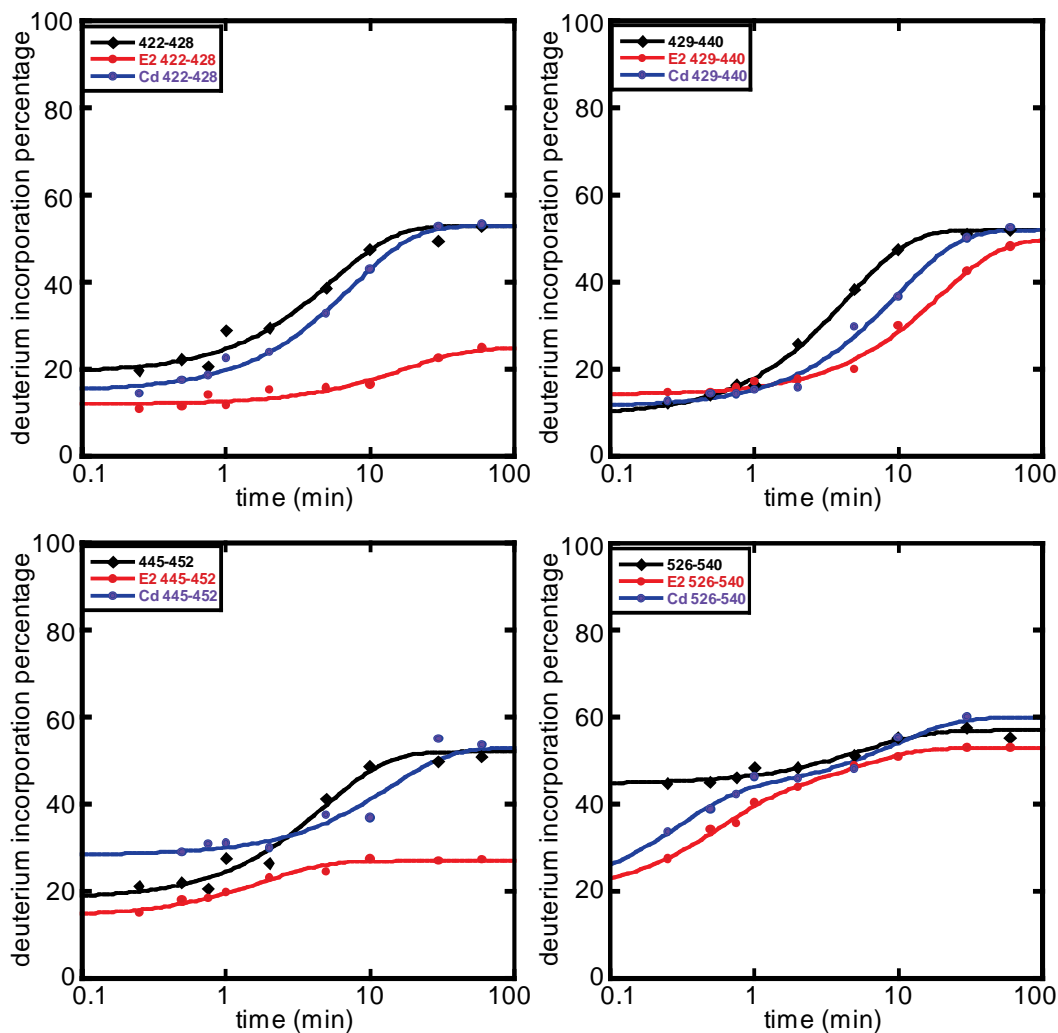


Figure 4.8. The HDX-MS profiles of apo-LBD, E2-LBD, and Cd²⁺-LBD (2). Peptides 422–428, 429–440, 445–452, and 526–540. The percent deuterium incorporation as a function of time is shown for apo-LBD (black), E2-LBD (red) and Cd²⁺-LBD (blue). Three replicates were performed for each type of LBD complex, and the deuterium incorporation amount was averaged.

upon binding E2. They interact with E2 through hydrogen bonds and/or hydrophobic interactions with the steroid ring (145). This observation strongly suggests that E2 binding to hER α LBD caused amides within these regions to become more protected from solvent and the backbone to become more rigid for peptides surrounding the E2 ligand. An additional peptide in the E2 binding site (422–428) showed weaker protection from deuteration (<10%). Peptides 311–319 (Figure 4.10A) exhibited a less than 10% reduction of deuterium incorporation by 15 sec, and this observation agrees that the “sandwich” shaped end of LBD is less affected during E2 binding. Peptide 391–402 demonstrated decreased deuterium incorporation; however, the reduction is not statistically significant.

Peptides of LBD that experienced changes protein backbone dynamics upon E2 binding are shown in **Figure 4.7** and **Figure 4.8**, and mapped to the LBD structure in **Figure 4.9B**. Peptides experiencing slight perturbation in backbone dynamics include 320–327 (H2–loop), 391–402 (H6–loop–S1), and 429–440 (H8). Much more obvious regions of decreased dynamic motions include peptides 311–319 (H2), 343–349 (H3), 403–410 (S1–loop–S2), and 422–428 (H8), and 445–452 (H9). These peptides cluster around the E2 binding pocket, with the exception of peptide 311–319 in helix H2. This same peptide had small changes in solvent accessibility but large changes in dynamics, consistent with a conformational change mediated by E2, but not in the immediate binding pocket. Two peptides had very unique HDX behavior in the E2 bound LBD. Peptides 411–423 (H7) and 526–540 (H11–loop–H12) had an overall decrease in dynamics, but since this peptide ultimately reached the same plateau as apo–LBD, the observed decrease in deuterium incorporation with E2 is probably more related to amide accessibility to D₂O. Peptide 411–423 does not directly interact with E2, but it is a part of the E2 binding cavity which becomes more hydrophobic upon E2 binding, thus the solvent accessibility

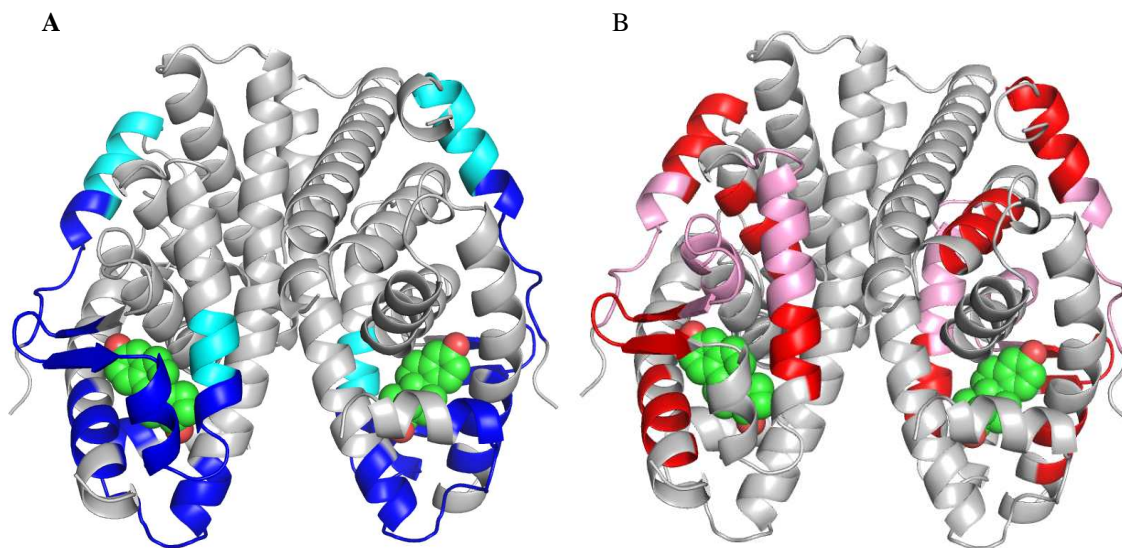


Figure 4.9. The solvent accessibility and dynamic changes of hER α LBD upon E2 binding, determined by HDX-MS. (A) Peptides demonstrated decreased solvent accessibility are mapped on the structure of E2-LBD (PDB 1ERE) (145). The peptides with large decrease are colored in blue, while the ones with small decrease are colored in cyan. (B) Peptides with decreased dynamics are mapped on the E2-LBD structure (PDB 1ERE) (145). The peptides with large decrease of dynamics are colored in red, and the ones with a small decrease are colored in pink.

of this peptide is reduced. Also, peptide 526–540 (H11–loop–H12) is known to undergo major conformational changes because of the transconformation of helix H12 (145). We observed a change in solvent accessibility that could be consistent with increased hydrogen bonding in the presence of E2. It does not appear that E2 binding leads to a large conformational change, which should also affect backbone dynamics.

Overall, our observations suggested that hER α LBD undergoes major conformational changes upon E2 binding, especially within the E2–binding cavity. Other changes induced by E2 include the region proposed to be important for hER α dimerization (H8) and the H11–loop–H12 which is involved in the transconformation of H12 and activation of LBD.

4.3.6 the Deuterium Incorporation of Cd²⁺–LBD

In terms of solvent accessibility as measured by the change in the percentage of deuterium incorporated into the backbone of LBD when Cd²⁺ binds (**Figure 4.7 and Figure 4.8**, in blue), there was only one peptide that had a noticeable decrease. The HDX plot for peptide 526–540 (H11–loop–H12) indicated that Cd²⁺ afforded the backbone in this region almost the same amount of protection from deuterium as E2 (**Figure 4.7 and Figure 4.8**). On the other hand, peptides 403–410 (S1–loop–S2) and 445–452 (H9) reported small increases in solvent accessibility in the presence of Cd²⁺ compared to either apo–LBD or E2–LBD. The increased solvent exposure is opposite of what was observed for E2–LBD. All three peptides with perturbed solvent accessibility consistent with a conformational change and/or ligand protection are mapped to the E2–LBD crystal structure (**Figure 4.10**). Overall, these observed deuterium incorporation rate profiles suggest that Cd²⁺ binds to hER α LBD and triggers conformational changes that could lead to the activation of this transcription factor in the full-length protein in a similar, but not identical manner as E2.

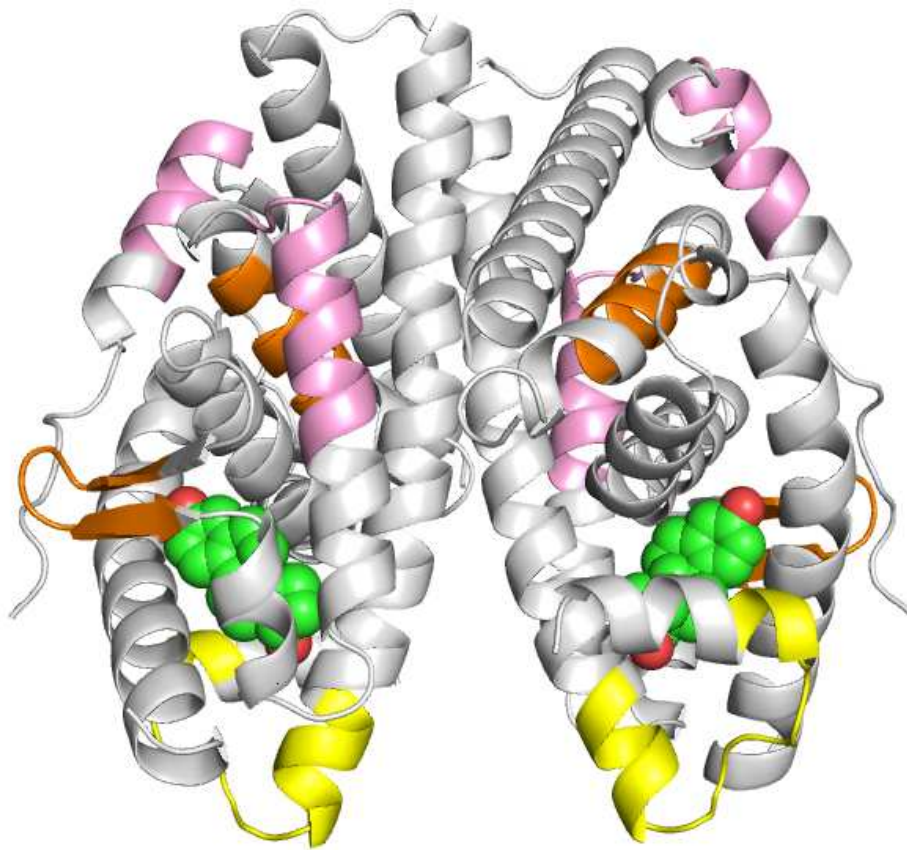


Figure 4.10. The solvent accessibility and dynamic changes of hER α LBD upon Cd²⁺ binding (PDB 1ERE) (145). The peptide with decreased solvent accessibility is colored in yellow (peptide 526–540). Peptides 403–410 and 445–452 demonstrated increased solvent accessibility and they are colored in orange. The peptides with small decreased dynamics (peptide 311–319 and 429–440) are colored in pink.

4.4 Discussion

The heavy metal cadmium is one of the more common co-carcinogens in modern society, and it is linked to cancers such as breast cancer, especially the ER positive type. Both *in vivo* and *in vitro* studies indicate that Cd^{2+} contributes to the development of ER positive breast cancers, potentially through the hER α pathway (128). Human ER α is highly involved in cell-specific regulation of gene expression and cell proliferation, thus its dysfunction is correlated to estrogen-related cancers. Experiments utilizing MCF-7 cancer cell lines and ovariectomized rats demonstrated that Cd^{2+} mimics the effects of E2 activation of hER α (133); however, little is known about the molecular details of Cd^{2+} binding to hER α , including the binding site(s) and related structural changes. Thus, it is important to understand the conformational changes caused by E2 binding and to compare the ones observed in Cd^{2+} -bound hER α .

Most knowledge of the structure-function relationship of hER α come from studies focused on the DNA-binding domain (DBD) and ligand binding domain (LBD). They are also proposed to interact with Cd^{2+} . However, the DBD is less likely to be the target of Cd^{2+} , because *in vitro* experiments demonstrated that Zn^{2+} cannot be directly substituted by Cd^{2+} in native DBD (149) and the Cd^{2+} -DBD showed similar DNA binding affinity as Zn^{2+} -DBD (150), which cannot fully explain the similar transcription factor activity of hER α upon Cd^{2+} binding (128, 133). Thus, the goal of our research was to correlate the structural changes of both full-length hER α and the LBD upon estradiol or Cd^{2+} binding to determine the mechanism of ER α activation by a metalloestrogen.

4.4.1 Barriers to Structural Characterization of Full-length hER α .

Full-length hER α is unstable and difficult to purify both in mammalian cells and *E. coli*, while current commercial full-length hER α is too low in concentration to perform protein

structural studies, such as NMR, x-ray crystallography. In addition, the buffering components to stabilize commercial full-length hER α are incompatible with HDX-MS. To overcome these difficulties, we tested the expression of full-length hER α in both *E. coli* and yeast with numerous expression vectors, including pET-21b, pCold, pMAL, and pREP3X. The protein expression was inhibited in both pET-21b and pCold systems, and the protein was severely degraded. The vector pMAL fused the maltose binding protein (MBP) with hER α to assist expression and folding, which significantly promoted the amount of overexpressed protein. However, the degradation was also severe and the final concentration of purified hER α remained low. On the other hand, when hER α was expressed in the fission yeast *S. pombe*, the protein degradation was partially relieved and more full-length hER α was obtained. We propose this observation is because of the protein chaperone systems in yeast to help nascent proteins fold correctly and the possibility that PTM occurred to stabilize the full-length hER α protein. The possible reason may be the differences in native *E. coli* and yeast proteases, where full-length hER α was more susceptible to proteolysis in *E. coli*. Due to the limits of our experiments, the concentration of final hER α product was still low, but enough for the product to be identified with tandem MS/MS. Further investigation will focus on optimizing the expression and purification conditions of hER α from *S. pombe*, as well as the binding assay and HDX-MS. Instead, we focused on the LBD to obtain useful mechanistic information about E2 and Cd²⁺ activation of hER α .

4.4.2 Estrogen binding to the hER α Ligand Binding Domain

To fully understand the mechanism of Cd²⁺ activating hER α through the LBD, it is important to understand the structural changes of LBD during the binding of its native ligand, E2. The first x-ray crystallography structure of E2-LBD complex was published in 1997 by Brzozowski *et al* and numerous structures of LBD with different ligands are reported, however,

there is no structure for apo-hER α LBD (145, 159). Generally, apo-LBD structures are rare for nuclear receptor-3 family proteins, of which hER α belongs. Thus, little information is known about the process of ligand binding (160), partly because most LBD proteins were purified with immobilized ligand-affinity chromatography, which produced ligand bound complexes (161). The current knowledge of hER α structural changes during E2 binding came from the comparison of E2 and antagonist bound LBD (145). These structures revealed that upon E2 binding, helices H8 and H11 were aligned to form the homodimer, and helix H12 was packed against helices H3, H5/6 and H11. The transconformation of H12 provided an interaction surface for other coactivators with “LXXLL” motifs, which “seal” the E2 binding cavity (146). However, because these structures are in crystals rather than in solution, the real conformational changes are still under debate, especially if the helix H12 undergoes transconformation upon E2 binding (145, 146, 160, 162, 163).

With the limits of NMR and x-ray crystallography in mind, we utilized HDX-MS to study the E2 induced conformational changes of hER α LBD. We examined the deuterium incorporation rate profiles of E2-LBD complex and compared it with that of apo-LBD. Indeed, the most significant deuterium incorporation rates changes were observed for peptides in and around the E2 binding cavity. Among these peptides, helix H3, H8 and strands S1/S2 demonstrated significantly decreased deuterium incorporation amount even after 1 h incubation, which indicated that these peptides were in a more rigid conformation. This observation agrees with that these peptides form hydrophobic interaction with E2 (145). In addition, the significant decreased solvent accessibility of peptides in H2-loop, H7 and H11-loop-H12 suggested there were increased hydrogen bonding interactions for these peptides rather than large conformational changes (no changes from loop to helix).

One of the most interesting findings is the decreased solvent accessibility of peptide 526–540, which contains the end of helix 11, the loop and the beginning of helix H12. As proposed in the “mouse trap” model proposed by Gronemeyer *et al*, the loop extends freely in apo–LBD and becomes partially locked upon E2 binding (164, 165). Our HDX–MS plots can be explained by this model, though other possibilities cannot be ruled out. Another region affected by ligand binding is the dimerization interface formed by helices H8 and H11 (145). Because helix H11 is highly resistant to pepsin digestion (156), this helix is not available for HDX–MS analysis. On the other hand, the helix H8 demonstrated slower deuterium incorporation rates with E2 bound, indicating this helix loses conformational flexibility.

The other form of estrogen receptor is the human estrogen receptor beta (hER β), and the alignment of sequences and structural overlay of hER α and hER β reveal high similarity at the ligand binding domain (**Figure 4.11**). Similar HDX–MS experiments have been performed by Griffin and coworkers for the E2–LBD complex from hER β . Thus, we compared our hER α HDX–MS findings with that of hER β LBD (166). Upon E2 binding, the LBD of hER β showed changes in HDX for peptide 296–309 (helix H3) and peptide 345–362 (beta strands S1/S2), very similar results were reported as ours (peptide 320–327 for helix H3 and peptide 403–410 for beta strands S1/S2 in hER α). The most obvious discrepancy between hER α and hER β HDX–MS was that we observed more pronounced changes in these peptides and in others. The reason for this discrepancy is unknown.

Overall, the deuterium incorporation rate profile of E2–LBD from hER α agrees the formation of hydrophobic core at the E2 binding cavity, the transconformation of H12 and the formation of homodimer. This result sets the comparison standard for the analysis of Cd²⁺–LBD HDX–MS data.

Accession	Description
✓ c 10001	sp Q92731 ESR2_HUMAN Estrogen receptor beta OS=Homo sapiens GN=ESR2 PE=1 SV=2
✓ c 10002	sp P03372 ESR1_HUMAN Estrogen receptor OS=Homo sapiens GN=ESR1 PE=1 SV=2

✓ 10001	1	--MDIKNSPSSL-----NSPSSYNCSILPLEH--GSIYIPSSY--VDSHHEYPA M TFYSPAVM N YSIPSNVTNLE	66	} AF-1
✓ 10002	1	MTMTLHTKASGMALLHQIQGNELEPLNRPQLKIPLERPLGEVYLDSSKPAVYNYPEGAAYEFNAAAAANAQVYGG-TGLP	79	
✓ 10001	67	GGPGRQTTSPNVLWPTPGHLSPLVVRQLSHLYAEPQKSPWCEARSLEHTLPVNRE-----TLKRKV	128	} AF-1
✓ 10002	80	YGPGEAAAFSGNGLGGFPPLNSVSPSPMLLHP P Q L SPFLQPHGQV P YYLENEPSGYTVREAGPPAFYRPN S DRRQ	159	
✓ 10001	129	SGNRCASPVTGPG-----SKRDAHFCAVCS D YASGYHYGV W SCEGCKAFFKR S IQGHNDYICPATN Q CTIDKNRRKSCQA	203	} DBD
✓ 10002	160	GGRERLASTNDKGS M AMESAKETRYCAVCNDYASGYHYGV W SCEGCKAFFKR S IQGHNDYMC P ATN Q CTIDKNRRKSCQA	239	
✓ 10001	204	CRLRKCYEVGMV K CGSR R RCGYRLVRRQRSADQLHCAGKAKRSGGHAPRVREL-----LLDALSPEQ	267	} DBD
✓ 10002	240	CRLRKCYEVGM M KGGIRKDRRGGF M LKHKRQRDD-----GEGRGEVGSAGDMRAANLWPSPLMIKRSKKNLALSLTADQ	314	
✓ 10001	268	LVLTLLEAEP P PHV L ISR--PSAPFTEASMMMSLT K LADKELVH M ISWAKKIPGFVLSLFDQVR L LESCWMEVLMGLMW	345	} AF-2
✓ 10002	315	MVSALLDAEPP-ILYSEYDPT R PFSEASMMGLLT N LADRELVH M INWAKRVPGFVDLTLHDQVH L LECAWLEILMIGLVW	393	
✓ 10001	346	RSIDHPGKLI F APDLVLRDEGKCV E GILEIFDMLLATTSR F RELK L QHKEYLCVKAMILN S SMYPLVTAT-QDADSSR	424	} AF-2
✓ 10002	394	RSMEHPGKLL F APNLLDRNQGKCV E GMVEIFDMLLATSSR F FRMNLQGE E FVCLKSIILN S GVYTF L SSTLKSLEEKD	473	
✓ 10001	425	KLAHLNNAV T DALV V IAKSGISSQQQSMRLANLMLLSHVRHASNKGMEHL L NMKCKNVV P VYD L LLEMLNAHVLRGCK	504	} AF-2
✓ 10002	474	HIHRVLDKI T DTLIHLMAKAGLT L QQHQRLAQLLLILSHIRHMSNKGMEHLYSMCKCKNVV P LYD L LLEMLDAHRLHAPT	553	
✓ 10001	505	SSITGSECSPAEDSKSKEGSQNPQSQ-----	530	} AF-2
✓ 10002	554	SRGGASVEETDQSHLATAGSTSSHSLQKYYITGEAEGFPATV	595	

Figure 4.11. The protein sequence alignment of full-length hER α and hER β . The protein sequence of hER β was aligned to full-length hER α , and highly conserved DBD and AF-2 domains were observed.

4.4.3 Cadmium binding to the hER α ligand binding domain

Similar to E2, we demonstrated that Cd²⁺ also bound to apo-LBD with 1:1 ratio and a with submicromolar affinity. Cd²⁺ activates hER α as a transcription factor (137), and the chimeric protein of GAL4-DBD/hER α -LBD suggested that Cd²⁺ exerts its functional activation at the LBD. However, no structure-function relationship has been established for the Cd²⁺ complex. We measured the deuterium incorporation rate profiles of the Cd²⁺-LBD complex and compared them to the profiles of apo-LBD and E2-LBD. Several interesting changes were observed that help us understand how Cd²⁺ may activate the LBD of hER α . First, the HDX rate profile for is peptide 526–540 is almost indistinguishable from the E2-bound form. This suggests that the region spanning H11–H12 has a similar structural response to both the endogenous ligand estradiol and the metalloestrogen Cd²⁺. Since E2 binding to apo-LBD causes a transconformation of helix H12, we propose that a similar structural change is occurring in Cd²⁺-LBD. This is highly functionally relevant since H11–H12 are proposed to mediate the conformational response to ligand binding to the rest of the hER α in the full-length construct (125, 145).

Another peptide in Cd²⁺-LBD with similar change as E2-LBD is peptide 429–440, which is the middle section of helix H8 and provides the interface for dimerization (145). The observation could indicate that both E2 and Cd²⁺ can enhance the formation of homodimer because this peptide became more rigid in both E2-LBD and Cd²⁺-LBD.

4.4.4 Localization of the Cd²⁺ binding site within the LBD

The Cd²⁺ binding site and amino acid residues involved in Cd²⁺ binding have been studied with mutagenesis (137) and chemical modifications (151). However, the residues suggested by Stoica *et al* are broadly distributed and the mutants had significantly decreased

binding affinity to E2 (137, 147), which raise the possibility that for some, the protein conformation might be disrupted or altered by the mutations. This is especially true for chemical modification since it affects multiple residues at once by covalent attachment of some chemical moiety. The results from the chemical modification study also disagreed with those from the mutagenesis experiments so we will primarily consider the mutagenesis results in this discussion. Mutagenesis suggested that residues Cys381, Cys447, Asp523, His524 and Glu538 are potential ligands to Cd²⁺. Among them, the peptides contain residues Asp523, His524 or Cys381 are not available for HDX-MS analysis, thus we cannot exclude the possibility that these residues are involved in Cd²⁺ coordination. Interestingly, the peptide contains residue Glu538 (peptide 526–540) demonstrated a decrease in solvent accessibility, but it is more likely that the decreased solvent accessibility was due to the transconformation of helix H12 rather than the coordination of Cd²⁺ by Glu538.

To locate the binding site of Cd²⁺ in the LBD, we utilized the ligand binding prediction program 3DligandSite (167). This prediction for the LBD of hER α was based on the x-ray crystallography structure of rat ER β LBD that contained E2 and Ni²⁺ as ligands, and residues Arg394, His398 and Glu397 are predicted as the Cd²⁺ coordination ligands (**Figure 4.12A**). Side chains from these three amino acids provide a possible coordination environment with N and O as ligands. Noticeably, these three amino acid residues are highly conserved in estrogen receptors for mammals, including ER α and ER β of mouse, rat, cow and human. Thus, it is possible that Cd²⁺ can also bind to hER β in a similar manner. However, hER β has distinct tissue distribution and it regulates the expression of different genes than that of hER α . For example, hER α activates mammary cells proliferation, while hER β triggers apoptosis for cancer cells (125). The highest level of hER α is expressed in reproductive organs, and hER β is expressed in

brain and other tissues (125). As a result, Cd^{2+} binding does not heavily affect the proper function and regulation of $\text{hER}\beta$ as it to $\text{hER}\alpha$ (125). The first drawback to this prediction is that it does not truly take the coordination characteristics of Cd^{2+} ion into account when predicting a binding site. In addition, our HDX–MS experiments observed increased solvent accessibility for peptide 403–410 (beta strands S1/S2), which disagrees with the prediction due to the coordination of metal ions normally causes decreased solvent accessibility and/or dynamics (29, 63).

Another possible Cd^{2+} binding site is between the side chains of residues Cys381 and His547 (**Figure 4.12B**). In this hypothesis, Cd^{2+} is coordinated by the thiolate from residue Cys381 and the imidazole group from His547 with ideal distance. In addition, the coordination of Cd^{2+} will force the helix H12 to seal the estradiol binding cavity, which could explain the non-competitive inhibition of Cd^{2+} to estradiol binding (137). This forced transconformation of helix H12 could create the binding surface for coactivators and stimulate the activity of $\text{hER}\alpha$ as a transcription factor. However, peptides containing residues Cys381 or His547 are not available in our current HDX–MS due to the digestion resistance of $\text{hER}\alpha$ LBD (156). Thus, optimization of HDX–MS and additional experiments are warranted.

Last but not the least, the x-ray crystallography reported by Sigler *et al* provides additional possibility of Cd^{2+} binding site(s) (162). In this structure, Au^+ was added to phase structure for data solving, and these Au^+ ions were coordinated by cysteine residues (**Figure 4.13**). Au^+ is also a soft metal like Cd^{2+} , thus the binding sites of Au^+ may bind Cd^{2+} with unknown binding affinity.

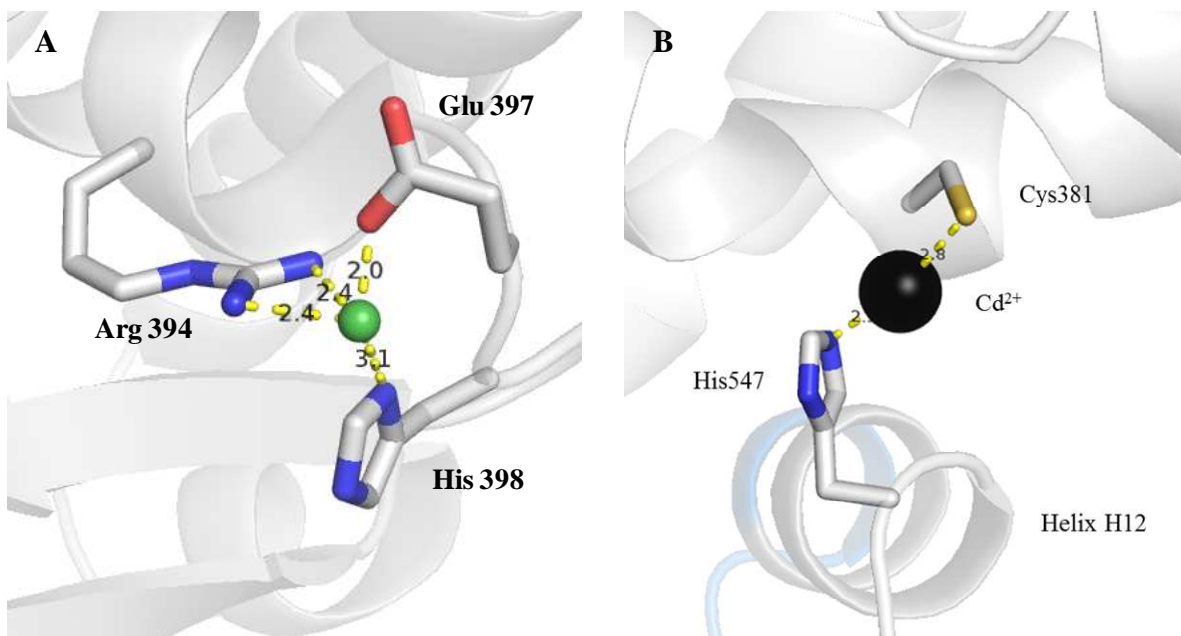


Figure 4.12. The possible binding site(s) of Cd²⁺ in hERα LBD. (A) The binding site predicted based on the structure of rERβ (167, 168), and residues Arg394, Glu397 and His398 are the predicted ligands. (B) The proposed binding site of Cd²⁺, which is coordinated by the thiol group from Cys381 and His547. Cd²⁺ is in black (PDB 1ERE) (145).

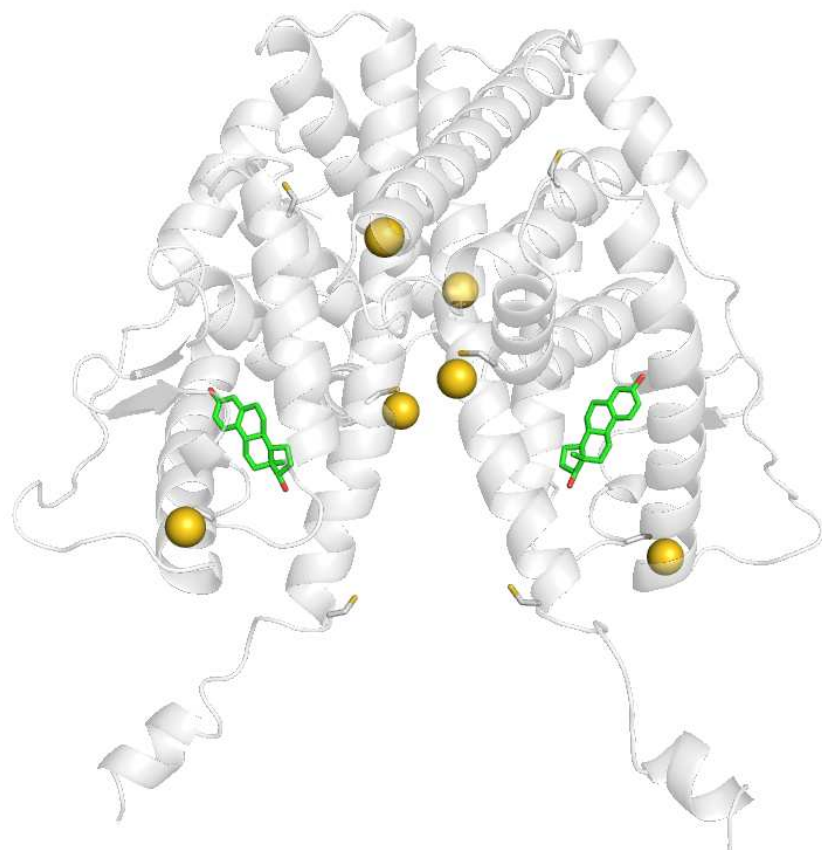


Figure 4.13. The Au⁺ binding sites in hER α LBD. Au⁺ is in gold, and estradiol is in green (PDB 1A52) (162).

Based on current results, we demonstrated that Cd^{2+} bound to hER α LBD and triggered structural changes, some of which were similar to the ones in E2-bound LBD. We suggest there are two most possible binding sites for Cd^{2+} : (1) the site between the helix H6 and strand S1; (2) the site provided by residues Cys381 and His547. Further investigation utilizing UV-visible spectrophotometer and X-ray absorption spectroscopy (XAS) will provide detailed information about the ligand types and coordination geometry, which will give the conclusive answer about the binding site(s) of Cd^{2+} on hER α .

4.5 Future Work

To fully understand the mechanism of Cd^{2+} activating hER α , future studies are going to focus on following directions. (1) To purify full-length hER α with native E2 and DNA binding affinities, the hER α protein will be expressed and purified for *S. pombe* in larger scale. The purified hER α will be analyzed for structural changes upon E2 and Cd^{2+} binding through HDX-MS analysis, and this will reveal the mechanism of hER α activation for the full-length protein. (2) Utilizing XAS and mutagenesis to further test the proposed Cd^{2+} binding amino acid residues. XAS measures the photon energy used to excite the core electrons of interested metals, and we will use it to determine the ligand types and coordination geometry of the Cd^{2+} atom in Cd^{2+} -LBD complex. (3) A coactivator recruitment assay for will be performed for the LBD and full-length hER α with fluorophore-labeled stapled peptides with sequence of XXLXXLLXX. This assay will provide evidence for the capability of Cd^{2+} to activate hER α as a transcription factor. (4) Native gel electrophoresis will be performed for apo-LBD, E2-LBD and Cd^{2+} -LBD to clarify if the LBD dimerization is ligand-dependent. This is important because if Cd^{2+} cannot lead to dimerization then it cannot activate hER α as a transcription factor. (5) If the expression of full-length hER α still results with low concentration protein, the overexpression of AF-1 domain

(residues 1–184), DBD (185–250) and AF-2 (251–595) can be performed and their conformational changes will be analyzed with HDX–MS.

REFERENCES

1. Chowdhury, B. A., and Chandra, R. K. (1987) Biological and health implications of toxic heavy metal and essential trace element interactions, *Prog. Food Nutr. Sci.* 11, 55-113.
2. Chrichton, R. R. (2008) *Biological inorganic chemistry: An introduction*, Elsevier.
3. Hanikenne, M., Merchant, S. S., and Hamel, P. (2009) Transition metal nutrition: A balance between deficiency and toxicity, in *The Chlamydomonas Sourcebook* (Stern, D., Ed.), pp 333–400, San Diego, CA: Academic Press.
4. Ehrensberger, K. M., and Bird, A. J. (2011) Hammering out details: regulating metal levels in eukaryotes, *Trends Biochem. Sci.* 36, 524-531.
5. Jarup, L. (2003) Hazards of heavy metal contamination, *Br. Med. Bull.* 68, 167-182.
6. Hartwig, A. (2013) Cadmium and cancer, *Met. Ions. Life Sci.* 11, 491-507.
7. Maret, W., and Moulis, J. M. (2013) The bioinorganic chemistry of cadmium in the context of its toxicity, *Met. Ions Life Sci.* 11, 1-29.
8. Crichton, R. R., and Pierre, J. L. (2001) Old iron, young copper: from Mars to Venus, *Biometals* 14, 99-112.
9. Aisen, P., Enns, C., and Wessling-Resnick, M. (2001) Chemistry and biology of eukaryotic iron metabolism, *Int. J. Biochem. Cell Biol.* 33, 940-959.
10. Drose, S., and Brandt, U. (2012) Molecular mechanisms of superoxide production by the mitochondrial respiratory chain, *Adv. Exp. Med. Biol.* 748, 145-169.
11. Fridovich, I. (1997) Superoxide anion radical (O₂⁻), superoxide dismutases, and related matters, *J. Biol. Chem.* 272, 18515-18517.
12. Martin, L. J. (2012) Biology of mitochondria in neurodegenerative diseases, *Prog. Mol. Biol. Transl. Sci.* 107, 355-415.
13. Halliwell, B. (2001) Role of free radicals in the neurodegenerative diseases: therapeutic implications for antioxidant treatment, *Drugs Aging* 18, 685-716.

14. Pastor, N., Weinstein, H., Jamison, E., and Brenowitz, M. (2000) A detailed interpretation of OH radical footprints in a TBP-DNA complex reveals the role of dynamics in the mechanism of sequence-specific binding, *J. Mol. Biol.* 304, 55-68.
15. Valko, M., Rhodes, C. J., Moncol, J., Izakovic, M., and Mazur, M. (2006) Free radicals, metals and antioxidants in oxidative stress-induced cancer, *Chem. Biol. Interact.* 160, 1-40.
16. De Domenico, I., McVey Ward, D., and Kaplan, J. (2008) Regulation of iron acquisition and storage: consequences for iron-linked disorders, *Nat. Rev. Mol. Cell Biol.* 9, 72-81.
17. Kaplan, C. D., and Kaplan, J. (2009) Iron acquisition and transcriptional regulation, *Chem. Rev.* 109, 4536-4552.
18. Anderson, C. P., Shen, M., Eisenstein, R. S., and Leibold, E. A. (2012) Mammalian iron metabolism and its control by iron regulatory proteins, *Biochim. Biophys. Acta* 1823, 1468-1483.
19. Pantopoulos, K., Porwal, S. K., Tartakoff, A., and Devireddy, L. (2012) Mechanisms of mammalian iron homeostasis, *Biochemistry* 51, 5705-5724.
20. Labbe, S., Khan, M. G., and Jacques, J. F. (2013) Iron uptake and regulation in *Schizosaccharomyces pombe*, *Curr. Opin. Microbiol.*
21. Schrettl, M., Winkelmann, G., and Haas, H. (2004) Ferrichrome in *Schizosaccharomyces pombe*--an iron transport and iron storage compound, *Biometals* 17, 647-654.
22. Askwith, C., and Kaplan, J. (1997) An oxidase-permease-based iron transport system in *Schizosaccharomyces pombe* and its expression in *Saccharomyces cerevisiae*, *J. Biol. Chem.* 272, 401-405.
23. Labbe, S., Pelletier, B., and Mercier, A. (2007) Iron homeostasis in the fission yeast *Schizosaccharomyces pombe*, *Biometals* 20, 523-537.
24. Pelletier, B., Beaudoin, J., Mukai, Y., and Labbe, S. (2002) Fep1, an iron sensor regulating iron transporter gene expression in *Schizosaccharomyces pombe*, *J. Biol. Chem.* 277, 22950-22958.
25. Huang, M. L., Lane, D. J., and Richardson, D. R. (2011) Mitochondrial mayhem: the mitochondrion as a modulator of iron metabolism and its role in disease, *Antioxid. Redox Signal* 15, 3003-3019.
26. Lill, R., Hoffmann, B., Molik, S., Pierik, A. J., Rietzschel, N., Stehling, O., Uzarska, M. A., Webert, H., Wilbrecht, C., and Muhlenhoff, U. (2012) The role of mitochondria in cellular iron-sulfur protein biogenesis and iron metabolism, *Biochim. Biophys. Acta* 1823, 1491-1508.

27. Schrettl, M., and Haas, H. (2011) Iron homeostasis--Achilles' heel of *Aspergillus fumigatus*?, *Curr. Opin. Microbiol.* *14*, 400-405.
28. Hamza, I., and Dailey, H. A. (2012) One ring to rule them all: trafficking of heme and heme synthesis intermediates in the metazoans, *Biochim. Biophys. Acta* *1823*, 1617-1632.
29. Asuru, A. P., and Busenlehner, L. S. (2011) Analysis of human ferrochelatase iron binding via amide hydrogen/deuterium exchange mass spectrometry, *Intl. J. Mass Spectrom.* *302*, 76-84.
30. Asuru, A. P., An, M., and Busenlehner, L. S. (2012) Dissection of porphyrin-induced conformational dynamics in the heme biosynthesis enzyme ferrochelatase, *Biochemistry* *51*, 7116-7127.
31. Yoon, T., and Cowan, J. A. (2004) Frataxin-mediated iron delivery to ferrochelatase in the final step of heme biosynthesis, *J. Biol. Chem.* *279*, 25943-25946.
32. Lill, R., and Muhlenhoff, U. (2006) Iron-sulfur protein biogenesis in eukaryotes: components and mechanisms, *Annu. Rev. Cell. Dev. Biol.* *22*, 457-486.
33. Sheftel, A. D., Mason, A. B., and Ponka, P. (2011) The long history of iron in the Universe and in health and disease, *Biochim Biophys Acta* *1820*, 161-187.
34. Lill, R. (2009) Function and biogenesis of iron-sulphur proteins, *Nature* *460*, 831-838.
35. Lill, R., and Muhlenhoff, U. (2008) Maturation of iron-sulfur proteins in eukaryotes: mechanisms, connected processes, and diseases, *Annu. Rev. Biochem.* *77*, 669-700.
36. Johnson, D. C., Dean, D. R., Smith, A. D., and Johnson, M. K. (2005) Structure, function, and formation of biological iron-sulfur clusters, *Annu. Rev. Biochem.* *74*, 247-281.
37. Balk, J., and Pilon, M. (2011) Ancient and essential: the assembly of iron-sulfur clusters in plants, *Trends Plant Sci.* *16*, 218-226.
38. Busi, M. V., and Gomez-Casati, D. F. (2012) Exploring frataxin function, *IUBMB Life* *64*, 56-63.
39. Pierik, A. J., Netz, D. J., and Lill, R. (2009) Analysis of iron-sulfur protein maturation in eukaryotes, *Nat. Protoc.* *4*, 753-766.
40. Frazzon, J., and Dean, D. R. (2001) Feedback regulation of iron-sulfur cluster biosynthesis, *Proc. Natl. Acad. Sci. USA* *98*, 14751-14753.
41. Schwartz, C. J., Giel, J. L., Patschkowski, T., Luther, C., Ruzicka, F. J., Beinert, H., and Kiley, P. J. (2001) IscR, an Fe-S cluster-containing transcription factor, represses

- expression of *Escherichia coli* genes encoding Fe-S cluster assembly proteins, *Proc. Natl. Acad. Sci. USA* 98, 14895-14900.
42. Li, J., Kogan, M., Knight, S. A., Pain, D., and Dancis, A. (1999) Yeast mitochondrial protein, Nfs1p, coordinately regulates iron-sulfur cluster proteins, cellular iron uptake, and iron distribution, *J. Biol. Chem.* 274, 33025-33034.
 43. Rouault, T. A., and Tong, W. H. (2008) Iron-sulfur cluster biogenesis and human disease, *Trends Genet.* 24, 398-407.
 44. Sheftel, A., Stehling, O., and Lill, R. (2010) Iron-sulfur proteins in health and disease, *Trends Endocrinol. Metab.* 21, 302-314.
 45. Rotig, A., de Lonlay, P., Chretien, D., Foury, F., Koenig, M., Sidi, D., Munnich, A., and Rustin, P. (1997) Aconitase and mitochondrial iron-sulphur protein deficiency in Friedreich ataxia, *Nat. Genet.* 17, 215-217.
 46. RA, P., TD, B., and CR, D., (Eds.) (1998) *Friedreich Ataxia*, Seattle (WA).
 47. Marmolino, D. (2011) Friedreich's ataxia: past, present and future, *Brain Res. Rev.* 67, 311-330.
 48. Campuzano, V., Montermini, L., Molto, M. D., Pianese, L., Cossee, M., Cavalcanti, F., Monros, E., Rodius, F., Duclos, F., Monticelli, A., Zara, F., Canizares, J., Koutnikova, H., Bidichandani, S. I., Gellera, C., Brice, A., Trouillas, P., De Michele, G., Filla, A., De Frutos, R., Palau, F., Patel, P. I., Di Donato, S., Mandel, J. L., Coccozza, S., Koenig, M., and Pandolfo, M. (1996) Friedreich's ataxia: autosomal recessive disease caused by an intronic GAA triplet repeat expansion, *Science* 271, 1423-1427.
 49. Cossee, M., Puccio, H., Gansmuller, A., Koutnikova, H., Dierich, A., LeMeur, M., Fischbeck, K., Dolle, P., and Koenig, M. (2000) Inactivation of the Friedreich ataxia mouse gene leads to early embryonic lethality without iron accumulation, *Hum. Mol. Genet.* 9, 1219-1226.
 50. Koutnikova, H., Campuzano, V., and Koenig, M. (1998) Maturation of wild-type and mutated frataxin by the mitochondrial processing peptidase, *Hum. Mol. Genet.* 7, 1485-1489.
 51. Condo, I., Ventura, N., Malisan, F., Rufini, A., Tomassini, B., and Testi, R. (2007) In vivo maturation of human frataxin, *Hum. Mol. Genet.* 16, 1534-1540.
 52. Schmucker, S., Argentini, M., Carelle-Calmels, N., Martelli, A., and Puccio, H. (2008) The in vivo mitochondrial two-step maturation of human frataxin, *Hum. Mol. Genet.* 17, 3521-3531.

53. Gakh, O., Bedekovics, T., Duncan, S. F., Smith, D. Y. t., Berkholtz, D. S., and Isaya, G. (2010) Normal and Friedreich ataxia cells express different isoforms of frataxin with complementary roles in iron-sulfur cluster assembly, *J. Biol. Chem.* 285, 38486-38501.
54. Pastore, A., and Puccio, H. (2013) Frataxin: a protein in search for a function, *J. Neurochem.* 126 Suppl. 1, 43-52.
55. Dhe-Paganon, S., Shigeta, R., Chi, Y. I., Ristow, M., and Shoelson, S. E. (2000) Crystal structure of human frataxin, *J. Biol. Chem.* 275, 30753-30756.
56. He, Y., Alam, S. L., Proteasa, S. V., Zhang, Y., Lesuisse, E., Dancis, A., and Stemmler, T. L. (2004) Yeast frataxin solution structure, iron binding, and ferrochelatase interaction, *Biochemistry* 43, 16254-16262.
57. Cook, J. D., Bencze, K. Z., Jankovic, A. D., Crater, A. K., Busch, C. N., Bradley, P. B., Stemmler, A. J., Spaller, M. R., and Stemmler, T. L. (2006) Monomeric yeast frataxin is an iron-binding protein, *Biochemistry* 45, 7767-7777.
58. Cook, J. D., Kondapalli, K. C., Rawat, S., Childs, W. C., Murugesan, Y., Dancis, A., and Stemmler, T. L. (2010) Molecular details of the yeast frataxin-Isu1 interaction during mitochondrial Fe-S cluster assembly, *Biochemistry* 49, 8756-8765.
59. Gakh, O., Smith, D. Y. t., and Isaya, G. (2008) Assembly of the iron-binding protein frataxin in *Saccharomyces cerevisiae* responds to dynamic changes in mitochondrial iron influx and stress level, *J. Biol. Chem.* 283, 31500-31510.
60. Aloria, K., Schilke, B., Andrew, A., and Craig, E. A. (2004) Iron-induced oligomerization of yeast frataxin homologue Yfh1 is dispensable in vivo, *EMBO Rep.* 5, 1096-1101.
61. Arnold, K., Bordoli, L., Kopp, J., and Schwede, T. (2006) The SWISS-MODEL workspace: a web-based environment for protein structure homology modelling, *Bioinformatics* 22, 195-201.
62. Vaubel, R. A., and Isaya, G. (2013) Iron-sulfur cluster synthesis, iron homeostasis and oxidative stress in Friedreich ataxia, *Mol. Cell Neurosci.* 55, 50-61.
63. Gentry, L. E., Thacker, M. A., Doughty, R., Timkovich, R., and Busenlehner, L. S. (2013) His86 from the N-Terminus of Frataxin Coordinates Iron and Is Required for Fe-S Cluster Synthesis, *Biochemistry*.
64. Babcock, M., de Silva, D., Oaks, R., Davis-Kaplan, S., Jiralerspong, S., Montermini, L., Pandolfo, M., and Kaplan, J. (1997) Regulation of mitochondrial iron accumulation by Yfh1p, a putative homolog of frataxin, *Science* 276, 1709-1712.

65. Foury, F., and Cazzalini, O. (1997) Deletion of the yeast homologue of the human gene associated with Friedreich's ataxia elicits iron accumulation in mitochondria, *FEBS Lett.* 411, 373-377.
66. Puccio, H., Simon, D., Cossee, M., Criqui-Filipe, P., Tiziano, F., Melki, J., Hindelang, C., Matyas, R., Rustin, P., and Koenig, M. (2001) Mouse models for Friedreich ataxia exhibit cardiomyopathy, sensory nerve defect and Fe-S enzyme deficiency followed by intramitochondrial iron deposits, *Nat. Genet.* 27, 181-186.
67. Santos, M. M., Ohshima, K., and Pandolfo, M. (2001) Frataxin deficiency enhances apoptosis in cells differentiating into neuroectoderm, *Hum. Mol. Genet.* 10, 1935-1944.
68. Miranda, C. J., Santos, M. M., Ohshima, K., Smith, J., Li, L., Bunting, M., Cossee, M., Koenig, M., Sequeiros, J., Kaplan, J., and Pandolfo, M. (2002) Frataxin knockin mouse, *FEBS Lett.* 512, 291-297.
69. Anderson, P. R., Kirby, K., Hilliker, A. J., and Phillips, J. P. (2005) RNAi-mediated suppression of the mitochondrial iron chaperone, frataxin, in *Drosophila*, *Hum. Mol. Genet.* 14, 3397-3405.
70. Al-Mahdawi, S., Pinto, R. M., Varshney, D., Lawrence, L., Lowrie, M. B., Hughes, S., Webster, Z., Blake, J., Cooper, J. M., King, R., and Pook, M. A. (2006) GAA repeat expansion mutation mouse models of Friedreich ataxia exhibit oxidative stress leading to progressive neuronal and cardiac pathology, *Genomics* 88, 580-590.
71. Vazquez-Manrique, R. P., Gonzalez-Cabo, P., Ros, S., Aziz, H., Baylis, H. A., and Palau, F. (2006) Reduction of *Caenorhabditis elegans* frataxin increases sensitivity to oxidative stress, reduces lifespan, and causes lethality in a mitochondrial complex II mutant, *FASEB J.* 20, 172-174.
72. Ventura, N., Rea, S. L., Handerson, S. T., Condo, I., Testi, R., and Johnson, T. E. (2006) *C. elegans* as a model for Friedreich Ataxia, *FASEB J.* 20, 1029-1030.
73. Llorens, J. V., Navarro, J. A., Martinez-Sebastian, M. J., Baylies, M. K., Schneuwly, S., Botella, J. A., and Molto, M. D. (2007) Causative role of oxidative stress in a *Drosophila* model of Friedreich ataxia, *FASEB J.* 21, 333-344.
74. Zarse, K., Schulz, T. J., Birringer, M., and Ristow, M. (2007) Impaired respiration is positively correlated with decreased life span in *Caenorhabditis elegans* models of Friedreich Ataxia, *FASEB J.* 21, 1271-1275.
75. Calmels, N., Schmucker, S., Wattenhofer-Donze, M., Martelli, A., Vaucamps, N., Reutenauer, L., Messaddeq, N., Bouton, C., Koenig, M., and Puccio, H. (2009) The first cellular models based on frataxin missense mutations that reproduce spontaneously the defects associated with Friedreich ataxia, *PLoS One* 4, e6379.

76. Ku, S., Soragni, E., Campau, E., Thomas, E. A., Altun, G., Laurent, L. C., Loring, J. F., Napierala, M., and Gottesfeld, J. M. (2010) Friedreich's ataxia induced pluripotent stem cells model intergenerational GAATTC triplet repeat instability, *Cell. Stem Cell* 7, 631-637.
77. Gerber, J., Muhlenhoff, U., and Lill, R. (2003) An interaction between frataxin and Isu1/Nfs1 that is crucial for Fe/S cluster synthesis on Isu1, *EMBO Rep.* 4, 906-911.
78. Tsai, C. L., and Barondeau, D. P. (2010) Human frataxin is an allosteric switch that activates the Fe-S cluster biosynthetic complex, *Biochemistry* 49, 9132-9139.
79. Bulteau, A. L., O'Neill, H. A., Kennedy, M. C., Ikeda-Saito, M., Isaya, G., and Szwed, L. I. (2004) Frataxin acts as an iron chaperone protein to modulate mitochondrial aconitase activity, *Science* 305, 242-245.
80. Gonzalez-Cabo, P., Vazquez-Manrique, R. P., Garcia-Gimeno, M. A., Sanz, P., and Palau, F. (2005) Frataxin interacts functionally with mitochondrial electron transport chain proteins, *Hum. Mol. Genet.* 14, 2091-2098.
81. Gakh, O., Adamec, J., Gacy, A. M., Twosten, R. D., Owen, W. G., and Isaya, G. (2002) Physical evidence that yeast frataxin is an iron storage protein, *Biochemistry* 41, 6798-6804.
82. Pook, M. A., Al-Mahdawi, S., Carroll, C. J., Cossee, M., Puccio, H., Lawrence, L., Clark, P., Lowrie, M. B., Bradley, J. L., Cooper, J. M., Koenig, M., and Chamberlain, S. (2001) Rescue of the Friedreich's ataxia knockout mouse by human YAC transgenesis, *Neurogenetics* 3, 185-193.
83. Miranda, C. J., Santos, M. M., Ohshima, K., Tessaro, M., Sequeiros, J., and Pandolfo, M. (2004) Frataxin overexpressing mice, *FEBS Lett.* 572, 281-288.
84. Runko, A. P., Griswold, A. J., and Min, K. T. (2008) Overexpression of frataxin in the mitochondria increases resistance to oxidative stress and extends lifespan in *Drosophila*, *FEBS Lett.* 582, 715-719.
85. Seguin, A., Bayot, A., Dancis, A., Rogowska-Wrzesinska, A., Auchere, F., Camadro, J. M., Bulteau, A. L., and Lesuisse, E. (2009) Overexpression of the yeast frataxin homolog (Yfh1): contrasting effects on iron-sulfur cluster assembly, heme synthesis and resistance to oxidative stress, *Mitochondrion* 9, 130-138.
86. Navarro, J. A., Llorens, J. V., Soriano, S., Botella, J. A., Schneuwly, S., Martinez-Sebastian, M. J., and Molto, M. D. (2011) Overexpression of human and fly frataxins in *Drosophila* provokes deleterious effects at biochemical, physiological and developmental levels, *PLoS One* 6, e21017.

87. Ristow, M., Pfister, M. F., Yee, A. J., Schubert, M., Michael, L., Zhang, C. Y., Ueki, K., Michael, M. D., 2nd, Lowell, B. B., and Kahn, C. R. (2000) Frataxin activates mitochondrial energy conversion and oxidative phosphorylation, *Proc. Natl. Acad. Sci. USA* 97, 12239-12243.
88. Schulz, T. J., Thierbach, R., Voigt, A., Drewes, G., Mietzner, B., Steinberg, P., Pfeiffer, A. F., and Ristow, M. (2006) Induction of oxidative metabolism by mitochondrial frataxin inhibits cancer growth: Otto Warburg revisited, *J. Biol. Chem.* 281, 977-981.
89. Rhind, N., Chen, Z., Yassour, M., Thompson, D. A., Haas, B. J., Habib, N., Wapinski, I., Roy, S., Lin, M. F., Heiman, D. I., Young, S. K., Furuya, K., Guo, Y., Pidoux, A., Chen, H. M., Robbertse, B., Goldberg, J. M., Aoki, K., Bayne, E. H., Berlin, A. M., Desjardins, C. A., Dobbs, E., Dukaj, L., Fan, L., FitzGerald, M. G., French, C., Gujja, S., Hansen, K., Keifenheim, D., Levin, J. Z., Mosher, R. A., Muller, C. A., Pfiffner, J., Priest, M., Russ, C., Smialowska, A., Swoboda, P., Sykes, S. M., Vaughn, M., Vengrova, S., Yoder, R., Zeng, Q., Allshire, R., Baulcombe, D., Birren, B. W., Brown, W., Ekwall, K., Kellis, M., Leatherwood, J., Levin, H., Margalit, H., Martienssen, R., Nieduszynski, C. A., Spatafora, J. W., Friedman, N., Dalgaard, J. Z., Baumann, P., Niki, H., Regev, A., and Nusbaum, C. (2011) Comparative functional genomics of the fission yeasts, *Science* 332, 930-936.
90. Wu, S. P., Wu, G., Surerus, K. K., and Cowan, J. A. (2002) Iron-sulfur cluster biosynthesis. Kinetic analysis of [2Fe-2S] cluster transfer from holo ISU to apo Fd: role of redox chemistry and a conserved aspartate, *Biochemistry* 41, 8876-8885.
91. Maundrell, K. (1993) Thiamine-repressible expression vectors pREP and pRIP for fission yeast, *Gene* 123, 127-130.
92. C. Alfa, P. Fantès, J. Hyams, M. McLeod, and Warbrick, E. (1993) *Experiments with Fission Yeast: A Laboratory Course Manual*, Cold Spring Harbor Laboratory Press, NY.
93. Forsburg, S. L. (1993) Comparison of *Schizosaccharomyces pombe* expression systems, *Nucleic Acids Res.* 21, 2955-2956.
94. Javerzat, J. P., Cranston, G., and Allshire, R. C. (1996) Fission yeast genes which disrupt mitotic chromosome segregation when overexpressed, *Nucleic Acids Res.* 24, 4676-4683.
95. Wang, Y., Gulis, G., Buckner, S., Johnson, P. C., Sullivan, D., Busenlehner, L., and Marcus, S. (2010) The MAP kinase Pmk1 and protein kinase A are required for rotenone resistance in the fission yeast, *Schizosaccharomyces pombe*, *Biochem. Biophys. Res. Commun.* 399, 123-128.
96. Chen, D., Toone, W. M., Mata, J., Lyne, R., Burns, G., Kivinen, K., Brazma, A., Jones, N., and Bahler, J. (2003) Global transcriptional responses of fission yeast to environmental stress, *Mol. Biol. Cell* 14, 214-229.

97. Livak, K. J., and Schmittgen, T. D. (2001) Analysis of relative gene expression data using real-time quantitative PCR and the 2(-Delta Delta C(T)) Method, *Methods* 25, 402-408.
98. Chiron, S., Gaisne, M., Guillou, E., Belenguer, P., Clark-Walker, G. D., and Bonnefoy, N. (2007) Studying mitochondria in an attractive model: *Schizosaccharomyces pombe*, *Methods Mol. Biol.* 372, 91-105.
99. Tamarit, J., Irazusta, V., Moreno-Cermeno, A., and Ros, J. (2006) Colorimetric assay for the quantitation of iron in yeast, *Anal. Biochem.* 351, 149-151.
100. Ackrell, B. A., Kearney, E. B., and Singer, T. P. (1978) Mammalian succinate dehydrogenase, *Methods Enzymol.* 53, 466-483.
101. Claros, M. G., and Vincens, P. (1996) Computational method to predict mitochondrially imported proteins and their targeting sequences, *Eur. J. Biochem.* 241, 779-786.
102. Roman, D. G., Dancis, A., Anderson, G. J., and Klausner, R. D. (1993) The fission yeast ferric reductase gene *frp1+* is required for ferric iron uptake and encodes a protein that is homologous to the gp91-phox subunit of the human NADPH phagocyte oxidoreductase, *Mol. Cell. Biol.* 13, 4342-4350.
103. Gardner, P. R. (2002) Aconitase: sensitive target and measure of superoxide, *Methods Enzymol.* 349, 9-23.
104. Hederstedt, L., and Rutberg, L. (1981) Succinate dehydrogenase--a comparative review, *Microbiol Rev.* 45, 542-555.
105. Gille, G., and Reichmann, H. (2011) Iron-dependent functions of mitochondria--relation to neurodegeneration, *J. Neural. Transm.* 118, 349-359.
106. Shoichet, S. A., Baumer, A. T., Stamenkovic, D., Sauer, H., Pfeiffer, A. F., Kahn, C. R., Muller-Wieland, D., Richter, C., and Ristow, M. (2002) Frataxin promotes antioxidant defense in a thiol-dependent manner resulting in diminished malignant transformation in vitro, *Hum. Mol. Genet.* 11, 815-821.
107. Zuin, A., Gabrielli, N., Calvo, I. A., Garcia-Santamarina, S., Hoe, K. L., Kim, D. U., Park, H. O., Hayles, J., Ayte, J., and Hidalgo, E. (2008) Mitochondrial dysfunction increases oxidative stress and decreases chronological life span in fission yeast, *PLoS One* 3, e2842.
108. Trester-Zedlitz, M., Kamada, K., Burley, S. K., Fenyo, D., Chait, B. T., and Muir, T. W. (2003) A modular cross-linking approach for exploring protein interactions, *J. Am. Chem. Soc.* 125, 2416-2425.

109. Sun, W., Wang, Z., Jiang, H., Zhang, J., Bahler, J., Chen, D., and Murchie, A. I. (2010) A novel function of the mitochondrial transcription factor Mtf1 in fission yeast; Mtf1 regulates the nuclear transcription of *srk1*, *Nucleic Acids Res.* 39, 2690-2700.
110. Wu, P., Zhao, R., Ye, Y., and Wu, J. Q. (2011) Roles of the DYRK kinase Pom2 in cytokinesis, mitochondrial morphology, and sporulation in fission yeast, *PLoS One* 6, e28000.
111. Starkov, A. A. (2008) The role of mitochondria in reactive oxygen species metabolism and signaling, *Ann. N. Y. Acad. Sci.* 1147, 37-52.
112. Herrero, E., Ros, J., Belli, G., and Cabisco, E. (2008) Redox control and oxidative stress in yeast cells, *Biochim. Biophys. Acta* 1780, 1217-1235.
113. Fridovich, I. (1995) Superoxide radical and superoxide dismutases, *Annu. Rev. Biochem.* 64, 97-112.
114. Schmucker, S., Martelli, A., Colin, F., Page, A., Wattenhofer-Donze, M., Reutenauer, L., and Puccio, H. (2011) Mammalian frataxin: an essential function for cellular viability through an interaction with a preformed ISCU/NFS1/ISD11 iron-sulfur assembly complex, *PLoS One* 6, e16199.
115. Lindahl, P. A., and Holmes-Hampton, G. P. (2011) Biophysical probes of iron metabolism in cells and organelles, *Curr. Opin. Chem. Biol.* 15, 342-346.
116. Wilson, R. B. (2012) Therapeutic developments in Friedreich ataxia, *J. Child Neurol.* 27, 1212-1216.
117. Blindauer, C. A., and Schmid, R. (2010) Cytosolic metal handling in plants: determinants for zinc specificity in metal transporters and metallothioneins, *Metallomics* 2, 510-529.
118. Sovago, I., and Varnagy, K. (2013) Cadmium(II) complexes of amino acids and peptides, *Met. Ions Life Sci.* 11, 275-302.
119. Zangger, K., Oz, G., Otvos, J. D., and Armitage, I. M. (1999) Three-dimensional solution structure of mouse [Cd7]-metallothionein-1 by homonuclear and heteronuclear NMR spectroscopy, *Protein Sci.* 8, 2630-2638.
120. Perrin, D. D., and Watt, A. E. (1971) Complex formation of zinc and cadmium with glutathione, *Biochim. Biophys. Acta* 230, 96-104.
121. Reuter, S., Gupta, S. C., Chaturvedi, M. M., and Aggarwal, B. B. (2010) Oxidative stress, inflammation, and cancer: how are they linked?, *Free Radic. Biol. Med.* 49, 1603-1616.
122. Kumar, R., and Thompson, E. B. (1999) The structure of the nuclear hormone receptors, *Steroids* 64, 310-319.

123. Maret, W. (2013) Zinc biochemistry: from a single zinc enzyme to a key element of life, *Adv. Nutr.* 4, 82-91.
124. Byrne, C., Divekar, S. D., Storchan, G. B., Parodi, D. A., and Martin, M. B. (2013) Metals and breast cancer, *J. Mammary Gland Biol. Neoplasia.* 18, 63-73.
125. Ascenzi, P., Bocedi, A., and Marino, M. (2006) Structure-function relationship of estrogen receptor alpha and beta: impact on human health, *Mol. Aspects. Med.* 27, 299-402.
126. Sorlie, T., Perou, C. M., Tibshirani, R., Aas, T., Geisler, S., Johnsen, H., Hastie, T., Eisen, M. B., van de Rijn, M., Jeffrey, S. S., Thorsen, T., Quist, H., Matese, J. C., Brown, P. O., Botstein, D., Lonning, P. E., and Borresen-Dale, A. L. (2001) Gene expression patterns of breast carcinomas distinguish tumor subclasses with clinical implications, *Proc. Natl. Acad. Sci. USA* 98, 10869-10874.
127. Perou, C. M., Sorlie, T., Eisen, M. B., van de Rijn, M., Jeffrey, S. S., Rees, C. A., Pollack, J. R., Ross, D. T., Johnsen, H., Akslen, L. A., Fluge, O., Pergamenschikov, A., Williams, C., Zhu, S. X., Lonning, P. E., Borresen-Dale, A. L., Brown, P. O., and Botstein, D. (2000) Molecular portraits of human breast tumours, *Nature* 406, 747-752.
128. Garcia-Morales, P., Saceda, M., Kenney, N., Kim, N., Salomon, D. S., Gottardis, M. M., Solomon, H. B., Sholler, P. F., Jordan, V. C., and Martin, M. B. (1994) Effect of cadmium on estrogen receptor levels and estrogen-induced responses in human breast cancer cells, *J. Biol. Chem.* 269, 16896-16901.
129. Antila, E., Mussalo-Rauhamaa, H., Kantola, M., Atroshi, F., and Westermarck, T. (1996) Association of cadmium with human breast cancer, *Sci. Total Environ.* 186, 251-256.
130. McElroy, J. A., Shafer, M. M., Trentham-Dietz, A., Hampton, J. M., and Newcomb, P. A. (2006) Cadmium exposure and breast cancer risk, *J. Natl. Cancer Inst* 98, 869-873.
131. Akesson, A., Julin, B., and Wolk, A. (2008) Long-term dietary cadmium intake and postmenopausal endometrial cancer incidence: a population-based prospective cohort study, *Cancer Res.* 68, 6435-6441.
132. Lubovac-Pilav, Z., Borrás, D. M., Ponce, E., and Louie, M. C. (2014) Using expression profiling to understand the effects of chronic cadmium exposure on mcf-7 breast cancer cells, *PLoS One* 8, e84646.
133. Johnson, M. D., Kenney, N., Stoica, A., Hilakivi-Clarke, L., Singh, B., Chepko, G., Clarke, R., Sholler, P. F., Lirio, A. A., Foss, C., Reiter, R., Trock, B., Paik, S., and Martin, M. B. (2003) Cadmium mimics the in vivo effects of estrogen in the uterus and mammary gland, *Nat. Med.* 9, 1081-1084.

134. Alonso-Gonzalez, C., Gonzalez, A., Mazarrasa, O., Guezmes, A., Sanchez-Mateos, S., Martinez-Campa, C., Cos, S., Sanchez-Barcelo, E. J., and Mediavilla, M. D. (2007) Melatonin prevents the estrogenic effects of sub-chronic administration of cadmium on mice mammary glands and uterus, *J. Pineal. Res.* 42, 403-410.
135. Hofer, N., Diel, P., Wittsiepe, J., Wilhelm, M., and Degen, G. H. (2009) Dose- and route-dependent hormonal activity of the metalloestrogen cadmium in the rat uterus, *Toxicol. Lett.* 191, 123-131.
136. Ali, I., Penttinen-Damdimopoulou, P. E., Makela, S. I., Berglund, M., Stenius, U., Akesson, A., Hakansson, H., and Halldin, K. (2010) Estrogen-like effects of cadmium in vivo do not appear to be mediated via the classical estrogen receptor transcriptional pathway, *Environ. Health Perspect.* 118, 1389-1394.
137. Stoica, A., Katzenellenbogen, B. S., and Martin, M. B. (2000) Activation of estrogen receptor-alpha by the heavy metal cadmium, *Mol. Endocrinol.* 14, 545-553.
138. Gosden, J. R., Middleton, P. G., and Rout, D. (1986) Localization of the human oestrogen receptor gene to chromosome 6q24---q27 by in situ hybridization, *Cytogenet. Cell Genet.* 43, 218-220.
139. Walter, P., Green, S., Greene, G., Krust, A., Bornert, J. M., Jeltsch, J. M., Staub, A., Jensen, E., Scrace, G., Waterfield, M., and et al. (1985) Cloning of the human estrogen receptor cDNA, *Proc. Natl. Acad. Sci. USA* 82, 7889-7893.
140. McInerney, E. M., and Katzenellenbogen, B. S. (1996) Different regions in activation function-1 of the human estrogen receptor required for antiestrogen- and estradiol-dependent transcription activation, *J. Biol. Chem.* 271, 24172-24178.
141. Schwabe, J. W., Chapman, L., Finch, J. T., and Rhodes, D. (1993) The crystal structure of the estrogen receptor DNA-binding domain bound to DNA: how receptors discriminate between their response elements, *Cell* 75, 567-578.
142. Schwabe, J. W., Chapman, L., Finch, J. T., Rhodes, D., and Neuhaus, D. (1993) DNA recognition by the oestrogen receptor: from solution to the crystal, *Structure* 1, 187-204.
143. Schwabe, J. W., Fairall, L., Chapman, L., Finch, J. T., Dutnall, R. N., and Rhodes, D. (1993) The cocrystal structures of two zinc-stabilized DNA-binding domains illustrate different ways of achieving sequence-specific DNA recognition, *Cold Spring Harb. Symp. Quant. Biol.* 58, 141-147.
144. Webster, N. J., Green, S., Jin, J. R., and Chambon, P. (1988) The hormone-binding domains of the estrogen and glucocorticoid receptors contain an inducible transcription activation function, *Cell* 54, 199-207.

145. Brzozowski, A. M., Pike, A. C., Dauter, Z., Hubbard, R. E., Bonn, T., Engstrom, O., Ohman, L., Greene, G. L., Gustafsson, J. A., and Carlquist, M. (1997) Molecular basis of agonism and antagonism in the oestrogen receptor, *Nature* 389, 753-758.
146. Warnmark, A., Treuter, E., Gustafsson, J. A., Hubbard, R. E., Brzozowski, A. M., and Pike, A. C. (2002) Interaction of transcriptional intermediary factor 2 nuclear receptor box peptides with the coactivator binding site of estrogen receptor alpha, *J. Biol. Chem.* 277, 21862-21868.
147. Reese, J. C., and Katzenellenbogen, B. S. (1991) Mutagenesis of cysteines in the hormone binding domain of the human estrogen receptor. Alterations in binding and transcriptional activation by covalently and reversibly attaching ligands, *J. Biol. Chem.* 266, 10880-10887.
148. Wrenn, C. K., and Katzenellenbogen, B. S. (1993) Structure-function analysis of the hormone binding domain of the human estrogen receptor by region-specific mutagenesis and phenotypic screening in yeast, *J. Biol. Chem.* 268, 24089-24098.
149. Predki, P. F., and Sarkar, B. (1992) Effect of replacement of "zinc finger" zinc on estrogen receptor DNA interactions, *J. Biol. Chem.* 267, 5842-5846.
150. Deegan, B. J., Bona, A. M., Bhat, V., Mikles, D. C., McDonald, C. B., Seldeen, K. L., and Farooq, A. (2011) Structural and thermodynamic consequences of the replacement of zinc with environmental metals on estrogen receptor alpha-DNA interactions, *J. Mol. Recognit.* 24, 1007-1017.
151. Nesatyy, V. J., Rutishauser, B. V., Eggen, R. I., and Suter, M. J. (2005) Identification of the estrogen receptor Cd-binding sites by chemical modification, *Analyst.* 130, 1087-1097.
152. Mossakowska, D. E. (1998) Expression of nuclear hormone receptors in Escherichia coli, *Curr. Opin. Biotechnol.* 9, 502-505.
153. Srinivasan, G. (1992) Overexpression of receptors of the steroid/thyroid family, *Mol. Endocrinol.* 6, 857-860.
154. Maity, H., Lim, W. K., Rumbley, J. N., and Englander, S. W. (2003) Protein hydrogen exchange mechanism: local fluctuations, *Protein Sci.* 12, 153-160.
155. Ling, J. M., Silva, L., Schriemer, D. C., and Schryvers, A. B. (2012) Hydrogen-deuterium exchange coupled to mass spectrometry to investigate ligand-receptor interactions, *Methods Mol. Biol.* 799, 237-252.
156. Dai, S. Y., Chalmers, M. J., Bruning, J., Bramlett, K. S., Osborne, H. E., Montrose-Rafizadeh, C., Barr, R. J., Wang, Y., Wang, M., Burris, T. P., Dodge, J. A., and Griffin,

- P. R. (2008) Prediction of the tissue-specificity of selective estrogen receptor modulators by using a single biochemical method, *Proc. Natl. Acad. Sci. USA* 105, 7171-7176.
157. Riddles, P. W., Blakeley, R. L., and Zerner, B. (1983) Reassessment of Ellman's reagent, *Methods Enzymol.* 91, 49-60.
158. Busenlehner, L. S., and Armstrong, R. N. (2005) Insights into enzyme structure and dynamics elucidated by amide H/D exchange mass spectrometry, *Arch. Biochem. Biophys.* 433, 34-46.
159. Bolli, A., and Marino, M. (2011) Current and future development of estrogen receptor ligands: applications in estrogen-related cancers, *Recent Pat. Endocr. Metab. Immune. Drug Discov.* 5, 210-229.
160. Batista, M. R., and Martinez, L. (2013) Dynamics of nuclear receptor Helix-12 switch of transcription activation by modeling time-resolved fluorescence anisotropy decays, *Biophys. J.* 105, 1670-1680.
161. Hegy, G. B., Shackleton, C. H., Carlquist, M., Bonn, T., Engstrom, O., Sjöholm, P., and Witkowska, H. E. (1996) Carboxymethylation of the human estrogen receptor ligand-binding domain-estradiol complex: HPLC/ESMS peptide mapping shows that cysteine 447 does not react with iodoacetic acid, *Steroids* 61, 367-373.
162. Tanenbaum, D. M., Wang, Y., Williams, S. P., and Sigler, P. B. (1998) Crystallographic comparison of the estrogen and progesterone receptor's ligand binding domains, *Proc. Natl. Acad. Sci. USA* 95, 5998-6003.
163. Bourguet, W., Ruff, M., Chambon, P., Gronemeyer, H., and Moras, D. (1995) Crystal structure of the ligand-binding domain of the human nuclear receptor RXR-alpha, *Nature* 375, 377-382.
164. Gronemeyer, H. (1998) Receptor mechanisms: principles of agonism. 23-25 July 1998, Merano, Italy, *IDrugs* 1, 657-659.
165. Germain, P., Iyer, J., Zechel, C., and Gronemeyer, H. (2002) Co-regulator recruitment and the mechanism of retinoic acid receptor synergy, *Nature* 415, 187-192.
166. Dai, S. Y., Burris, T. P., Dodge, J. A., Montrose-Rafizadeh, C., Wang, Y., Pascal, B. D., Chalmers, M. J., and Griffin, P. R. (2009) Unique ligand binding patterns between estrogen receptor alpha and beta revealed by hydrogen-deuterium exchange, *Biochemistry* 48, 9668-9676.
167. Wass, M. N., Kelley, L. A., and Sternberg, M. J. (2010) 3DLigandSite: predicting ligand-binding sites using similar structures, *Nucleic Acids Res.* 38, W469-473.

168. Pike, A. C., Brzozowski, A. M., Walton, J., Hubbard, R. E., Thorsell, A. G., Li, Y. L., Gustafsson, J. A., and Carlquist, M. (2001) Structural insights into the mode of action of a pure antiestrogen, *Structure* 9, 145-153.